


2012-01-01

High Pressure Synchrotron X-Ray Diffraction Studies of Superprotonic Transitions in Phosphate Based Solid Acids

Juan Daniel Hermosillo
University of Texas at El Paso, hermosillo@gmail.com

Follow this and additional works at: https://digitalcommons.utep.edu/open_etd

 Part of the [Materials Science and Engineering Commons](#), [Mechanics of Materials Commons](#), [Oil, Gas, and Energy Commons](#), and the [Physics Commons](#)

Recommended Citation

Hermosillo, Juan Daniel, "High Pressure Synchrotron X-Ray Diffraction Studies of Superprotonic Transitions in Phosphate Based Solid Acids" (2012). *Open Access Theses & Dissertations*. 2312.
https://digitalcommons.utep.edu/open_etd/2312

This is brought to you for free and open access by DigitalCommons@UTEP. It has been accepted for inclusion in Open Access Theses & Dissertations by an authorized administrator of DigitalCommons@UTEP. For more information, please contact lweber@utep.edu.

HIGH PRESSURE SYNCHROTRON X-RAY DIFFRACTION STUDIES OF
SUPERPROTONIC TRANSITIONS IN PHOSPHATE
BASED SOLID ACIDS

JUAN DANIEL HERMOSILLO

Department of Materials Science and Engineering

APPROVED:

Cristian E. Botez, Ph.D., Chair

Lawrence E. Murr, Ph.D.

Russell R. Chianelli, Ph.D.

John C. McClure, Ph.D.

Benjamin C. Flores, Ph.D.
Interim Dean of the Graduate School

Copyright ©

by

Juan Hermosillo

2012

HIGH PRESSURE SYNCHROTRON X-RAY DIFFRACTION STUDIES OF
SUPERPROTONIC TRANSITIONS IN PHOSPHATE

BASED SOLID ACIDS

by

JUAN DANIEL HERMOSILLO, M.S.

DISSERTATION

Presented to the Faculty of the Graduate School of

The University of Texas at El Paso

in Partial Fulfillment

of the Requirements

for the Degree of

DOCTOR OF PHILOSOPHY

Department of Materials Science and Engineering

THE UNIVERSITY OF TEXAS AT EL PASO

May 2012

Acknowledgements

First and foremost, I would like to thank my advisor, Dr. Cristian Botez for all his support during this research project. He not only guided me in my research but was instrumental in me applying for and eventually getting the NSF GK-12 fellowship which has helped me to pursue a higher education. I would also thank Dr. Russell Chianelli for funding my trip to the 2006 Users Meeting at the Stanford Linear Accelerator Center to present the findings of this work.

This project was made possible by the support of the University of Texas Research Fund. Use of the National Synchrotron Light Source, Brookhaven National Laboratory, by the U.S. Department of Energy, Office of Basic Energy Sciences. I would also like to acknowledge support from the American Chemical Society Petroleum Research Fund under Award No. 45854-GB10, the Texas High Education Coordinating Board Norman Hackerman Advanced Research Program under Award No. 003661-0010-2007, and the Research Corporation Cottrell College Science Award No. 7749.

I would also like to thank the members for my defense committee, Dr. Murr, Dr Chianelli, and Dr. McClure for all the help and support they've provided me, and for taking the time to provide me with extremely constructive feedback on my research and dissertation.

Abstract

Certain phosphate based solid acids, such as CsH_2PO_4 and RbH_2PO_4 , have been shown to exhibit an abrupt, several-order-of-magnitude increase in their proton conductivity when heated above a temperature threshold. This so called superprotonic behavior allows the above-mentioned materials to function as fuel cell electrolytes at temperatures between 150°C and 300°C , a remarkable application that attracted significant interest especially from the automobile industry. Yet, the microscopic structures and dynamic mechanisms responsible for this behavior are not fully understood. In fact, until very recently, the very nature of the superprotonic behavior has been debate, with some groups attributing the steep proton enhancement to a polymorphic transition and others pointing out to possible chemical modifications. This is mainly due to the fact that heating the title materials under ambient pressure and humidity conditions does indeed lead to their dehydration at temperatures in the immediate vicinity of proton conductivity jump, which, in turn, generate ambiguity on the origin of the superprotonic behavior.

The main purpose of the investigations presented in this thesis is to clarify the origin of the above-mentioned heating-induced proton conductivity enhancement. To this end, we have mostly used high-pressure synchrotron x-ray diffraction methods to avoid dehydration and study the structural (and possibly chemical) modifications responsible for the observed proton conductivity behavior. However, for comparison purposes, we carried out similar measurements under ambient-pressure conditions. We investigated CsH_2PO_4 and RbH_2PO_4 , as well as their counterparts based on smaller size cations, i.e. KH_2PO_4 , NaH_2PO_4 , and LiH_2PO_4 .

Our initial temperature-resolved data collected on polycrystalline CsH_2PO_4 demonstrate that even under ambient pressure conditions this solid acid exhibits a transition from its room-temperature monoclinic ($\text{P2}_1/\text{m}$) phase to a cubic ($\text{Pm}3\text{m}$) modification. Yet, the cubic phase is not stable under ambient pressure and humidity conditions and dehydrates in minutes even in the absence of further heating. Further measurements on samples subjected to high pressure ($\text{P}=1\text{GPa}$) reveal the same monoclinic cubic polymorphic transition at $T\sim 260^\circ\text{C}$. In this case, the high temperature cubic phase ($\text{Pm}3\text{m}$, $a=4.88\text{ \AA}$) is stable, and the transition occurs under the same (P , T) conditions as the 1000-fold jump in CsH_2PO_4 's proton conductivity. Rietveld analysis confirms that the high-pressure cubic phase has essentially the same crystal structure as its counterpart observed under normal atmosphere. This unambiguously demonstrates that the superprotonic behavior of CsH_2PO_4 is due to a polymorphic transformation and not to dehydration-driven chemical modifications.

For RbH_2PO_4 we found a transition from its room temperature tetragonal (I-42d) phase to an intermediate temperature monoclinic ($\text{P2}_1/\text{m}$) modification, which, remarkably, is isomorphic to the room temperature monoclinic CsH_2PO_4 . This suggests that a monoclinic-cubic polymorphic transition, similar to the one observed in CsH_2PO_4 , is responsible for the Rb-based compound's superprotonic behavior. While further heating under ambient pressure conditions resulted in the sample's chemical decomposition, temperature-resolved data collected under 1 GPa of pressure revealed the existence of a previously unknown high-temperature RbH_2PO_4 polymorph. Moreover, this new phase has the same cubic symmetry as its Cs-based counterpart, thus confirming our hypothesis that the microscopic aspects that trigger the superprotonic behavior in phosphate solid acids are not cation-dependent, and a general highly-efficient proton conduction mechanism is at work in the high-temperature cubic phases of these compounds.

KH_2PO_4 has been shown not to exhibit a superprotonic behavior although it is isomorphic with RbH_2PO_4 at room temperature. Our data shows that this isomorphism persists in the intermediate temperature phases, which implies that the cation size plays a key role in determining the existence of a superprotonic behavior. We confirmed this hypothesis through temperature resolved x-ray diffraction measurements on small-cation phosphate solid acids NaH_2PO_4 and LiH_2PO_4 . Indeed, these latter materials do not appear to exhibit heating-induced transitions to the highly symmetric phases that enable an efficient proton transport in phosphate solid acids..

Table of Contents

Acknowledgements.....	iiv
Abstract	v
Table of Contents.....	vii
List of Tables.....	x
List of Figures	xi
List of Illustrations.....	xiii
Chapter 1: Introduction	1
1.1 Solid Acids.....	5
1.1.1 Acidity.....	5
1.2 Early Research	6
1.2.1 Superprotonic Behavior	7
Chapter 2: Fuel Cells	9
2.1 Basic Design	9
2.2 Types of Fuel Cells.....	9
2.2.1 Proton Exchange Membrane Fuel Cells	10
2.2.2 Direct Methanol Fuel Cells	11
2.2.3 Phosphoric Acid Fuel Cells.....	11
2.2.4 Alkaline Fuel Cells	11
2.2.5 Solid Oxide Fuel Cells	12
2.2.6 Molten Carbonate Fuel Cells.....	12
2.3 Applications	13
2.3.1 Pollution.....	13
2.3.2 Transportation	13
2.3.3 Military.....	14
2.4 Solid Acids as Electrolytes	14
Chapter 3: Theoretical Background.....	16
3.1 Alkali Metals.....	16
3.1.1 Atomic and Ionic Radii	16
3.1.2 First Ionization Energy	18

3.1.3 Electronegativity.....	19
3.2 Crystal Structures	20
3.2.1 Classification	20
Crystal System	20
The Bravais Lattices	21
Point and Space Groups.....	21
Lattice Planes and <i>hkl</i> -Indices.....	23
3.3 X-ray Diffraction.....	24
3.3.1 Single Crystal vs. Powder Diffraction	24
3.3.2 Data Interpretation	25
3.3.3 The Bragg Law	26
3.3.4 Data Interpretation When the Unit Cell is Known	28
Cubic System	28
Monoclinic System.....	29
3.3.5 Rietveld Refinement	30
3.3.6 Pawley Method.....	36
3.3.7 Le Bail Fit	42
Chapter 4: Experimental Methods.....	46
4.1 Sample Preparation.....	46
4.2 Ambient-Pressure Conditions	46
4.3 High-Pressure Conditions	50
Chapter 5: Results & Discussion.....	54
5.1 CsH ₂ PO ₄ & RbH ₂ PO ₄ : Ambient-Pressure Conditions.....	55
5.2 CsH ₂ PO ₄ & RbH ₂ PO ₄ : High-Pressure Conditions	62
5.3 KH ₂ PO ₄	67
5.4 LiH ₂ PO ₄	72
5.5 NaH ₂ PO ₄	73
5.6 Mixed Cation Solid Acids	74

Chapter 6: Conclusions	75
References	77
Vitaí í í í í ..	79

List of Tables

Table 1.1: Debate on Whether CsH_2PO_4 Shows a Superprotonic Transition.....	7
Table 2.1: Summary of Fuel Cell Temperature Ranges.	12
Table 3.1: Electron Configuration of the Alkali Metals	17
Table 3.2: Atomic and Ionic Radii of the Alkali Metals.....	17
Table 3.3: First Ionization Energies of the Alkali Earth Metals	18
Table 3.4: Electronegativities of the Alkali Metals.	19
Table 3.5: The 14 Lattice Types in three Dimensions.....	22
Table 3.6: Parameters in the Rietveld Method.	29

List of Figures

Figure 3.1: X-ray Powder Diffraction Data.	27
Figure 3.2: X-ray Powder Diffraction Ring Pattern	29
Figure 3.3: X-ray Powder Diffraction Pattern from Ring Integration	30
Figure 3.4: Powder Diffraction Pattern of Freon Gas Fluorotrichloromethane	32
Figure 3.5: Powder Diffraction Pattern of 220 Reflection of Nickel	33
Figure 3.6: Calculation of Intensity Contribution	36
Figure 3.7: 2 Peaks with Little Correlation.....	38
Figure 3.8: 2 Peaks Closer Together.....	39
Figure 3.9: 2 Peaks too Close Together	40
Figure 3.10: Extreme Example of near 100% Correlation.....	41
Figure 3.11: Profile Intensity Partitioning	43
Figure 4.1: Profile Parameters Used to Fit Powder Diffraction Data.....	47
Figure 4.2: Lattice Parameters Calculated with the Fullprof Program.....	48
Figure 4.3: Correct Peak Positions with Bad Profile Fit.....	49
Figure 4.4: Good Profile Fit with Incorrect Peak Positions.....	50
Figure 4.5: Excellent Fit Indicating a High Temperature Cubic Phase	51
Figure 5.1: X-ray Powder Diffraction Patterns from CsH_2PO_4	53

Figure 5.2: Temperature Dependence of the Lattice Parameters	55
Figure 5.3: Time Resolved Diffraction Patterns of CDP	57
Figure 5.4: Temperature Resolved Patterns of RDP.	58
Figure 5.5: Temperature Dependence of the Lattice Parameters of RDP.....	60
Figure 5.6: X-ray Powder Diffraction Pattern Under HP for CDP at 255 and 275C	62
Figure 5.7: X-ray Powder Diffraction Pattern Under HP for CDP at 275C	63
Figure 5.8: X-ray Powder Diffraction Pattern Under HP for CDP with excluded region	64
Figure 5.9: Proton Conductivity vs. Temperature.....	65
Figure 5.10: Temperature Resolved Pattern for RDP Under High Pressure.	67
Figure 5.11: Temperature Resolved Pattern for KDP.....	68
Figure 5.12: Structural Refinement of the Monoclinic KDP Phase.	69
Figure 5.13: Lattice Parameters of the Monoclinic Phases of KDP, RDP, and CDP.....	71
Figure 5.14: Temperature Resolved Diffraction Patterns of LiDP.....	72
Figure 5.15: Temperature Resolved Diffraction Patterns of NaDP.	73
Figure 5.16: Mixed-cation Phosphate Solid Acids.....	74

List of Illustrations

Illustration 1.1: Dynamic Disorder.....	2
Illustration 1.2: CDP Unit Cell.....	3
Illustration 2.1: Fuel Cell Diagram.....	10
Illustration 3.1: Definition of Miller Indices.....	23
Illustration 3.2: Indices Important in Cubic Phase	24
Illustration 3.3: Powder Diffraction Measurement Rings.....	26
Illustration 3.4: Derivation of the Bragg Equation.	31
Illustration 3.5: Overview of Le Bail Method.....	44
Illustration 5.1: Monoclinic RbH_2PO_4	61
Illustration 5.2: Monoclinic CsH_2PO_4	61
Illustration 5.3: Comparison Between the Atom Positions in the Unit Cells of RDP and KDP.....	70

Chapter 1: Introduction

Fuel cells are currently being studied for applications in countless fields. They are one of the most promising forms of alternative energy due to their extremely adaptable nature. They can be used under various operating conditions and can make use of a vast number of fuel sources, ranging from molecular hydrogen to biomass, or even hydrocarbons.

Fuel cells produce electrical energy without combustion typically by using hydrogen as fuel. The basic design of a fuel cell includes an electrolyte capable of conducting protons in between a cathode and an anode. The hydrogen molecules are stripped of their electrons by a catalyst at the anode. The cations (single protons) then pass through an electrolyte that conducts protons while blocking the flow of electrons. These loose electrons can then be used to provide a current passing through an external load after which they can be redirected back to the cathode where they, along with the transferred protons can reduce molecular oxygen into water or steam.

Solid acids are a new class of proton conducting electrolytes under consideration for fuel cell applications. These compounds have been shown to exhibit a large increase in their proton conductivity at temperatures ranging from 150-300°C¹. This makes them extremely lucrative for use in fuel cells operating at these intermediate temperature ranges in which there are only a few other competitors. They have numerous advantages over current polymer electrolyte membrane fuel cells under development, ranging from more efficient cooling to a higher tolerance to catalyst poisons.

Sulfate based solid acids were the first to be studied as possible electrolytes; however they were quickly abandoned due to their tendency to react with molecular hydrogen to produce H₂S which poisons the catalyst. As stated earlier, the catalyst is responsible for oxidizing the molecular hydrogen producing the loose protons and electrons. As the catalyst becomes less efficient, it allows more H₂ molecules to reach the electrolyte which in turn produces more H₂S molecules creating a chain reaction that ultimately kills the fuel cell. Fully hydrogenated phosphate based solid acids such as CsH₂PO₄ and RbH₂PO₄ do not react with hydrogen and therefore are much more suitable alternative.

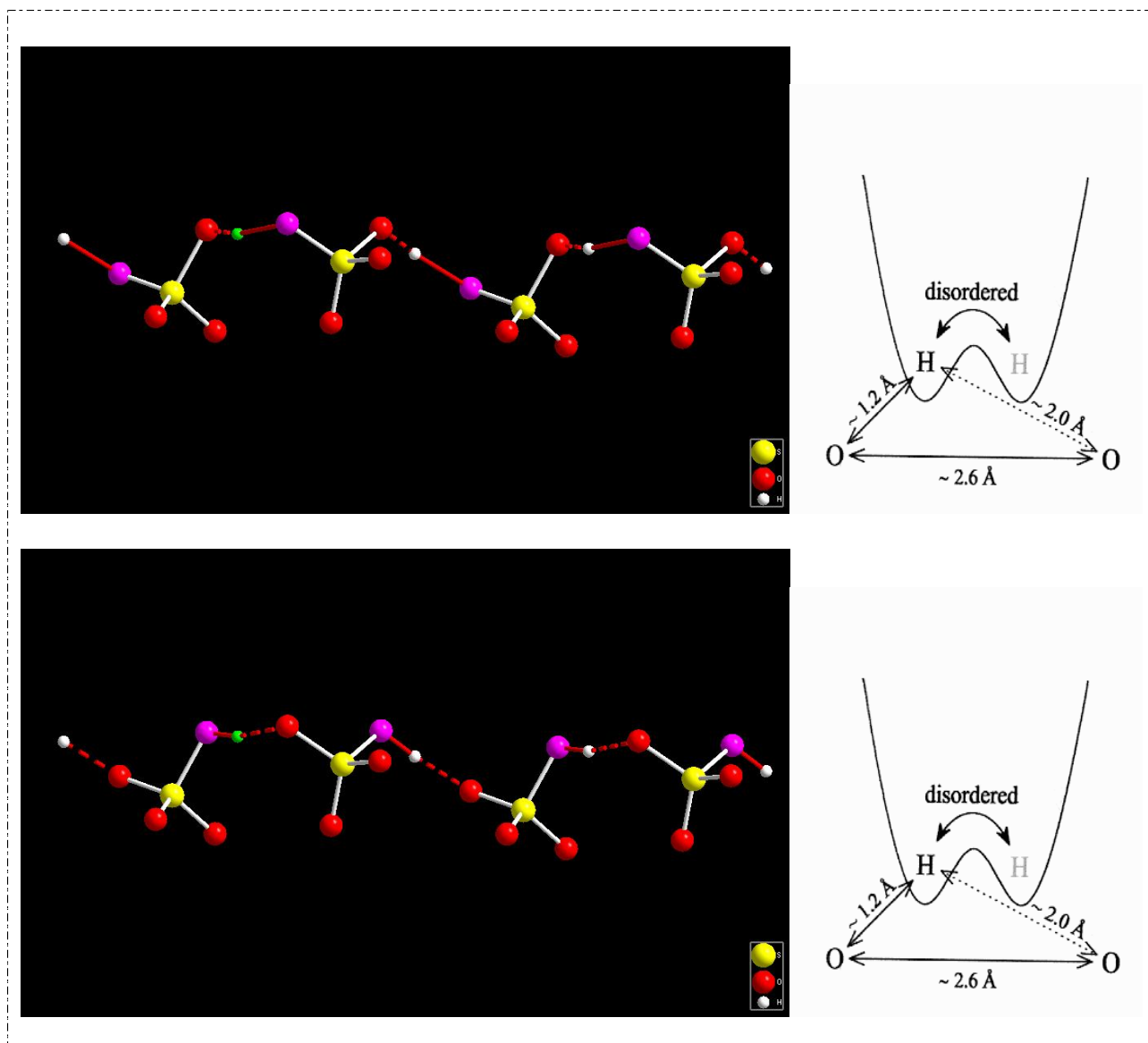


Illustration 1.1: Dynamic disorder in CsHSO_4 responsible for proton conduction.

Since sulfate based solid acids are only half hydrogen bonded, the proton conduction mechanism is much better understood than in their phosphate based counterparts. The hydrogen bonds connecting the sulfate tetrahedra become disordered at high temperatures allowing for protons to jump along empty sites (see illustration 1.1). The mechanism behind the sharp increase in proton conductivity in phosphate based solid acids however, is not known. Since these compounds are fully hydrogenated, there are hydrogen bonds at all four corners of the phosphate tetrahedra (see illustration 1.2) which

prevent the same mechanism from working. The proton conduction mechanism in phosphate based solid acids is thought to be caused by two possible factors.

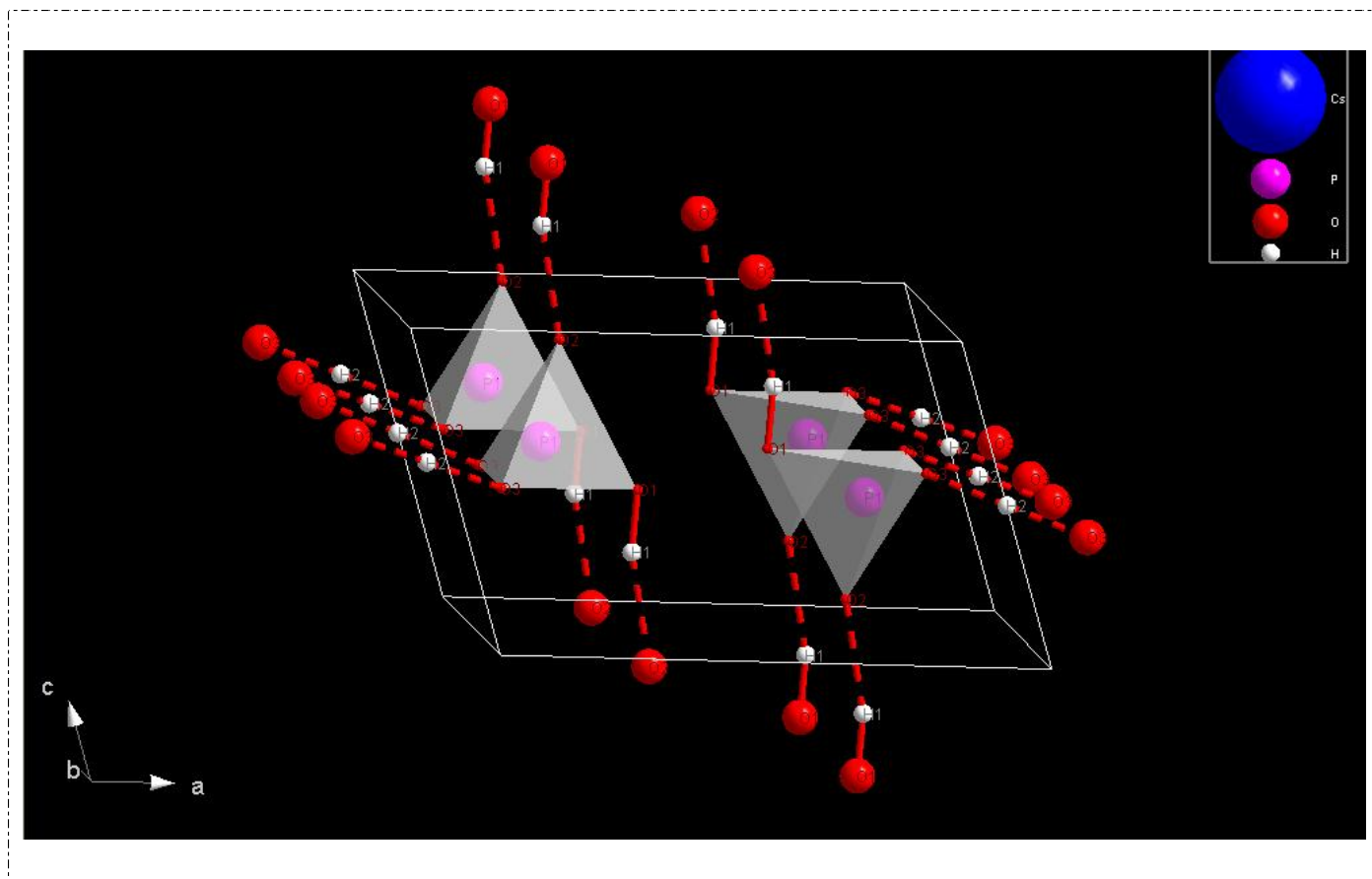
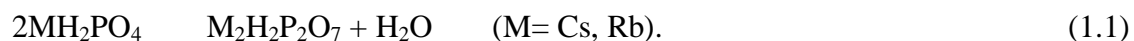


Illustration 1.2: The hydrogen bonds at all four corners of each tetrahedron do not allow the bucket brigade mechanism to work.

One theory stems from the fact that these materials tend to dehydrate when heated under ambient conditions via the reaction:



This would indicate that water molecules and not the solid acid are responsible for the proton conduction. A second theory, the one to which we subscribe, is that these solid acids undergo a structural modification to a high symmetry phase at high temperature which allows for a much more efficient proton transport path. We have already shown this high symmetry phase to exist in CsH_2PO_4

which undergoes a monoclinic to cubic structural transition at temperatures near the superprotonic transition⁴¹.

The broad objective of this work is to develop a better understanding of the superprotonic behavior of CsH_2PO_4 (CDP), RbH_2PO_4 (RDP), and other fully hydrogenated phosphate based solid acid compounds, so as to allow the engineering of these compounds with the desired properties for their application in devices. Specifically, we wish to determine the high temperature phase of RbH_2PO_4 and correlate that to the cubic phase of CsH_2PO_4 which we believe is responsible for the superprotonic behavior of these materials at high temperatures.

The proton conductivity of both CsH_2PO_4 (CDP) and RbH_2PO_4 (RDP) exhibits a sharp, 1000-fold increase upon heating above a temperature threshold.¹⁻³ Yet, if the heating is carried out under ambient humidity and pressure conditions, these materials dehydrate and transform into pyrophosphates at temperatures in the immediate vicinity of the above-mentioned superprotonic transition via equation 1.1.

Two methods have been proposed to inhibit, or at least delay CDP and RDP's dehydration. The first is to raise the temperature while keeping the samples under a saturated water vapor atmosphere. This was successfully used to reveal the existence of a high-temperature cubic CDP phase⁴, and to demonstrate the functionality of this material as a fuel cell electrolyte¹, a remarkable application that attracted significant interest. RDP also exhibits a proton conductivity jump upon heating above a temperature threshold, but, for this solid acid, a superprotonic phase could not be stabilized under a saturated water vapor atmosphere. Instead, the sample had to be subjected to a pressure of 1 GPa in order to observe an abrupt increase in its proton conductivity upon heating above 295°C.³ While this clearly demonstrates that RDP does become superprotonic at high temperatures, the crystal structure of the superprotonic phase and its relationship with its CDP counterpart are still unknown. Therefore, it is worth exploring the application of well-established crystal structure analysis techniques, such as synchrotron x-ray diffraction, to the study of the heating-induced behavior of phosphate solid acids under high pressure. This is important because achieving the ultimate goal of the investigation of these materials is the uncovering of the microscopic mechanisms responsible for their proton conductivity

enhancement ó essentially depends on acquiring precise knowledge of their superprotonic phase crystal structures.

Here we present a high pressure temperature-resolved synchrotron x-ray diffraction (XRD) study of polycrystalline CDP and RDP, where the crystal structure evolution of these materials is followed as their temperature is raised from 30°C to 300°C. X-ray scattering methods enhanced by the use of synchrotron radiation have been successfully used to reveal structural information about a wide variety of physical systems from metallic surfaces^{5,6} to magnetic systems⁷ and organic compounds.^{8,9} In particular, powder XRD has significantly benefited from the use of synchrotron x-rays¹⁰. This method is also very well suited for our present investigation, as heating-induced crystal twinning or cracking (previously reported in phosphate solid acids¹¹) does not affect powder XRD.

The remainder of this introduction will cover a brief history and description of solid acids. It includes sections on how acids were first categorized and how the eventual evolution of the definition allows materials such as CsH_2PO_4 to be categorized as solid acids. It then includes a brief background on the study of solid acids. The other parts of this paper include a chapter on the basics of fuel cells and their applications, an introduction to the theory behind x-ray diffraction, an experimental methods section, and finally a results and conclusions section.

1.1 SOLID ACIDS

1.1.1 Acidity

The concept of acidity has evolved drastically since it was first introduced. In 1884, Svante August Arrhenius, a doctoral student, proposed a classification of acids and bases in which he claimed that acids were substances that deliver hydrogen cations to a solution and bases are substances that deliver hydroxyl anions to the solution. At the time, Arrhenius' claims seemed preposterous to the scientific community and he was scornfully awarded a fourth class degree. In 1903, however, his claims were proven right and he was awarded the Nobel Prize in chemistry¹². This work led two other chemists, Johannes Nicolaus Brønsted and Thomas Martin Lowry, to further extend the theory into what is currently known today as the Brønsted-Lowry concept. According to this theory, acids are substances that can donate a proton and bases are substances that can accept a proton.

In most instances this accepting and donating of protons is done in a solution such as water. Later, Gilbert Newton Lewis extended the definition of acids and bases by focusing on electron pairs instead of protons. According to his definition, an acid is a substance that can accept an electron pair and a base is any substance that can donate an electron pair. This broadened the scope of acids and bases to compounds that do not contain hydrogen or hydroxide respectively. It also removed the connection to water. An acid and a base could simply exchange electron pairs between themselves without having to be dissolved in water. Through this reasoning, we are able to classify a solid substance not dissolved in water, such as CsH_2PO_4 , as an acid.

These types of substances, also known as acid salts, actually have properties intermediate to those of normal salts and normal acids. CsH_2PO_4 monocrystals for instance, can be grown from an aqueous solution of H_3PO_4 (acid) and Cs_2CO_3 (salt). Solid acids can therefore be brittle and insulating like salts but also contain structural acid protons such as a Brønsted-Lowry acid. In addition these structural acid protons give solid acids their most interesting properties including ferroelectricity and superprotonic conductivity.

1.2 EARLY RESEARCH

The first research on solid acids was conducted mostly on their ferroelectric and other low temperature properties ($< -150^\circ\text{C}$) such as piezoelectric, electro-optical, and non-linear optical properties.¹³ It was not until the 1980s that their high temperature behavior ($> 100^\circ\text{C}$) began to receive attention; behaviors such as a superprotonic phase transition in which, upon heating, the proton conductivity increased 1000-fold.^{14,15} Due to solid acids' solubility in water however, they were not considered to be applicable as electrolytes in fuel cells. Later research however, has shown that solid acids can be a realistic electrolyte simply by using them on fuel cells that operate above the boiling point of water.¹⁶

Table 1.1: Debate on whether CsH_2PO_4 shows a superprotonic transition^{14,17,18,19,20}.

Research Paper	Superprotonic Conductor?
Plakida, 1986	NO
Baranov <i>et al.</i> , 1989	YES
Romain <i>et al.</i> , 1991	YES
Haile <i>et al.</i> , 1995	NO
Lee <i>et al.</i> , 1996	NO
Luspin <i>et al.</i> , 1997	YES
Ortiz <i>et al.</i> , 1999	NO
Boysen <i>et al.</i> , 2003	YES
Boysen <i>et al.</i> , 2004	YES

1.2.1 Superprotonic Behavior

The mere existence of a superprotonic behavior of CsH_2PO_4 was under debate for almost two decades (see Table 1.1)^{14,17,18,19,20}. Although recent work has convincingly demonstrated that, indeed, a sample of CsH_2PO_4 becomes superprotonic upon heating¹⁹, little, if anything, is known about the microscopic mechanisms that enable the enhanced proton conduction in this material. Our previous work has shown a direct correlation between the superprotonic behavior of CDP and the monoclinic to cubic polymorphic structural transition it undergoes at high temperatures. Although this correlation does not imply a specific mechanism responsible for better proton conduction, it does give us a place to start the investigation.

RDP has also been observed to undergo a superprotonic transition at high temperatures. This superprotonic behavior, however, is only stable under high pressure conditions. Unlike CDP, which exhibits a stable superprotonic behavior under high pressure as well as in a vapor saturated environment, RDP does not. Both, however, do exhibit a similar superprotonic behavior under high pressure

conditions which implies that if CDP's superprotonic behavior is due to its transition into the cubic phase, RDPs superprotonic behavior should also be due to a polymorphic structural transition to a high symmetry phase.

Many authors have indicated that the observed superprotonic behavior of CDP is, in fact, due to dehydration followed by chemical decomposition^{14,21}, while others we suggest a polymorphic structural transition to a high-symmetry phase. The purpose of this work is to resolve this controversy and establish the chemical and structural character of the high temperature behavior of these materials. We are attempting to uncover the mechanisms of enhanced proton conduction in fully-hydrogen-bonded phosphate based solid acids, which in turn will improve the performance of these materials as fuel cell electrolytes and might contribute to the rational design of highly-efficient ionic conductors.

Chapter 2: Fuel Cells

Fuel cells produce energy without combustion through an electrochemical process that typically uses hydrogen as fuel. When the fuel cell system is equipped with a fuel reformer, however, the fuel cell can make use of the hydrogen from many different hydrocarbon fuels such as natural gas, methanol, propane, biomass, and even gasoline. Even when hydrocarbons are used as a fuel source, however, the emissions produced by the reforming process are still much cleaner than those produced from a combustion process, and when only hydrogen is used as the fuel source, the byproducts are only water and heat.

2.1 BASIC DESIGN

The basic design of a fuel cell is comprised of two electrodes separated by an electrolyte which is capable of conducting protons or cations between the electrodes but will not allow electrons to pass through. A fuel source such as hydrogen or methanol can then be oxidized by a catalyst at the anode.



The protons or cations will then pass through the electrolyte toward the cathode while the excess electrons pass through an external load providing a current. The protons and electrons can then be used at the cathode to reduce molecular oxygen into water or steam. See Illustration 2.1.



2.2 TYPES OF FUEL CELLS

There is a wide variety of fuel cell types which are characterized by their electrolytes and temperature of operation: the most common types are described below²². As we will see, most current fuel cells operate at either relatively low or extremely high temperature ranges as summarized in Table 2.1. Fuel cells that operate at intermediate temperatures such as those at which solid acids become superprotonic are therefore highly sought after.

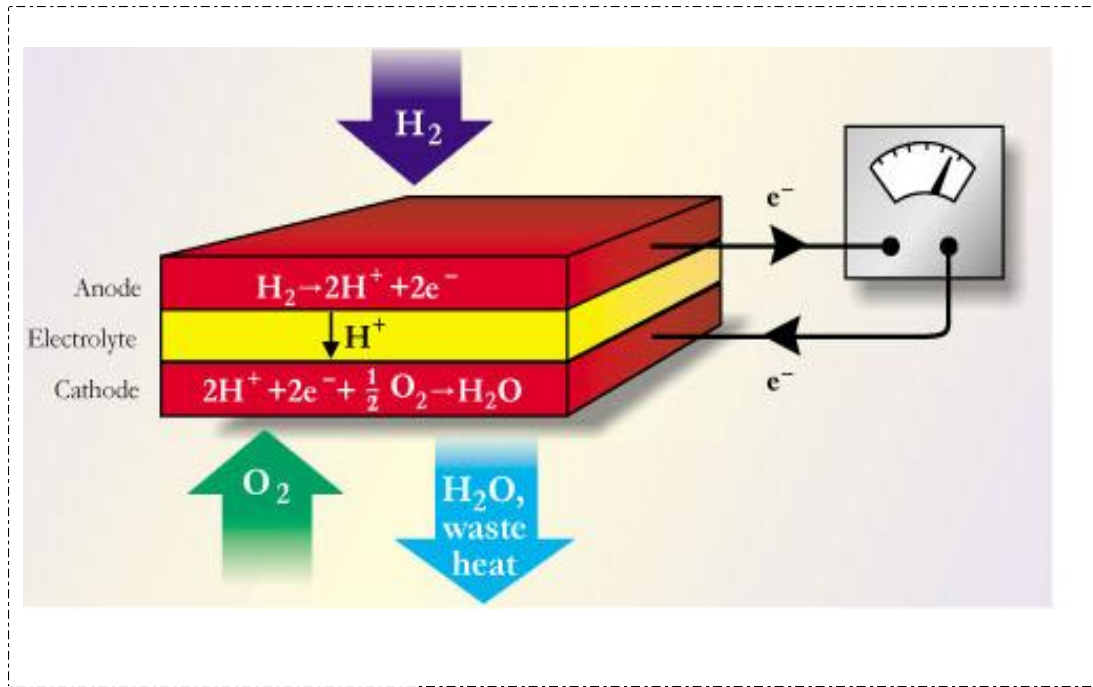


Illustration 2.1: Fuel cell diagram.

2.2.1 Proton Exchange Membrane Fuel Cells

Proton exchange membrane (PEM) fuel cells have a solid polymer membrane as an electrolyte. Due to membrane limitations, PEMs usually operate at low temperatures (60-100°C), but new developments have produced PEMs that can operate at temperatures up to 200°C. Platinum is used as the catalyst because it is the most chemically active substance for low temperature hydrogen separation. The hydrogen fuel is supplied as hydrogen gas or is reformed from methanol, ethanol, natural gas or liquefied petroleum gas and then fed into the fuel cell. Existing PEMs have a power range of about 50W to 150kW.

PEMs tend to have a low weight and volume with relatively good power-to-weight ratio. Since they operate at low temperatures, there is very little wear on their components. PEMs can also be started very quickly, and can supply full power in minutes or less. PEMs offer efficient operation of up to 50% electrical efficiency for the fuel cell itself and over 85% total efficiency when waste heat is captured for small-scale space and water heating. Despite their advantages, PEMs face a few challenges. For example, platinum catalysts are expensive and also subject to CO poisoning from hydrocarbon fuels, which can reduce the lifetime of the fuel cell.

2.2.2 Direct Methanol Fuel Cells

Direct methanol fuel cells (DMFCs) differ from PEMs because they use unreformed liquid methanol fuel rather than hydrogen. DMFCs operate at slightly higher temperatures than PEMs (50-120°C) and achieve around 40% efficiency. DMFCs are directed toward small mobile power applications such as laptops and cell phones because they can be refueled using replaceable methanol cartridges at power ranges of 1-50 W. The development of these fuel cells is subject to problems such as membrane corrosion, fuel crossover and miniaturization challenges.

2.2.3 Phosphoric Acid Fuel Cells

The phosphoric acid fuel cell (PAFC) is the fuel cell technology with the greatest experience in consumer applications. More than 200 PAFC fuel cell systems are installed all over the world, providing power and useful steam heat to hospitals, nursing homes, hotels, office buildings, schools, utility power plants, an airport terminal, landfills and waste water treatment plants. PAFCs use liquid phosphoric acid as an electrolyte with a platinum catalyst. Anode and cathode reactions are similar to PEMs, but operating temperatures are slightly higher (150-200°C) making them more tolerant to reforming impurities. PAFCs use hydrocarbon sources such as natural gas, propane or waste methane. They are typically used for medium to large-scale stationary power generation, attaining a 36-42% electrical efficiency and an overall 85% total efficiency with co-generation of electricity and heat. The power range of existing PAFCs is 25-250 kW. However, if several units are linked, PAFCs can achieve a combined power output greater than 1 MW.

2.2.4 Alkaline Fuel Cells

Fast-starting alkaline fuel cells (AFCs) have been used by NASA to produce power and drinking water for astronauts since the 1960s Gemini missions. AFCs operate in an electrolyte solution of potassium hydroxide and can use a variety of non-precious metal catalysts at operating temperatures of 25-250°C. Fueled by hydrogen gas, AFCs have a high chemical reaction rate and offer an electrical efficiency of 60-70%. However, AFCs are poisoned easily by small quantities of CO₂, so they are mostly used in controlled aerospace and underwater applications.

2.2.5 Solid Oxide Fuel Cells

Solid oxide fuel cells (SOFCs) are one of the high temperature fuel cells, operating at 800-1000°C. High temperature operation eliminates the need for precious metal catalysts and can reduce cost by recycling the waste heat from internal steam reformation of hydrocarbon fuels. SOFCs are tolerant to CO poisoning, allowing CO derived from coal gas to also be employed as a source of fuel. These fuel cells use a solid ceramic electrolyte and produce a power output of 2-100 kW and can attain 220 kW-300 kW when used in a SOFC/gas turbine hybrid system. Demonstrated electrical efficiencies are 45-55%, with total efficiencies of 80-85% with cogeneration of waste heat.

2.2.6 Molten Carbonate Fuel Cells

Molten carbonate fuel cells (MCFCs) operate at 600-750°C and use a molten alkali carbonate mixture for an electrolyte. MCFCs typically range between 75-250 kW, but when using combined units, have produced up to 5 MW of power. Electrical efficiencies are 50-60%, with total efficiencies of 80-85% with cogeneration of waste heat. To date, MCFCs have operated on hydrogen, carbon monoxide, natural gas, propane, landfill gas, marine diesel, and simulated coal gasification products. The challenges to both SOFC and MCFC development include slow start up, strong thermal shielding requirements, and difficulty in developing durable materials for the high temperature operating environment.

Table 2.1: Summary of Fuel Cell Temperature Ranges.

Fuel Cell Type	Operating Temperatures
Proton Exchange Membrane	60-100°C
Direct Methanol	50-120°C
Phosphoric Acid	150-200°C
Alkaline	25-250°C
Solid Oxide	800-1000°C
Molten Carbonate	600-750°C

2.3 APPLICATIONS

Fuel cells have applications in almost every field with a need for energy sources²³. Right now, all of the major automakers are working on ways to economically commercialize a fuel cell car. Fuel cells are currently used to power buses, boats, trains, planes, scooters, as well as bicycles. There are even fuel cell-powered vending machines, vacuum cleaners, and highway road signs. Furthermore, miniature fuel cells for cellular phones, laptop computers and portable electronics are on their way to market. Even businesses such as hospitals, credit card centers, police stations, and banks are all using fuel cells to provide power to their facilities. And others such as wastewater treatment plants and landfills are using fuel cells to convert the methane gas they produce into electricity. The possibilities are endless.

2.3.1 Pollution

Air pollution, for example, continues to be a primary health concern in America. Exposure to ozone, particulate, or airborne toxic chemicals has substantial health consequences. Therefore, scientists are now directly linking air pollution to heart disease, asthma and cancer. Recent health studies have suggested that polluted urban air is a comparable health threat to passive smoking. Fuel cells can begin to reduce pollution today and offer the promise of eliminating pollution in the near future.

2.3.2 Transportation

Fuel cell vehicles are the least polluting of all vehicles that consume fuel directly. Fuel cell vehicles operating on hydrogen stored on-board the vehicles produce zero pollution in the conventional sense. Neither conventional pollutants nor green house gases are emitted. The only byproducts are water and heat. Systems that rely on a reformer on board to convert a liquid fuel to hydrogen produce small amounts of emissions, but would still reduce smog-forming pollution by up to 90 percent compared to traditional combustion engines, depending on the choice of fuel. The simple reaction that takes place inside the fuel cell is highly efficient. Even if the hydrogen is produced from fossil fuels, fuel-cell vehicles can reduce emissions of carbon dioxide, a global warming concern, by more than half. Tests performed on a fuel cell bus, fueled by methanol, showed zero emissions of particulate matter and hydrocarbons, and near-zero emissions of carbon monoxide and nitrous oxides, these levels being far below the 1998 emission standard for buses.

2.3.3 Military

Fuel cells help the military reduce the cost of battlefield logistics, provide a source of energy for the modern soldier, save money and reduce pollution at military installations and on board ships and terrestrial vehicles, and most importantly, save lives and material by reducing telltale heat and noise.

A 2001 Defense Science Board report concluded that "over 70 percent of the tonnage required to position today's US Army into battle is fuel." The report also found that significant war-fighting, logistics and cost benefits occur when weapons systems are made more fuel-efficient¹⁵. Many organizations are working on miniature fuel cells for portable applications since soldiers are starting to carry a range of enabling electronic technologies, computers, personal radios, displays and thermal imaging, all intended to increase their effectiveness, lethality and survivability. Right now, these devices are limited by their power source. Miniature fuel cells can operate 10 times longer than conventional batteries used to power hand-held battlefield computers, and are much more cost-effective.

Stationary fuel cells are helping the military to address their peak electric power needs while complying with the presidential directive to reduce energy use at Federal facilities by 20%. Stationary fuel cells for military applications can provide back up or standby power for special operations and activities and can provide power in remote areas.

2.4 SOLID ACIDS AS ELECTROLYTES

Many different types of electrolytes can be used in a fuel cell ranging from polymers to solid acids. Solid acids can only be used at certain temperatures in which they go through a phase transition where their proton conductivity increases anywhere from 100 to several 1000 fold. These temperature ranges (150-300°C)^{5,9} are usually well above the functioning temperatures for most polymer electrolytes therefore solid acids provide a useful alternative for fuel cells needed to operate at intermediate temperatures.

CsHSO₄ was the first solid acid successfully used as a fuel cell electrolyte²⁴, but it was soon realized that the long-term performance of such a cell is likely to be affected by the reaction between sulfur and hydrogen, which produces the catalyst poison H₂S:



A possible solution would be to use electrolytes based on phosphate oxy-anions, such as CsH_2PO_4 , RbH_2PO_4 or KH_2PO_4 . For these fully-hydrogenated solid acids, however, the high-temperature behavior is not as well understood as for their half-hydrogen-bonded counterparts.

Chapter 3: Theoretical Background

3.1 ALKALI METALS

The alkali metals consist of the elements in the first group of the periodic table. They include lithium, sodium, potassium, rubidium, cesium, francium and a theoretical ununennium which has yet to be discovered and is not believed to occur in nature. Francium was also not considered in this study due to its radioactive nature. The alkali earth metals provide the best example of group trends in properties in the periodic table being that they are more similar to each other than the elements in any other group are to each other. The atomic radius, for example, increases steadily as you move down the table³⁵. Following the same trend, they also show decreasing electronegativity, increased reactivity³⁶, and decreasing melting and boiling points. They are all shiny, soft, silvery, highly reactive metals at standard temperature and pressure and readily lose their outermost electron to form cations with a +1 charge. This allows all of them to form fully hydrogenated phosphate solid acids in the form:



The similar characteristics of alkali metals, along with their somewhat predictable slight variations make them an ideal group of elements to work with when studying how (or whether) the crystal structure of these solid acids affects their proton conductivity. Because of the relatively close chemical properties in these metals, any variation in the proton conductivity of these types of solid acids should stem from their crystal structure rather than the cation type. Furthermore, any variation in crystal structure also be easily predicted and explained by considering the slight differences in properties the alkali metals exhibit. A further analysis and discussion of these properties is therefore required.

3.1.1 Atomic and ionic radii

The atomic radii of the alkali metals increase going down the group³⁵. The atomic radius of any atom depends on several factors including the size of the nucleus (which depends on the atomic number), the number of electron shells, and how tightly those shells are arranged around the nucleus. The last factor depends on how strongly the positively charged nucleus attracts the electrons in each shell. Each electron feels electric repulsion from the other electrons as well as electric attraction from the nucleus³⁷. When an atom has more than one electron shell, the shells between the electron and the

nucleus create a shielding effect which acts to reduce the effective nuclear charge the electron feels. In the alkali metals, the outermost electron only feels a net charge of +1, as some of the nuclear charge (which is equal to the atomic number) is cancelled by the inner electrons. In alkali metals, the number of inner electrons is always one less than the nuclear charge. Therefore, the only factor which affects the atomic radius of the alkali metals is the number of electron shells. Since this number increases down the group, the atomic radius must also increase down the group³⁵.

Table 3.1: Electron configuration of the alkali metals.

Z	Element	Number of electrons/shell	Electron configuration
3	Lithium	2, 1	[He] 2s ¹
11	Sodium	2, 8, 1	[Ne] 3s ¹
19	Potassium	2, 8, 8, 1	[Ar] 4s ¹
37	Rubidium	2, 8, 18, 8, 1	[Kr] 5s ¹
55	Cesium	2, 8, 18, 18, 8, 1	[Xe] 6s ¹
87	Francium	2, 8, 18, 32, 18, 8, 1	[Rn] 7s ¹

Table 3.2: Atomic and ionic radii of the alkali metals³⁶.

Alkali Metal	Atomic radius (pm)	Ionic radius (pm)
Lithium	152	68
Sodium	185	98
Potassium	227	133
Rubidium	247	148
Cesium	265	167

The ionic radii of the alkali metals are much smaller than their atomic radii. This is because the outermost electron of the alkali metals is in a different electron shell than the inner electrons, and thus when it is removed the resulting atom has one fewer electron shell and is smaller. Additionally, the

effective nuclear charge has increased, and thus the electrons are attracted more strongly towards the nucleus and the ionic radius decreases.

3.1.2 First ionization energy and reactivity

The first ionization energy of an element or molecule is the energy required to move the most loosely held electron from one mole of gaseous atoms of the element or molecules to form one mole of gaseous ions with electric charge +1. The factors affecting the first ionization energy are the nuclear charge, the amount of shielding by the inner electrons and the distance from the most loosely held electron from the nucleus, which is always an outer electron in main group elements. The first two factors change the effective nuclear charge the most loosely held electron feels. Since the outermost electron of alkali metals always feel the same effective charge (+1), the only factor which affects the first ionization energy is the distance from the outermost electron to the nucleus. Since this distance increases down the group, the outermost electron feels less attraction from the nucleus and thus the first ionization energy decreases³⁵. (This trend is broken in francium due to relativistic effects.) Therefore, it is easier for the outer electron to be removed from the atom and participate in chemical reactions, thus increasing reactivity down the group.

Table 3.3: First ionization energies of the alkali earth metals^{37,38}.

Alkali metal	First ionization energy (kJ/mol)
Lithium	520.2
Sodium	495.8
Potassium	418.8
Rubidium	403.0
Cesium	375.7
Francium	380

3.1.3 Electronegativity

Electronegativity is a chemical property that describes the tendency of an atom or a functional group to attract electrons (or electron density) towards itself⁴⁰. If the bond between sodium and chlorine in sodium chloride were covalent, the pair of shared electrons would be attracted to the chlorine because the effective nuclear charge on the outer electrons is +7 in chlorine but is only +1 in sodium. The electron pair is attracted so close to the chlorine atom that they are practically transferred to the chlorine atom (an ionic bond). However, if the sodium atom was replaced by a lithium atom, the electrons will not be attracted as close to the chlorine atom as before because the lithium atom is smaller, making the electron pair more strongly attracted to the closer effective nuclear charge from lithium. Hence, the larger alkali metal atoms (further down the group) will be less electronegative as the bonding pair is less strongly attracted towards them³⁵.

Because of the higher electronegativity of lithium, some of its compounds have a more covalent character. For example, lithium iodide (LiI) will dissolve in organic solvents, a property of most covalent compounds³⁵. Lithium fluoride (LiF) is the only alkali halide that is not soluble in water, and lithium hydroxide (LiOH) is the only alkali metal hydroxide that is deliquescent³⁶.

Table 3.4: Electronegativities of the alkali metals³⁹.

Alkali metal	Electronegativity
Lithium	0.98
Sodium	0.93
Potassium	0.82
Rubidium	0.82
Cesium	0.79
Francium	0.7

3.2 CRYSTAL STRUCTURES

Crystals are composed of arrangements of identical groups of atoms which form unit cells that repeat periodically. These unit cells are known as the basis of the crystal structure. We can define this basis mathematically using three translation vectors \mathbf{a}_1 , \mathbf{a}_2 , \mathbf{a}_3 , which will shift any point \mathbf{r} in the unit cell to the same point on a different unit cell when that point is translated by an integral multiple of the three vectors:

$$\mathbf{r}' = \mathbf{r} + u_1\mathbf{a}_1 + u_2\mathbf{a}_2 + u_3\mathbf{a}_3 \quad (\text{where } u_1, u_2, u_3 \text{ are integers}) \quad (3.1)^{25}$$

The set of points defined by (2.1) for all u_i defines the crystal lattice. There are only a set number of possible arrangements that can produce a crystal and it is based on these arrangements that crystals can be classified.

3.2.1 Classification

The defining property of a crystal is its inherent symmetry, which means that under certain operations the crystal remains unchanged. For example, rotating the crystal 180 degrees about a certain axis may result in an atomic configuration which is identical to the original configuration. The crystal is then said to have a two-fold rotational symmetry about this axis. In addition to rotational symmetries like this, a crystal may have symmetries in the form of mirror planes and translational symmetries, and also compound symmetries which are a combination of translation and rotation or mirror symmetries. A full classification of a crystal is achieved when all of these inherent symmetries of the crystal are identified.

Crystal System

The crystal systems are a grouping of crystal structures according to the axial system used to describe their lattice. Each crystal system consists of a set of three axes in a particular geometrical arrangement. There are seven unique crystal systems. The simplest and most symmetric, the cubic (or isometric) system, has the symmetry of a cube, that is, the three axes are mutually perpendicular and of equal length. The other six systems, in order of decreasing symmetry, are hexagonal, tetragonal, trigonal, orthorhombic, monoclinic and triclinic. The crystal system and Bravais lattice of a crystal describe the purely translational symmetry of the crystal.

The Bravais Lattices

When the crystal systems are combined with the various possible lattice centerings, we arrive at the Bravais lattices. They describe the geometric arrangement of the lattice points, and thereby the translational symmetry of the crystal. In three dimensions, there are 14 unique Bravais lattices which are distinct from one another in the translational symmetry they contain. All crystalline materials recognized until now fit in one of these arrangements. The fourteen three-dimensional lattices, classified by crystal system, are shown in Table 3.1.

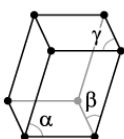
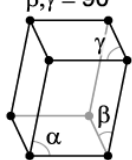
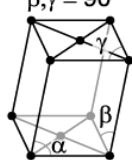
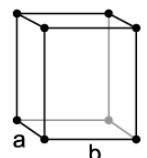
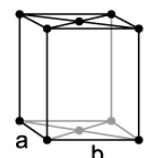
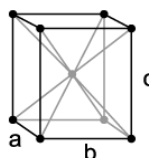
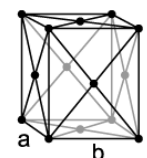
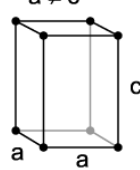
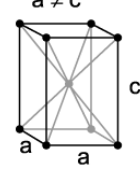
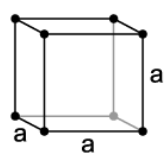
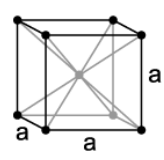
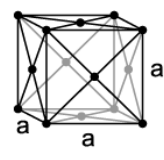
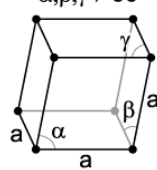
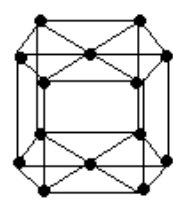
The crystal structure consists of the same group of atoms, the basis, positioned around each and every lattice point. This group of atoms therefore repeats indefinitely in three dimensions according to the arrangement of one of the 14 Bravais lattices. The characteristic rotation and mirror symmetries of the group of atoms, or unit cell, is described by its crystallographic point group.

Point and Space Groups

The crystallographic point group or crystal class is the set of non-translational symmetry operations that leave the appearance of the crystal structure unchanged. These symmetry operations can include mirror planes, which reflect the structure across a central plane, rotation axes, which rotate the structure a specified number of degrees, and a center of symmetry or inversion point which inverts the structure through a central point. There are 32 possible crystal classes. Each one can be classified into one of the seven crystal systems.

The space group of the crystal structure is composed of the translational symmetry operations in addition to the operations of the point group. These include pure translations which move a point along a vector, screw axes, which rotate a point around an axis while translating parallel to the axis, and glide planes, which reflect a point through a plane while translating it parallel to the plane. There are 230 distinct space groups.

Table 3.5: The 14 lattice types in three dimensions

System	Lattices			
Triclinic	$\alpha, \beta, \gamma \neq 90^\circ$ 			
Monoclinic	$\alpha \neq 90^\circ$ $\beta, \gamma = 90^\circ$  Simple		$\alpha \neq 90^\circ$ $\beta, \gamma = 90^\circ$  Base-Centered	
Orthorhombic	$a \neq b \neq c$  Simple	$a \neq b \neq c$  Base-Centered	$a \neq b \neq c$  Body-Centered	$a \neq b \neq c$  Face-Centered
Tetragonal	$a \neq c$  Simple		$a \neq c$  Body-Centered	
Cubic	 Simple	 Body-Centered		 Face-Centered
Trigonal	$\alpha, \beta, \gamma \neq 90^\circ$ 			
Hexagonal				

Lattice Planes and hkl -Indices

The planes which give rise to the reflections discussed above are called lattice planes, and have an orientation relative to the lattice which may be defined by Miller indices with the values hkl ²⁶. Every plane passing through points of the lattice is one of a stack of parallel planes such that every point of the lattice will lie in one plane of the stack, regardless of its orientation. The hkl indices of any such stack can be determined by examining the plane which lies nearest to the origin, without passing through it. Its intercepts on the a -, b -, and c -axes of the unit cell will be $1/h$, $1/k$ and $1/l$, which must be rational fractions. See Illustration 3.1.

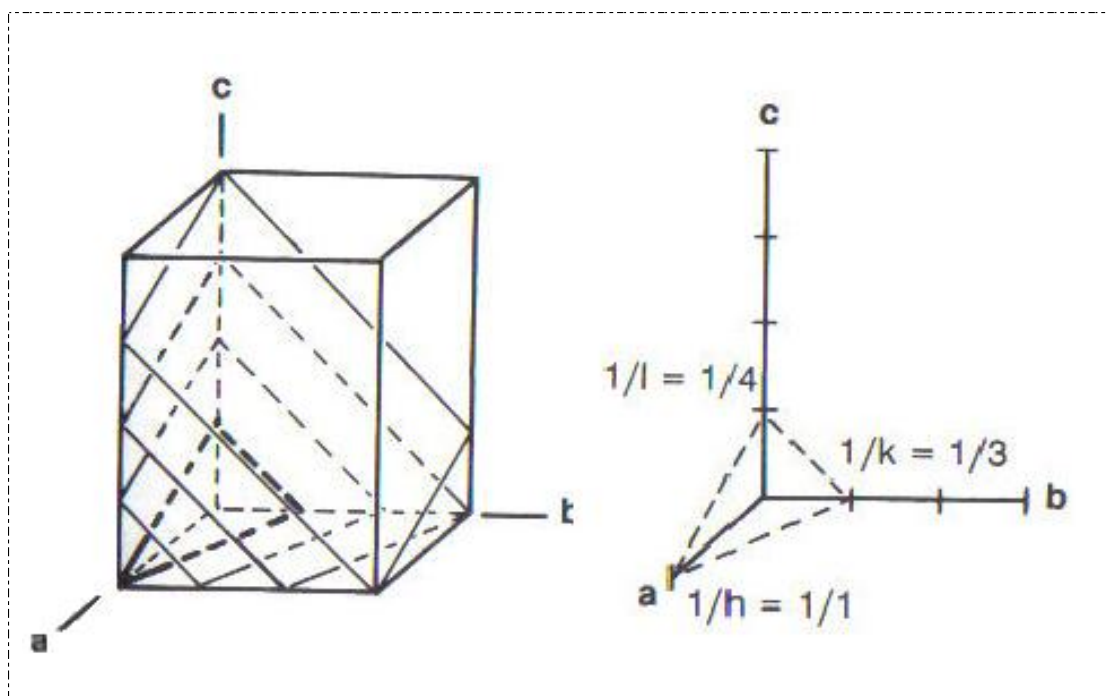


Illustration 3.1: Definition of hkl -values in terms of intercepts on the axes.

The reciprocals of these, which are integers, are the required indices hkl . An index of 0 indicates an intercept at infinity, that is, the planes are parallel to a crystallographic axis. For example, the planes (100), (010) and (001) are parallel to the faces of the unit cell of a cubic crystal. The indices hkl may denote a single plane or a set of parallel planes. If a plane cuts an axis on the negative side of the origin, the corresponding index is negative, indicated by placing a minus sign above the index; $\bar{h}\bar{k}\bar{l}$. Illustration 3.2 shows several different planes in a cubic crystal.

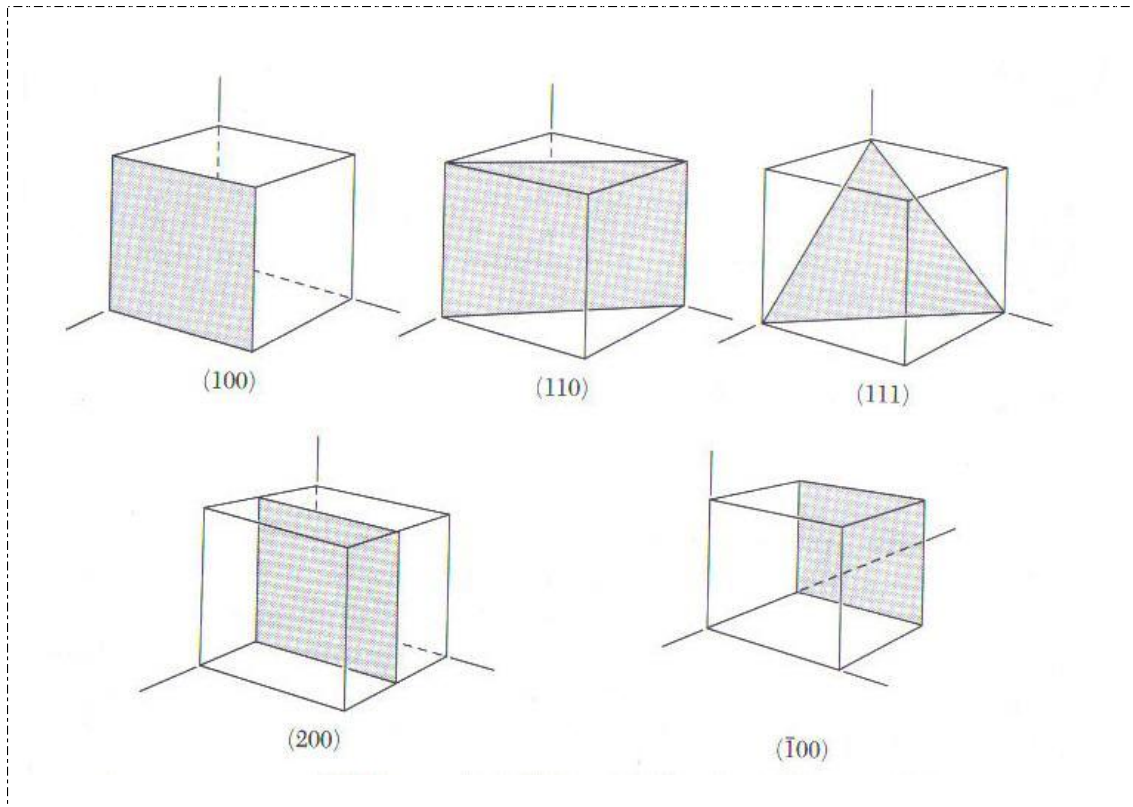


Illustration 3.2: Indices of important planes in a cubic crystal. The plane (200) is parallel to (100) and to $(\bar{1}00)$

3.3 X-RAY DIFFRACTION

X-ray diffraction is a technique used in crystallography in which the pattern produced by the diffraction of X-rays through the closely spaced lattice of atoms in a crystal is recorded and then analyzed to reveal the nature of that lattice.²⁷ This generally leads to an understanding of the material and atomic structure of a crystalline substance. The spacing in the crystal lattice can be determined using Bragg's law. Two different forms of X-ray diffraction can be used to determine crystalline structures: single crystal X-ray diffraction and X-ray powder diffraction. Each is used depending on the availability of samples or the nature of the experiment.

3.3.1 Single Crystal vs. Powder Diffraction

Whenever possible, single crystal diffraction is the preferred diffraction method because the data collected is more straightforward and is much easier to analyze. The data collected from a diffraction

experiment is a reciprocal space representation of the crystal lattice. The position of each diffraction spot is governed by the size and shape of the unit cell, and the inherent symmetry within the crystal. The data is also much easier to make sense out of because the orientation of the crystal can be controlled. In principle, one can learn everything there is to learn about the structure from it.

Single crystal diffraction, however, is not always feasible. For instance, it is not always possible to obtain a single crystal of the sample. It is also very difficult and time consuming to orient the crystal before and during the experiment, and since our experiment had to be done repeatedly at many different temperatures, single crystal diffraction would have proven to be quite ineffective. Also, in single crystals, defects in the crystal structure such as twinning can cause ambiguities in the data. This is the case in phosphate based solid acids. At high temperatures and pressures they tend to crack and/or twin. Due to these disadvantages of single crystal diffraction it is sometimes necessary to use smaller samples ground up into powder form.

The data obtained from powder diffraction is not as straightforward as that obtained from single crystal diffraction. This is because the crystallites in the powder are randomly oriented and it is thus not possible to see individual diffraction spots. We instead observe rings of diffracted intensity as a function of reciprocal lattice units (See Figure 3.1, Illustration 3.3). This makes finding the structure using powder diffraction data much more difficult and less reliable. However, this technique is optimal for following phase changes as a function of temperature, pressure, or some other variable because it is much less time consuming.

3.3.2 Data Interpretation

As stated above, powder diffraction experiments produce rings of diffracted intensities giving a graph as shown in Figure 3.1. These graphs are not very useful in determining diffraction angles or intensities therefore the data must be processed further to yield a graph with more readable information. To do this, the rings in these graphs can be integrated using plotting software such as Fit2D. The solid white line leading to the center point in the figure is due to the beam stop which is a material at the end of a beam placed there to completely stop and absorb the remaining beam particles and therefore, that part of the graph must be ignored when the diffraction rings are integrated. This is done by placing a

mask over the section which should be ignored and integrating over the remaining sections. Figure 3.2 shows a graph of the resulting data once the integration is complete.

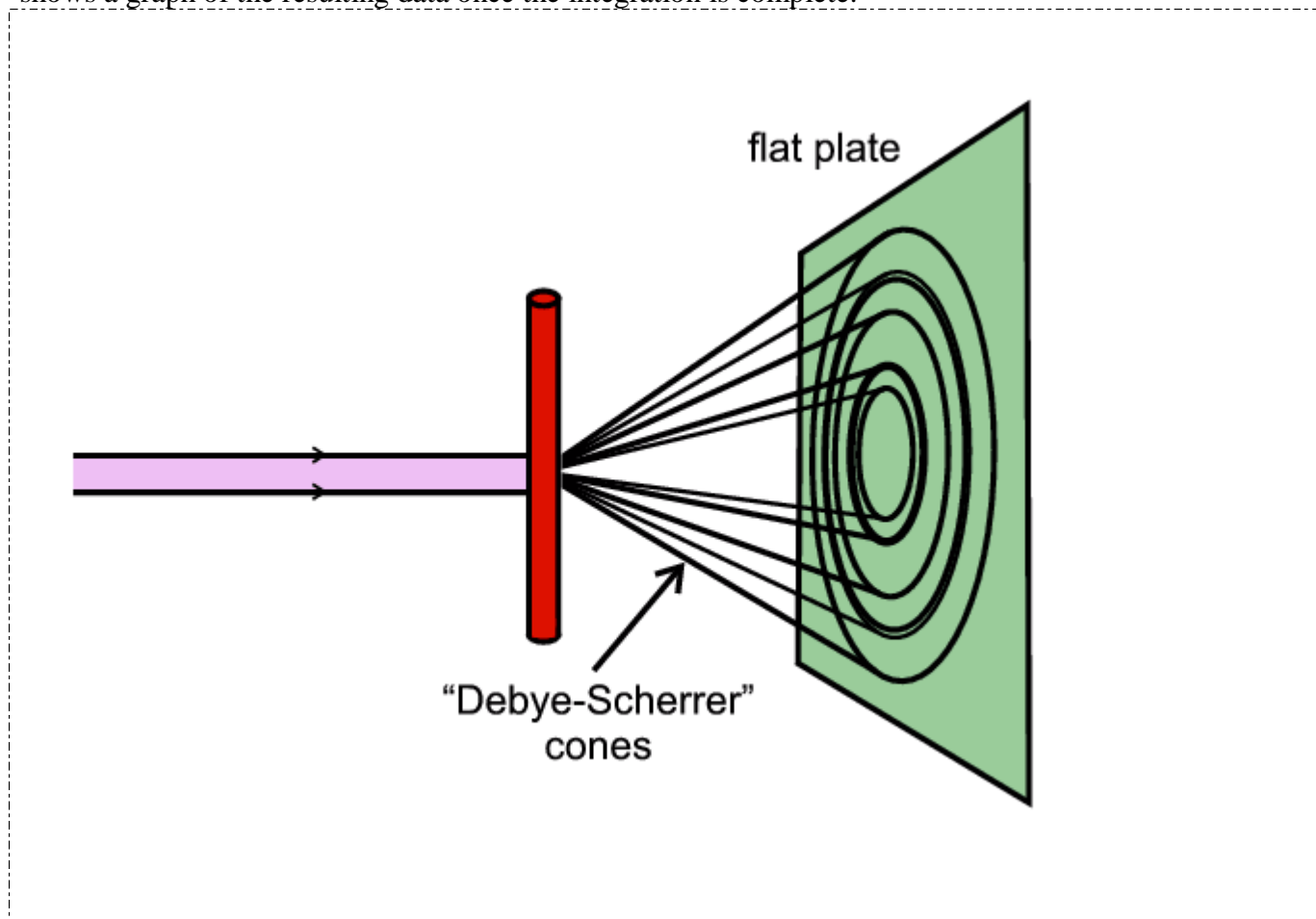


Illustration 3.3: Experiments carried out the X7B beamline at the National Synchrotron Light Source.

This data can then be analyzed to yield the position of the Bragg peaks corresponding to the Bragg angle, θ . Once every θ is known, in principle, the whole pattern can be indexed. Figure 3.3 shows a graph similar to the one in Figure 3.2 with all the Bragg peaks marked after being analyzed with the Fullprof software. From these angles, the experimental value of either $\sin^2 \theta$ or $1/d^2$ for each Bragg peak is determined, and indexing is carried out with one or other of these sets of values.

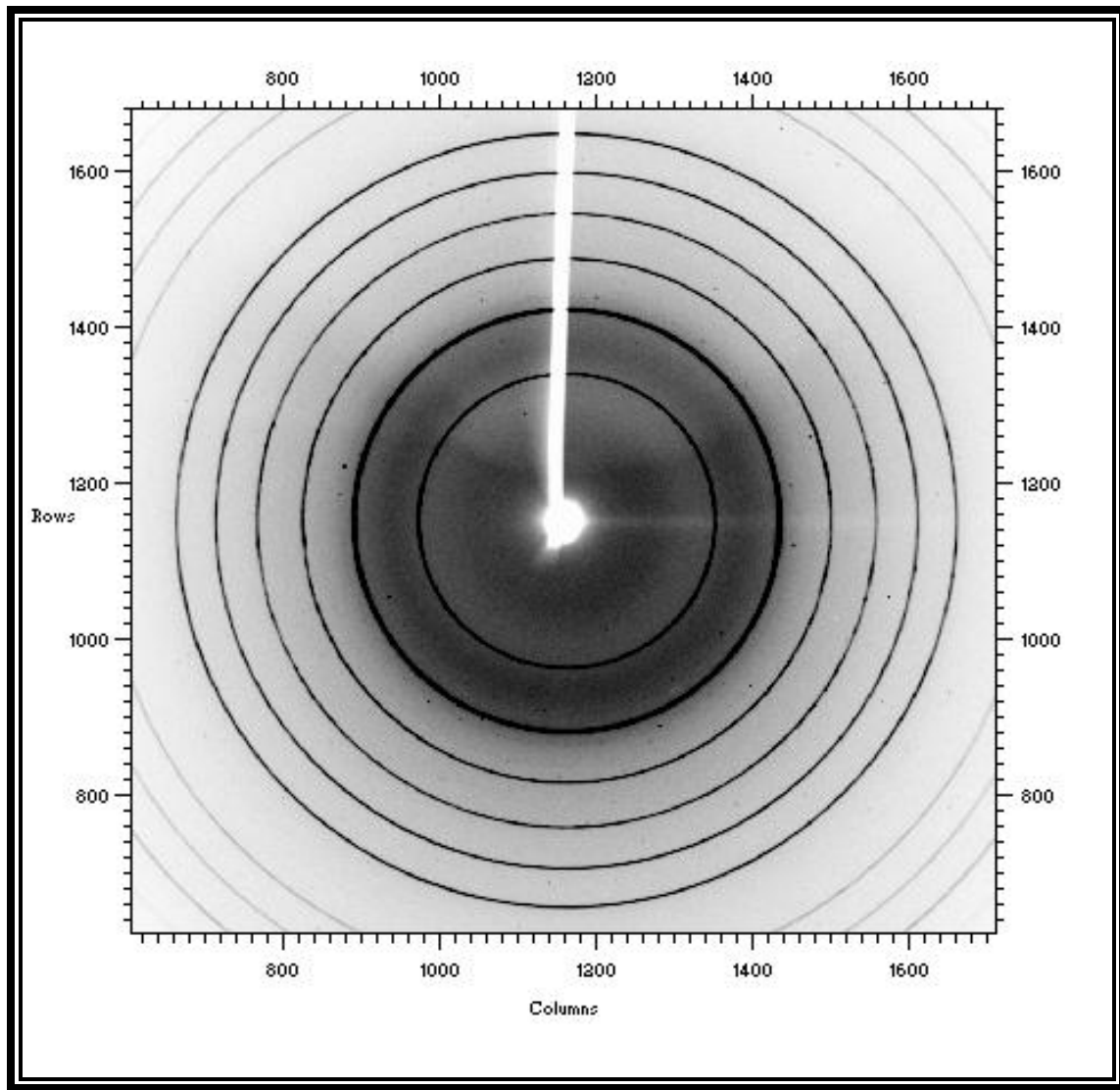


Figure 3.1: X-ray powder diffraction data corresponding to a cubic phase

3.3.3 The Bragg Law

In 1913, William Lawrence Bragg and William Henry Bragg proposed the Bragg formulation of X-ray diffraction after discovering that crystalline solids produced surprising patterns of reflected X-rays. They observed that when the X-rays were reflected at specific wavelengths and incident angles, intense peaks of reflected radiation were produced. W.L. Bragg explained this phenomenon using a very simple explanation. He modeled the crystal as a set of discrete parallel planes spaced a constant distance d apart (see Illustration 2.1). He then proposed that when a beam of X-rays penetrates the crystal, each plane reflects a small fraction of the radiation where the angle of reflection is equal to the angle of incidence θ . The intense peaks are therefore produced when the reflection from the parallel

planes of atoms interfere constructively. As can be seen in Illustration 3.4, the path difference for reflected rays from two adjacent planes is $2d \sin \theta$. In order for the rays to interfere constructively, this path difference must be a multiple of the wavelength λ , which gives us Bragg's law:

$$2d \sin \theta = n\lambda \quad (\text{where } n \text{ is an integer}) \quad (3.2)$$

3.3.4 Data Interpretation When the Unit Cell is Known

When the unit cell of the sample being studied is known, only three different stages are required to interpret the powder diffraction data. These steps include the derivation of the Bragg angles from the diffraction pattern, the calculation of Bragg angles for all possible combinations of indices hkl , and finally the comparison of these two sets of results²⁸. Previous work has shown that at room temperature, CsH_2PO_4 has a monoclinic structure and that it changes phases into a cubic structure at high temperatures.

Cubic System

For the cubic system, the expression for $\sin^2 \theta$ can be obtained by combining the Bragg equation (3.2) with the expression

$$d = \frac{a}{\sqrt{h^2 + k^2 + l^2}} \quad (3.3)$$

for the spacing, d , of the (hkl) planes in terms of the unit cell edge, a , and the indices h , k and l . This gives

$$\sin^2 \theta_{hkl} = \frac{\lambda^2}{4a^2} (h^2 + k^2 + l^2) \quad (3.4)$$

The quantity $h^2 + k^2 + l^2$ is an integer so that all that is required is to calculate the value of $\lambda^2/4a^2$ and to multiply it by the possible values of $h^2 + k^2 + l^2$. Because $\sin^2 \theta$ can never be greater than unity, it is not necessary to include values of $(\lambda^2/4a^2)(h^2 + k^2 + l^2)$ which are greater than this. Values of $\sin^2 \theta$ for the observed diffraction pattern can then be compared to these in order to determine which lines are actually present.

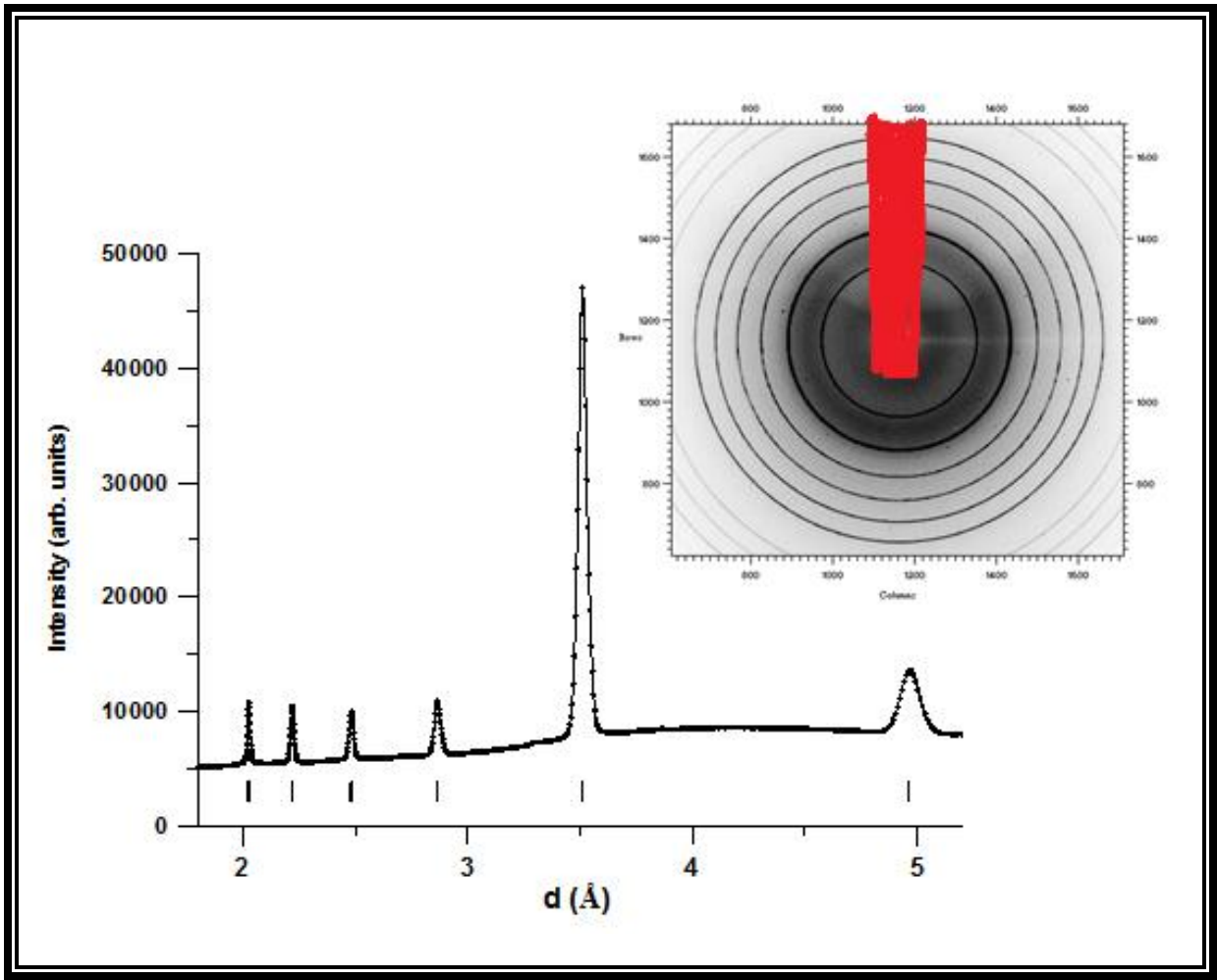


Figure 3.2: Graph obtained from integrating ring pattern resulting from X-ray diffraction experiments.

Monoclinic System

For the monoclinic system, the expression for \sin^2 in terms of the direct lattice parameters is more complicated:

$$\sin^2 \theta_{hkl} = \frac{\lambda^2}{4} \left\{ \frac{h^2/a^2 + l^2/c^2 - 2hl \cos \beta / ac + k^2/b^2}{\sin^2 \beta} \right\} \quad (3.5)$$

where b is perpendicular to the plane of a and c , and β is the angle between a and c . It is clearly possible, from this expression, to compare the observed and calculated values of \sin^2 but calculating every single possible value of \sin^2 can be laborious. The tedium can be reduced using the simpler relations obtained when \sin^2 is expressed in terms of the parameters of the reciprocal unit cell. With these parameters, namely $a^* = 1/a$, $b^* = 1/b$, and $c^* = 1/c$, which reduces (3.5) to

$$\sin^2 \theta_{hkl} = \frac{\lambda^2}{4} (h^2 a^{*2} + k^2 b^{*2} + l^2 c^{*2} + 2hlc^* a^* \cos \beta^*) \quad (3.6)$$

3.3.5 Rietveld Refinement

When the general space group and lattice parameters of a sample are either known or can be estimated, Rietveld refinement can be used to match the diffraction data with a more accurate representation of the unit cell. The big break through in the use of powder data for serious structural work came about for two reasons: Rietveld realized that the detailed profile of an angle-dispersive neutron powder-diffraction pattern contained a lot more information than the extracted intensities of composite peaks.²⁹ This is demonstrated in Figure 3.4 where, for example, the clickable region highlighted by the blue rectangle has two composite peaks composed of 10 different reflections.

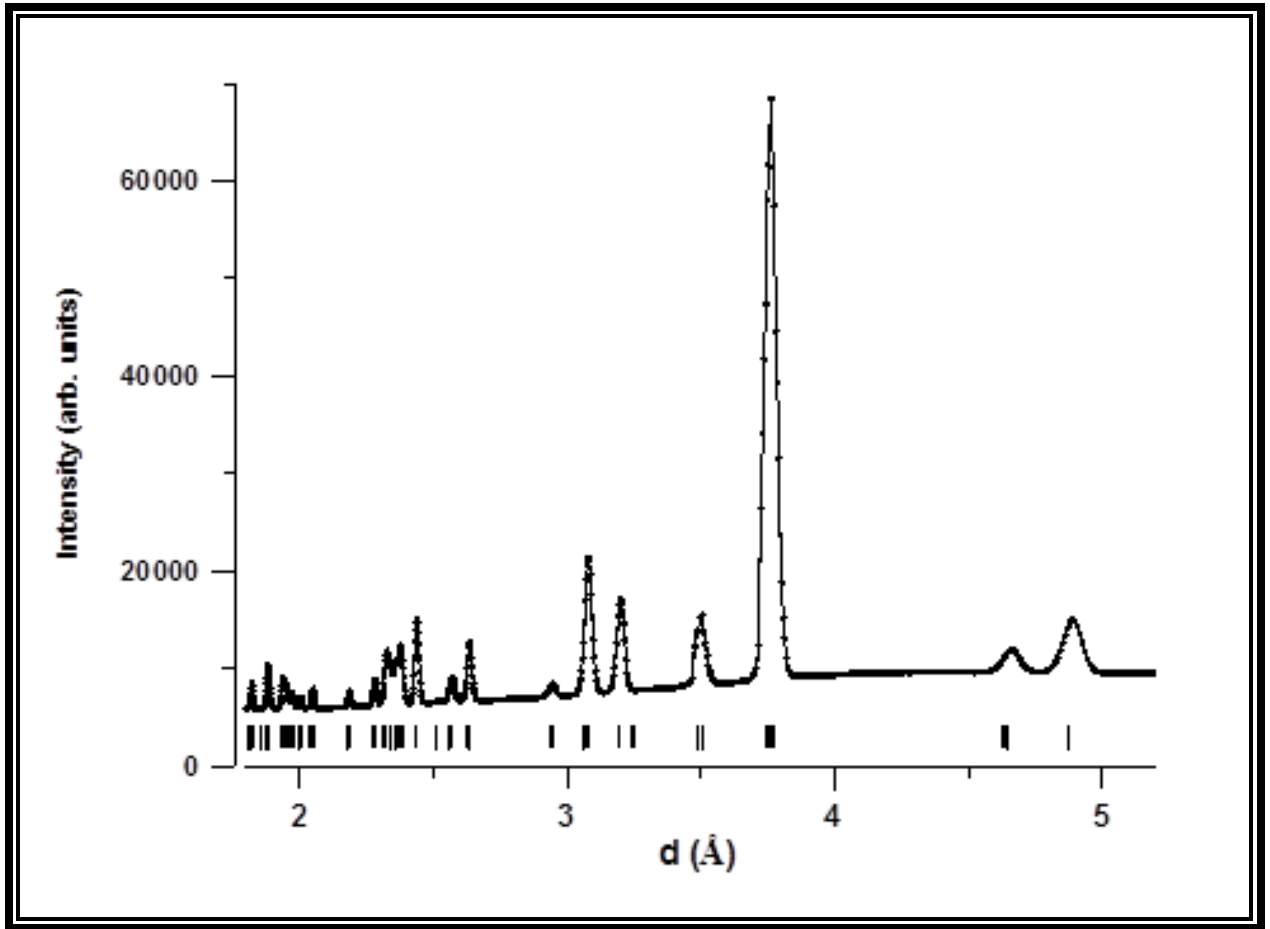


Figure 3.3: X-ray diffraction data with location of Bragg peak locations.

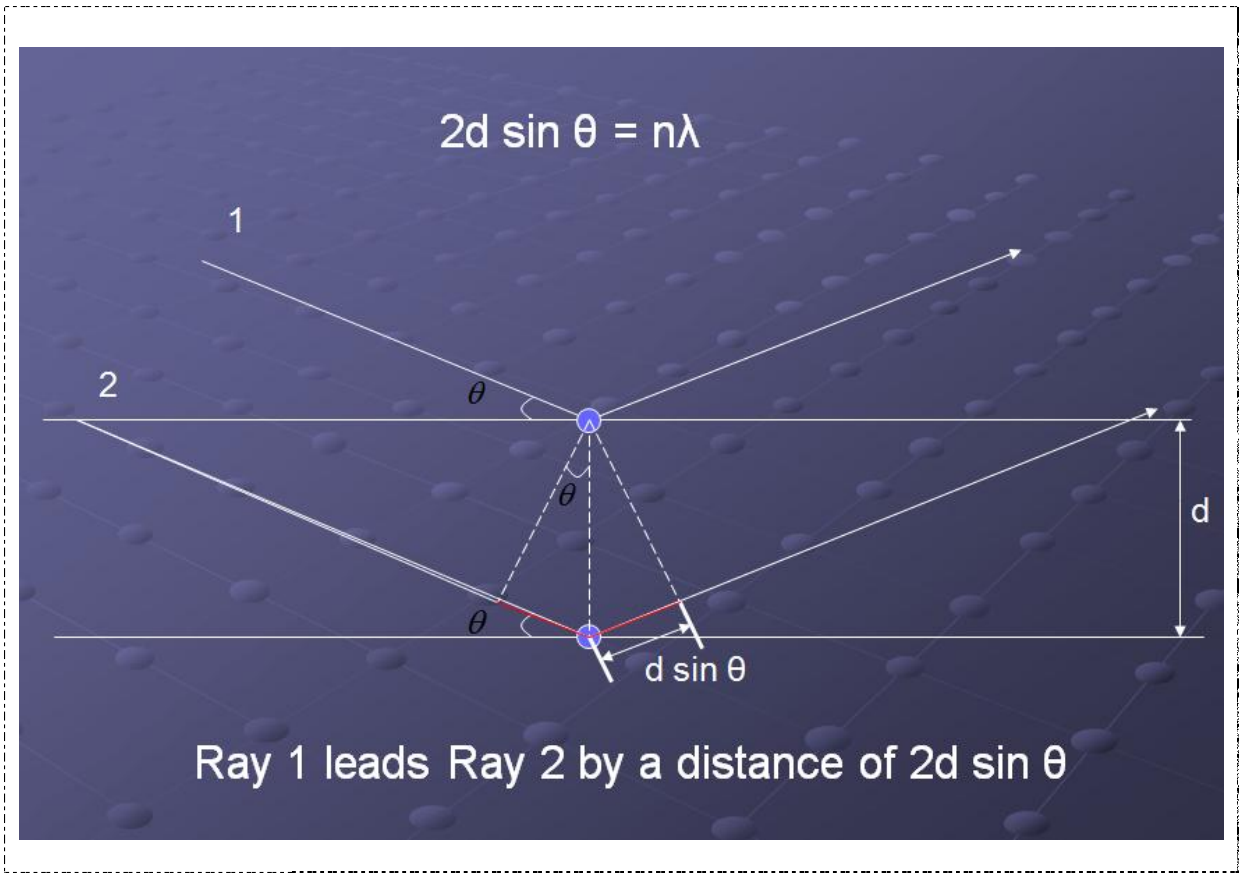


Illustration 3.4: Derivation of the Bragg equation $2d \sin \theta = n\lambda$ where d is the distance between parallel atomic planes and $2n$ is the phase difference between wave reflections from successive planes

Although the measured profile of a single powder diffraction peak is dependent on many different factors ranging from the shape and cristallinity of the sample to the specific properties of the diffractometer, it is an empirical fact that their convolution produces an almost exactly Gaussian peak shape as shown in Figure 3.5. The Gaussian peak-shape function, G , is given by:

$$G = \sqrt{(4 \ln 2 / \pi)} (I_{hkl} / H) e^{-4 \ln 2 (x_i - 2\theta_{hkl})^2 / H^2} \quad (3.7)$$

where

x is the 2θ value of the i^{th} profile point,

$2\theta_{hkl}$ is the centre of the peak (as determined by the d spacing),

H is the full-width at half-maximum height (FWHM) of the peak (as determined by the resolution function), and

I_{hkl} is the total intensity of the reflection with indices hkl .

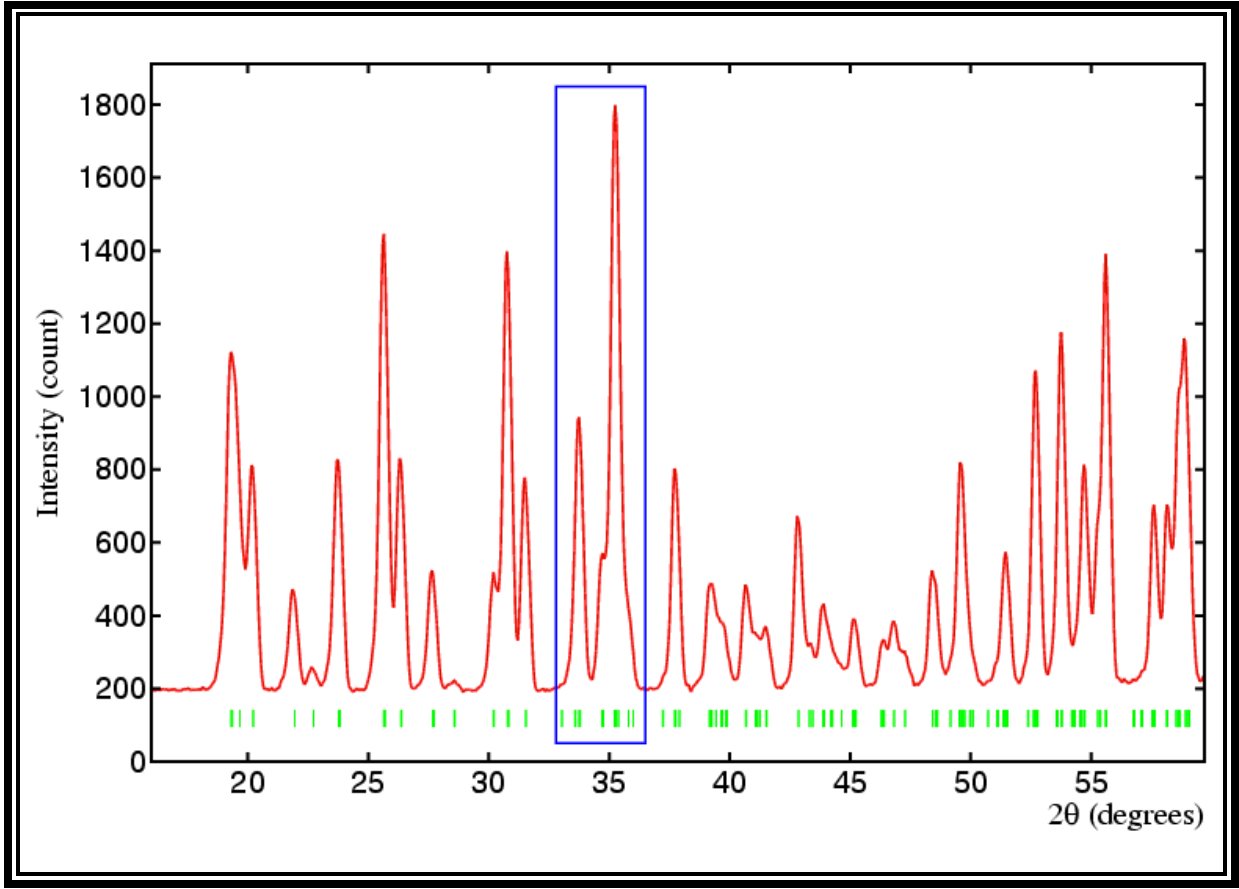


Figure 3.4: The red line shows the powder diffraction pattern of the solid phase of the freon gas fluoro-trichloromethane as measured on the powder neutron diffractometer D2B at the ILL, Grenoble. The green vertical tick lines indicate the position of peaks as determined from the unit-cell parameters and space-group symmetry.

Rietveld realized that the detailed profile could be fitted on a point by point basis using the simple Gaussian peak-shape function without any need to extract intensities of composite groups of reflections. The intensity, y_i , of the i^{th} profile point may be written as the summation of the contribution of the profiles of all reflections to that point:

$$y_i = \sum_{hkl} G(x_i, I_{hkl}, H) \quad (3.8)$$

$$y_i = \sum_{hkl} \sqrt{(4 \ln 2 / \pi)} I_{hkl} e^{-4 \ln 2 (x_i - 2\theta_{hkl})^2 / H^2} / H \quad (3.9)$$

$$y_i = \sum_{hkl} \sqrt{(4 \ln 2 / \pi)} c_j L(2\theta) F^2(hkl) e^{-4 \ln 2 (x_i - 2\theta_{hkl})^2 / H^2} / H \quad (3.10)$$

where

c is a scale factor,

j_{hkl} is the multiplicity of the reflection with indices hkl ,

$L(2\theta)$ is the Lorentz correction for the reflection at the scattering angle 2θ , and

$F^2(hkl)$ is the square of the structure factor of the reflection with indices hkl .

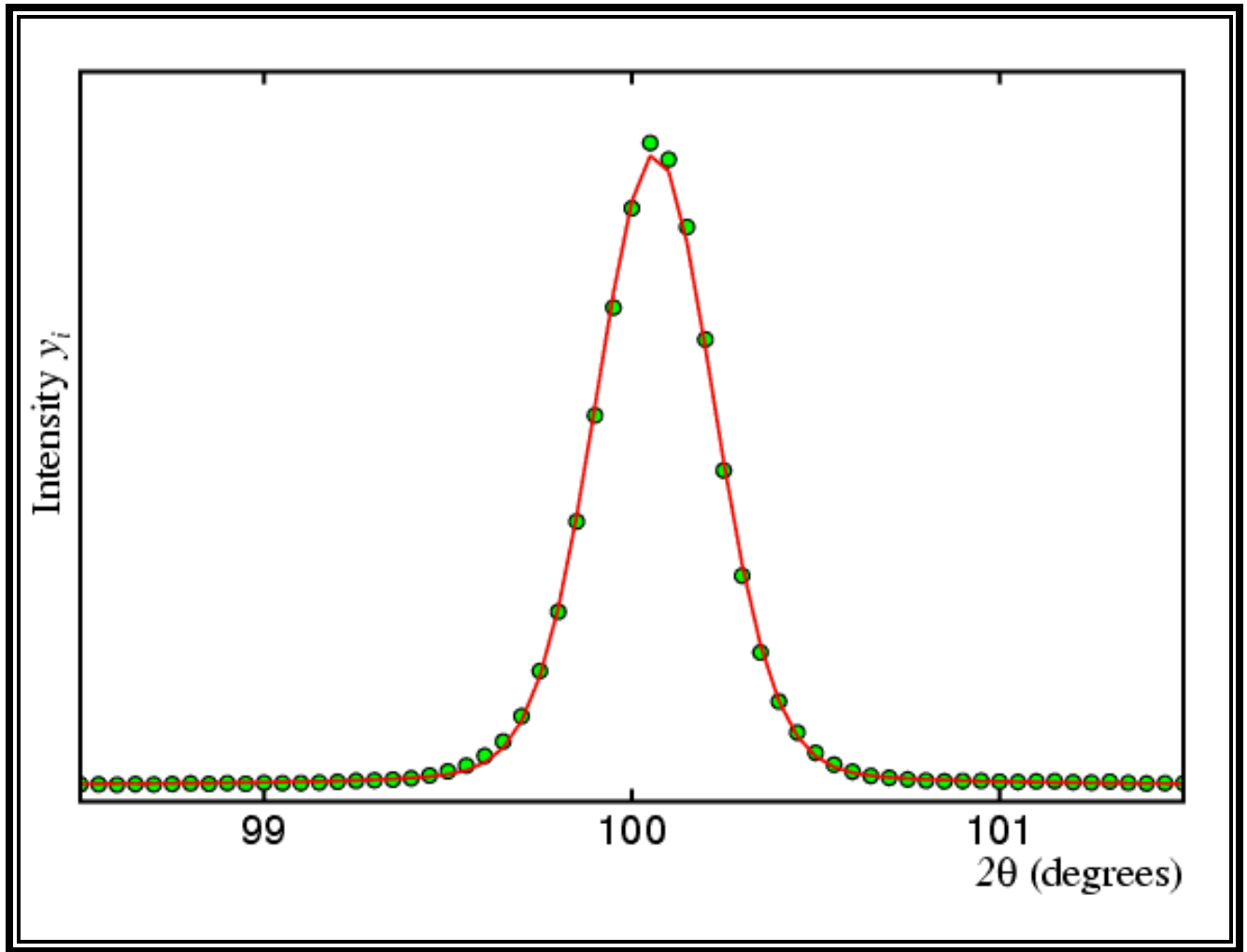


Figure 3.5: The green dots shows the powder diffraction pattern of the 220 reflection of nickel metal as measured on the powder neutron diffractometer D1A at the ILL, Grenoble. The data has been fitted using a Gaussian peak-shape function as shown by the solid red line. The very minor deviation in the experimental data away from Gaussian behaviour is a sample effect due to the particular nickel powder used for this measurement..

This is demonstrated in Figure 3.6 for part of a powder diffraction pattern profile shown in red, which is due to the presence of two reflections shown in green and blue. The intensity contribution to the profile at the point i is simply given by

$$y_i(3) = y_i(1) + y_i(2) \quad (3.11)$$

In practice, the powder diffraction profile has a background count attributable to variety of factors: instrumental background count, incoherent scattering, inelastic scattering, thermal diffuse scattering, electronic noise, etc., in addition to the sharp Bragg diffraction peaks. An expression for the peak width as a function of scattering angle had been derived theoretically many years previously by Cagliotti, Paoletti, & Ricci as:

$$H^2 = U \tan^2 \theta + V \tan \theta + W \quad (3.12)$$

This is simply a parabolic function in $\tan \theta$ characterized by 3 peak-width parameters, U , V , W . This simple formula not only describes the instrumental resolution of a powder diffractometer, but to some extent takes into account sample effects such as particle size which slightly can broaden the diffraction peak.

The quantity Δ that is minimized is given by the expression:

$$\Delta = \sum_i w_i \{y_i(obs) - y_i(calc)\}^2 \quad (3.13)$$

$$\Delta = \sum_i w_i \{y_i(obs) - \sum_{hkl} \sqrt{4 \ln 2 / \pi} c_j L(2\theta) F^2(hkl) e^{-4 \ln 2 (x_i - 2\theta_{hkl})^2 / H^2} / H - y_i(back)\}^2 \quad (3.14)$$

where

w_i is a weight attributed to each observation, and

$$F(hkl) = \sum_n b_n N_n e^{2\pi i(hx_n + ky_n + lz_n)} e^{-B_n \sin^2 \theta / \lambda^2} \quad (3.15)$$

The parameters in the Rietveld method may be summarized into two distinct groups as follows:

Table 3.6 Parameters in the Rietveld method

Instrumental			Structural	
2_{zero}	Instrumental zero error		c	Overall scale factor
A, B, C, D, E, F	Unit cell metric tensor		x_n, y_n, z_n	Fractional atomic coordinates
U, V, W	Peak width parameters		B_n	Isotropic temperature factor <i>or</i>
P, \dots , etc.	Peak shape parameter(s)		$_{ij}$	Anisotropic temperature factor
G	Preferred orientation parameter		N_n	Site occupation factor

It is important to realize that the parameters in the left of the table affect mainly peak position and shape, while those on the right relate directly to the reflection intensity and hence to the structure factor itself.

The above discussion focused around the use of angle-dispersive neutron diffractometry to obtain refined structural parameters from powder data. The same method could, in principle, be extended to the fitting of powder diffraction data obtained using both laboratory and synchrotron X-rays. All that is required is a few minor modifications to the basic code: firstly, X-ray form factors, $f(2\theta)$, must be used instead of the neutron scattering lengths, b , in the calculation of the structure factors; secondly, a polarisation correction, $P(2\theta)$, must be included in addition to the Lorentz factor for data collected with laboratory X-rays, together with an absorption correction, $A(2\theta)$, for data collected in capillary geometry; thirdly, a different (non-Gaussian) peak-shape function is required.

There has been much discussion on the latter subject with respect to laboratory data: the peak-shape function is highly dependent on the instrumental setup. For laboratory diffractometers with a narrow-bandpass primary-beam monochromators, and for most synchrotron diffractometers also, the pseudo-Voigt peak-shape function is empirically found to be most suitable. For diffractometers with only nickel filters or graphite monochromators, peak shapes based on less symmetric functions are preferred; alternatively, peak shapes based on so-called fundamental parameters have been heavily promoted by some code developers.

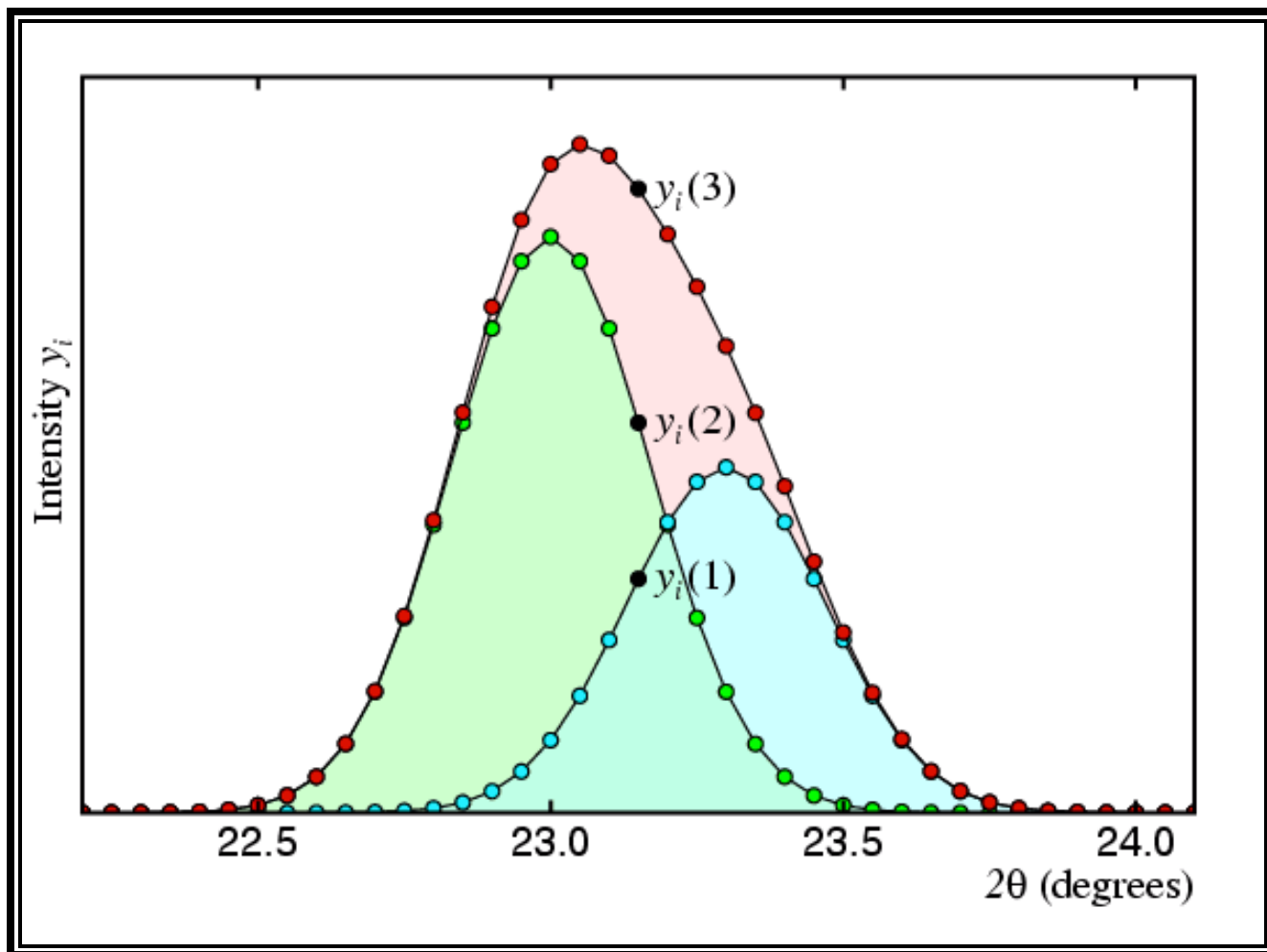


Figure 3.6: The intensity contribution at point i is calculated by summing the individual intensities of the two separate peaks.

The applicability of the Rietveld method to the X-ray case has probably led to a much wider exploitation than that originally envisaged. More importantly, the extension to the X-ray case has resulted in better-quality, higher-resolution, X-ray data being collected, together with improvements in the design of X-ray powder diffractometers.

3.3.6 Pawley Method

In order to solve a structure from powder data it is necessary to extract as many hkl and intensity values as possible from the data set. Until the 1980s, this wasn't feasible due to the overlapping nature of the peaks in the powder diffraction profile. However, with the development of high-speed computers with large memories and high-resolution diffractometers, pattern decomposition became a viable and

important part of the analysis of powder data. All the methods use pattern decomposition rather than deconvolution because the exact peak-width function is not known *a priori*, but in effect the end result is similar. There are two methods that are in common usage at the present time. The first is due to Pawley (1980) and the second is due to LeBail (1988). Pawley suggested that angle-dispersive powder diffraction profiles could be fitted with only the following parameters:

- $I(hkl)$ - Intensity of each reflection with indices hkl ;
- A, B, C, D, E, F - Unit-cell metric tensors or parameters;
- 2_{zero} - Instrumental zero error;
- U, V, W - Peak-width parameters;
- , etc. - Other peak-shape parameters.

Many of the parameters are the identical to those used in a Rietveld refinement program, but the significant difference is that *every* reflection is assumed to have (i) a peak position determined by A, B, C, D, E, F , and the 2_{zero} error, (ii) a peak width determined by the resolution function parameters U, V , and W , and (iii) a peak intensity $I(hkl)$. This can be contrasted to the Rietveld method, in which the intensity of the peaks is calculated from the structure factors, $F(hkl)$, which are themselves calculated from the parameters of the model structure.

In terms of a least-squares minimization procedure, this requires typically a $(10+N) \times (10+N)$ square matrix, where N is the number of symmetry-independent reflections generated for the 2_{zero} range covered by the data. So for 200 reflections, this will require computer memory of only approximately 170 kilobytes, but for 2000 reflections, the memory required for the matrix alone will be 16 Mbytes.

As described, the method has two problems, the first of which is illustrated by the following set of figures, in which the observed profile (or total count) is shown in red and the contributions of two peaks A and B are shown in blue and green, respectively. In Figure 3.7, the two peaks are fairly well separated and there is little correlation between their intensity values as obtained by least-squares fitting of the observed profile. In Figure 3.8, the two peaks are now closer together and any peak intensity values derived from the profile will start to show correlation.

In Figure 3.9, the two peaks are now so close together that any least-squares procedure risks producing incorrect intensity values for the two peaks. The blue and green peaks have an actual intensity

ratio of 5 to 3, but the smallest of errors in either the observed profile shown in red or the peak profile used to described the two peaks shown in blue and green could lead to ratios such as 10 to 1, say, or even 1 to 10 (or worse) for their fitted intensity ratio.

Thus, there is a large correlation in the values of $I(hkl)$ for peaks that are nearly coincident with the correlation rising to 100% for peaks that have the same d spacing within the limits of resolution of the data. Large correlations lead to unstable (and ultimately singular) least-squares matrices. An extreme example of the problem of near 100% correlation is illustrated in Figure 3.10.

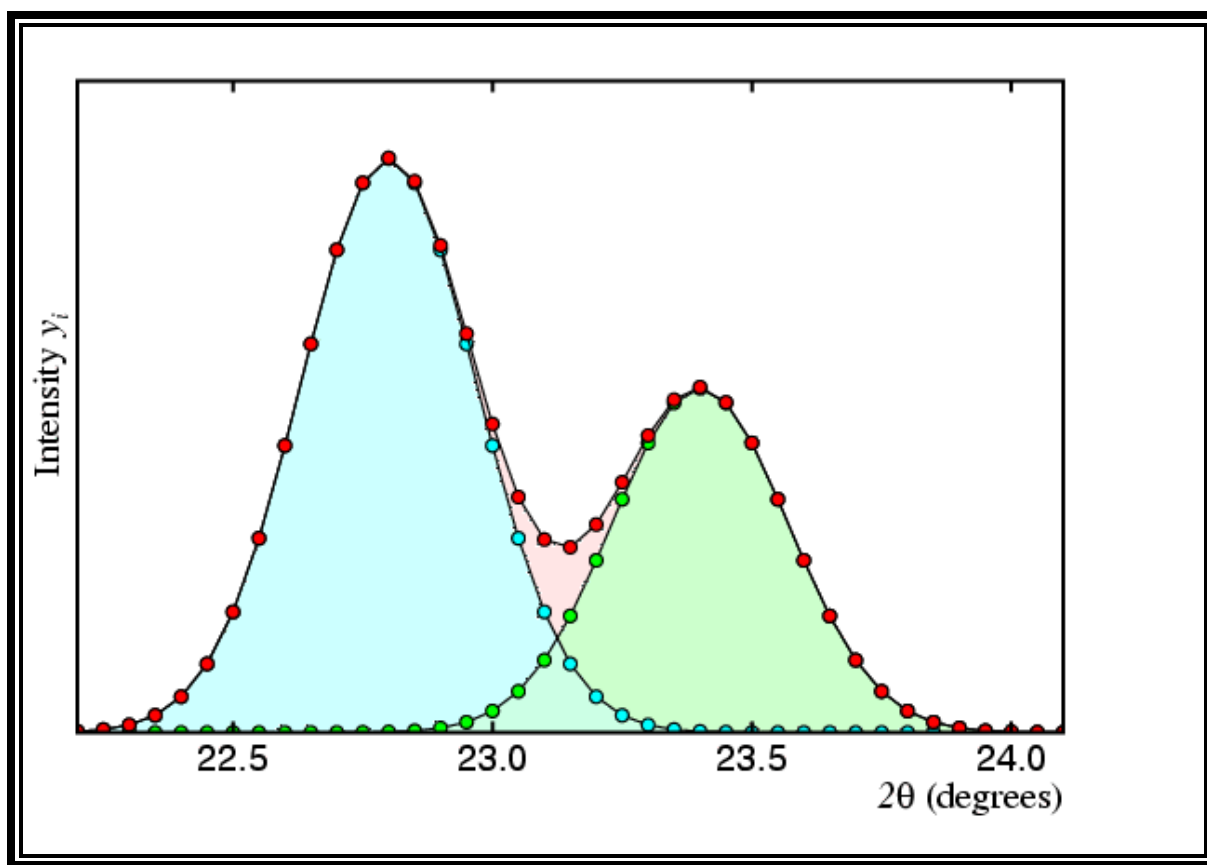


Figure 3.7: The two peaks are fairly well separated and there is little correlation between their intensity values as obtained by least-squares fitting of the observed profile.

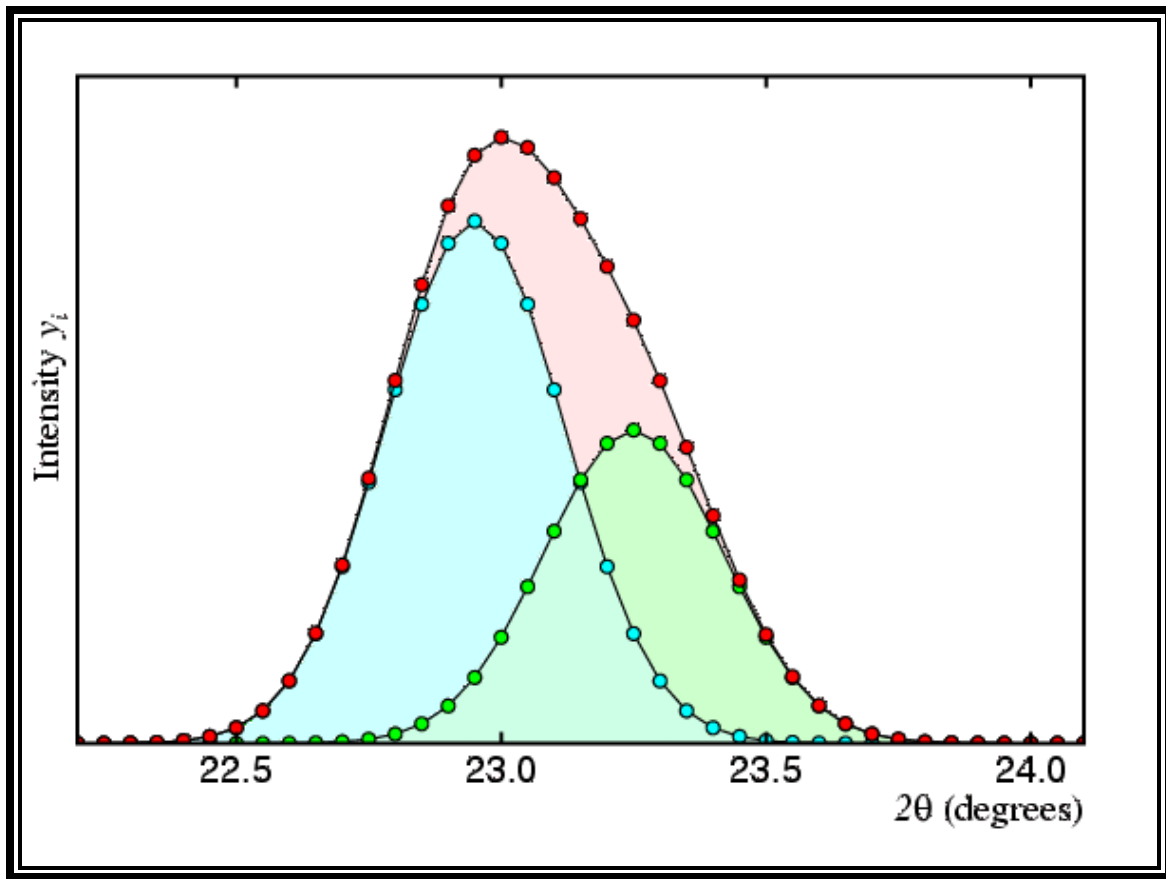


Figure 3.8: The two peaks are now closer together and any peak intensity values derived from the profile will start to show correlation.

Here the observed profile is shown fitted to two peaks, one of which is much bigger than the total observed intensity, and the other of which is negative. There is nothing in the least-squares procedure that forces the peaks to have positive intensity, despite the fact that $I(hkl)$ must be positive to be meaningful.

Pawley reduced the correlations by introducing both constraints and restraints into the least-squares procedure: as the difference between the calculated 2θ values of two adjacent peaks approaches zero, the following equality is applied:

$$I_1(hkl) = I_2(hkl) \quad (3.16)$$

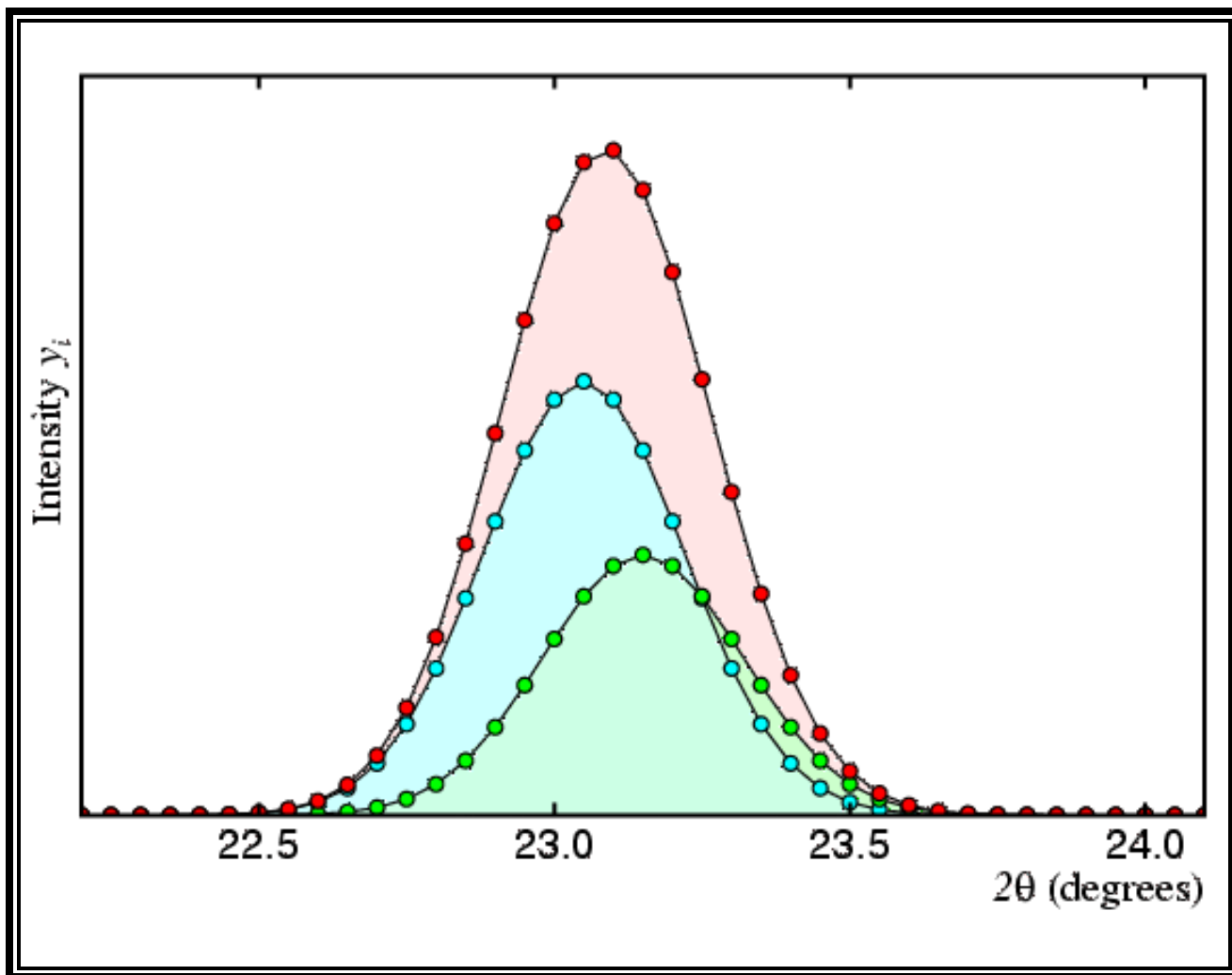


Figure 3.9: The two peaks are now so close together that any least-squares procedure risks producing incorrect intensity values for the two peaks.

When the 2θ is less than, say, the step size, this information is introduced as a hard constraint in the refinement procedure: when the value is larger, it is used as a soft restraint. While the above equality attempts to avert the problem of negative intensities, it may not prevent them completely, and so negative $I(hkl)$ values may occasionally be obtained in the output from programs that use the method as described. An alternative approach is to base the refinement on $|F|$ instead of I . This forces the peak intensities to have positive values only, but computer programs that use this method take much longer to run.

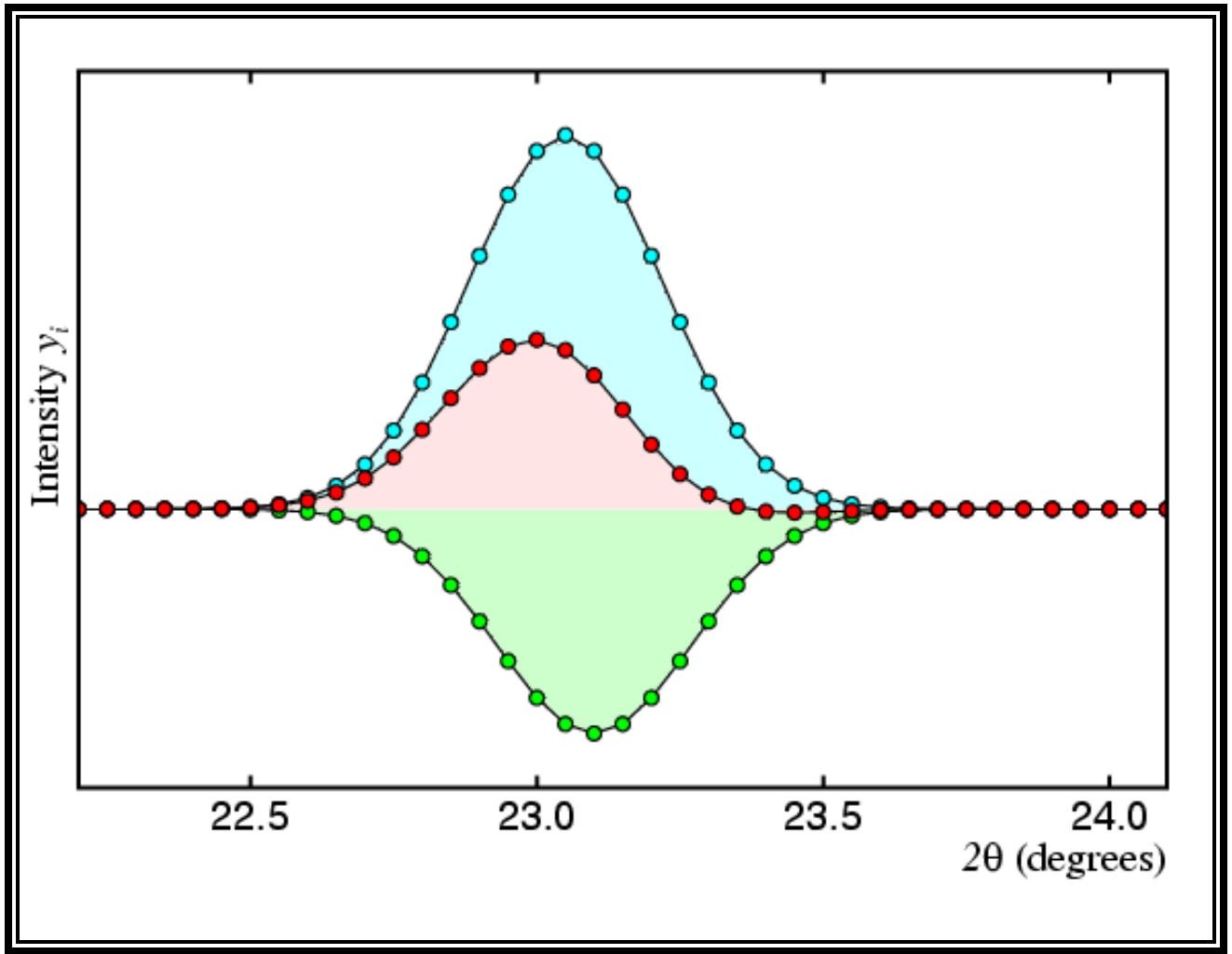


Figure 3.10: An extreme example of the problem of near 100% correlation.

A second problem concerns the wasted array space and computer time used to fill it. Most of the least-squares matrix is filled with zeros when the value of N_{hkl} is large. This is because the matrix contains many terms for each point i in the profile y_i of the type:

$$\sum_i \frac{dy_i}{dI_j} \times \frac{dy_i}{dI_k} \quad (3.17)$$

where I_j and I_k are the intensity parameters of the j^{th} and k^{th} reflections. These terms are zero for peaks that are well-separated and non-overlapping, but still require calculation and storage. Worse still, they are required for the inversion of a "full least-squares" matrix.

This is really a computer science problem and not one intrinsic to the method, so though it was in the 1980's when computers were slower and more memory limited than now. One solution to the above

problem is to reduce the matrix to smaller units by block diagonalization, in which only the elements close to the diagonal of the matrix are considered for the lower-value d spacings.

As a consequence of these two problems with the Pawley method, the LeBail method of whole pattern fitting was developed. This led to an enormous increase in the use of whole pattern fitting and, moreover, stimulated improvements in the Pawley method itself.

3.3.7 Le Bail Fit

The Fullprof software which we initially use to refine our structure uses a Le Bail fit. The method uses a two-step cyclic process. As with the Pawley method, the following parameters are fitted by a standard least-squares methods:

- A, B, C, D, E, F - Unit-cell metric tensor parameters;
- 2_{zero} - Instrumental zero error;
- U, V, W - Peak-width parameters;
- , etc. - Other peak-shape parameters.

This time, however, the intensities of the individual peaks are no longer treated as least-squares parameters and are never refined. Consequently, each cycle of least-squares is very fast since the matrix remains small.

Initially, all of the peak intensities are set to an arbitrary value, e.g. 1000.0. These are treated as "calculated" values as if they had been derived from a structural model. Application of Rietveld's procedure for partitioning observed profile points, $y(\text{obs})$, leads to a set of "observed" intensity values. In Figure 3.11, the observed profile is shown as a red line with white dots and the calculated is shown as a black line with red dots. The observed total intensity of peak 1 (shown in blue) is given by the expression:

$$I_{\text{obs}}(1) = \sum_i y_i(\text{obs}) \times y_i(1) / y_i(\text{calc}) \quad (3.18)$$

Likewise, for the total intensity of peak 2 (shown in green):

$$I_{\text{obs}}(2) = \sum_i y_i(\text{obs}) \times y_i(2) / y_i(\text{calc}) \quad (3.19)$$

where $y_i(\text{calc}) = y_i(1) + y_i(2)$, and the summation is taken over all profile points i that may contribute to peak intensity. This method, which is sometimes referred to as "profile intensity partitioning", works for any number of overlapping peaks and is not restricted to just two peaks as used for this illustration.

These "observed" intensity values will be biased by the starting values used for $I(\text{calc})$, but on average they will still be closer to the true value for the observed $I(hkl)$ than any arbitrary value. These observed values can now be used instead of a structural model for the least-squares fitting of the diffraction profile. This leads to an improvement in (a) cell parameters and, consequently, peak positions, (b) resolution function parameters, i.e. peaks widths, and (c) peak shape parameters. The process is now iterated and a fresh set of observed intensities are obtained. The whole process is shown in Illustration 3.5

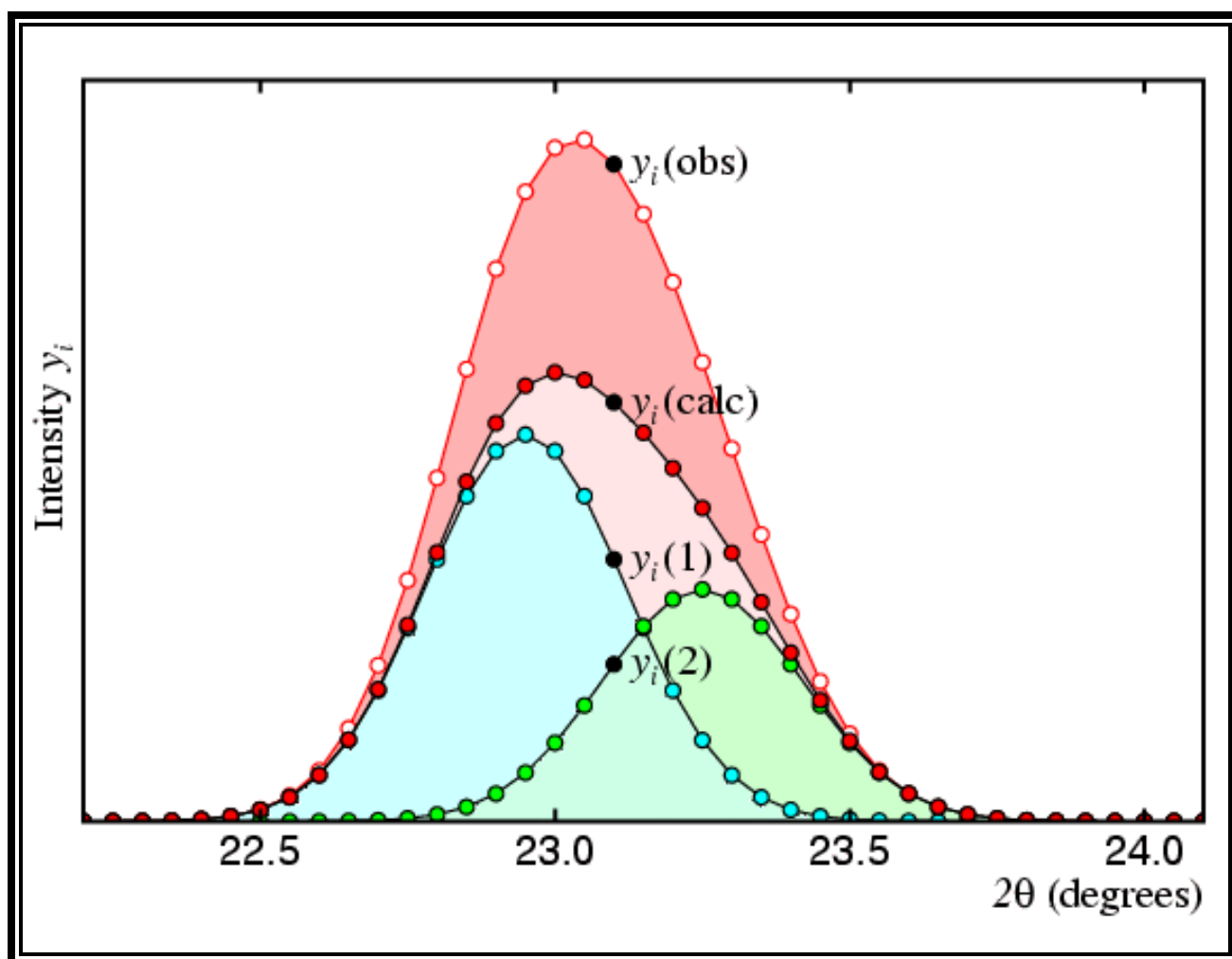


Figure 3.11: Overlapping peaks can be summed and simplified into a single peak using profile intensity partitioning.

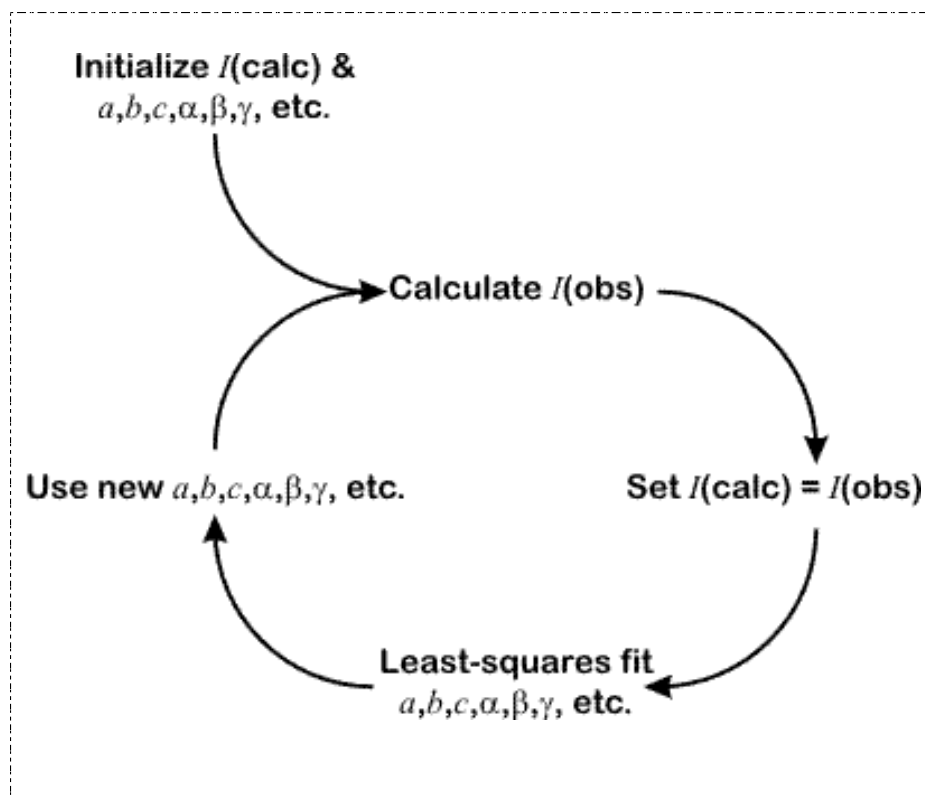


Illustration 3.5: An overview of the process used by the Le Bail method.

Because the process is of an iterative nature, and because least-squares is avoided for determining $I(\text{obs})$, the whole process converges somewhat slowly. (It is not immediately obvious that such a process will converge at all.) Typically, 10s to 100s of cycles are required, but given the very rapid speed of each cycle, this is not a problem in practice. Note that since $I(\text{calc})$ is set equal to $I(\text{obs})$ during each cycle, then the intensity R -factor will tend to zero.

Assuming that the background is determined correctly, and not overestimated, then programs that employ the LeBail method can never produce negative peak intensities.

Comparison of Pawley & LeBail methods

How do the two methods compare? This question provides much controversy between the "purists" and the "pragmatists". The former argue strongly that only the Pawley method should be used since this provides not only intensities, but esd values as well. The latter argue in favor of the speed offered by the LeBail method, and its general availability: what is the point in having mathematically perfect programs if they are not readily available "off-the-shelf" to all users? There are merits and

imperfections with both methods, though the issue of speed is now becoming less important given the availability of high-speed personal computers.

Both methods intrinsically have a problem with peaks that severely overlap. This is less of a problem for the low-symmetry crystal systems (triclinic to orthorhombic) since peaks with near identical d spacings only occur randomly. However, the problem is particularly severe for the higher symmetry crystal systems since it is impossible to derive reliable peak intensities for the Laue classes $4/m$ (which is indistinguishable from $4/mmm$ by powder diffraction), -3 , $3m1$, $31m$, $6/m$ (all of which are indistinguishable from $6/mmm$), and $m-3$ (which is indistinguishable from $m-3m$). As well as peak overlap due to Laue symmetry, there are a significant number of special cases, particularly for the cubic crystal system even in the higher Laue class $m-3m$: a simple example is the identical d spacings of the 500 and 430 reflections, i.e. reflections where the sum of the indices squared are equal. In all of these cases, the profile decomposition software simply partitions the intensities equally, even though this is unlikely to be the case; hence the difficulty of structure determination from powder diffraction with the high symmetry crystal systems.

Chapter 4: Experimental Methods

In order to study the superprotonic transition of CsH_2PO_4 and RbH_2PO_4 , their powders were initially characterized at room temperature through laboratory x-ray diffraction. Several different synchrotron X-ray powder diffraction experiments were then run at the National Synchrotron Light Source (NSLS), Brookhaven National Laboratory. CDP and RDP were first studied under ambient-pressure conditions to try to determine whether we could observe a structural phase transition under these conditions. In the temperature resolved synchrotron experiments, diffraction measurements were taken at temperature intervals of 5°C from room temperature to 250°C . Since synchrotron radiation was used and the diffraction data was collected all at once, the measurements for each temperature interval could be collected in less than a minute allowing us to collect a lot of data in very little time compared to using a laboratory diffractometer. Another set of temperature-resolved diffraction measurements were then taken with samples of CDP and RDP under high-pressure conditions. These experiments employed an energy-dispersive X-ray method in order to carry out the measurements at a constant measuring angle. These experiments are described in more detail below.

4.1 SAMPLE PREPARATION

MH_2PO_4 monocrystals ($\text{M} = \text{Cs}, \text{Rb}$) were grown by slow evaporation from an aqueous solution prepared by mixing stoichiometric amounts of H_3PO_4 and M_2CO_3 which go through the following chemical reaction



The resulting crystals were subsequently ground to a fine powder. The form of the specimen used was an elliptical cylinder with diameters in the range 0.3-0.5 mm and a height of about 0.5 mm. The samples were initially characterized at room temperature by laboratory x-ray diffraction using a Siemens D5000 diffractometer.

4.2 AMBIENT-PRESSURE CONDITIONS

Synchrotron X-ray powder diffraction measurements under ambient-pressure were performed on the X7B beamline at the NSLS, using X-rays of wavelength 0.922\AA selected by a double flat-crystal monochromator. The diffracted beams were detected on a Mar345 flat image plate. Images were

collected upon heating MH_2PO_4 polycrystals in 10°C steps from room temperature to 300°C . An exposure time of 45 seconds was used at each temperature. Eventually, the images were processed into intensity vs. diffraction angle (2θ) patterns by integrating over the projections of the Debye-Scherrer cones onto the flat detector using the FIT2D software.³⁰ The resulting data was then analyzed using the Fullprof software to obtain the crystal lattice type.

Figure 4.1: Parameter file used to fit powder diffraction data in Fullprof.

```

cubic.pcr - Notepad
File Edit Format View Help
COMM Superprotonic CsH2PO4
! Current global Chi2 (Bragg contrib.) = 7.030
! Files => DAT-file: cubic, PCR-file: cubic
! Job Npr Nph Nba Nex Nsc Nor Dum Iwg Ilo Ias Res Ste Nre Cry Uni Cor Opt Aut
! 0 12 1 19 2 0 1 1 0 0 1 0 0 0 0 0 0 0 0 0
!
! Ipr Ppl Ioc Mat Pcr Ls1 Ls2 Ls3 NLI Prf Ins Rpa Sym Hkl Fou Sho Ana
! 0 2 1 1 1 0 0 0 0 -3 10 1 1 1 0 0 0
!
! lambda1 Lambda2 Ratio Bkpos wdt Cthm muR AsyLim Rpolaz ->Patt# 1
! 0.922000 0.922000 1.0000 15.100 25.0000 0.0000 0.0000 35.00 0.0000
!
! NCY Eps R_at R_an R_pr R_gl Thmin Step Thmax PSD Sent0
! 2 0.30 0.50 0.50 0.50 0.50 0.0108 0.021749 49.9891 0.000 0.000
!
! 2Theta/TOF/E(Kev) Background for Pattern# 1
! 7.800 5010.084 0.000
! 9.209 4875.630 0.000
! 11.605 5447.059 0.000
! 12.732 5581.513 0.000
! 13.930 5329.412 0.000
! 15.550 4539.496 0.000
! 16.678 3749.580 0.000
! 19.355 3043.698 0.000
! 20.412 2926.051 0.000
! 22.737 2640.336 0.000
! 24.992 2472.269 0.000
! 28.092 2186.555 0.000
! 29.290 2119.328 0.000
! 33.165 2152.941 0.000
! 36.829 2085.715 0.000
! 39.859 2152.941 0.000
! 42.466 2085.715 0.000
! 44.227 2001.681 0.000
! 45.848 1900.840 0.000
!
! Excluded regions (LowT HighT) for Pattern# 1
! 0.00 7.00
! 47.00 70.00
!
! 2 !Number of refined parameters
!
! Zero Code SyCos Code SySin Code Lambda Code MORE ->Patt# 1
! 0.00396 21.00 0.00000 0.00 0.00000 0.00 0.000000 0.00 0
!
!-----

```

Figure 4.1: Parameter file used to fit powder diffraction data in Fullprof.

The Fullprof program matches the calculated and observed Bragg peaks by allowing the user to input different variables such as lattice parameters and peak profiles in order to match the observed graph produced by the Fit2D program to a calculated graph as described in Section 3.2.7. Figures 4.1 and 4.2 show the parameter file one can create to try to match to an observed graph.

```

cubic.pcr - Notepad
File Edit Format View Help
! Excluded regions (LowT HighT) for Pattern# 1
  0.00 7.00
 47.00 70.00
!
!
!      2      !Number of refined parameters
!
! Zero   Code   SyCos   Code   Sysin   Code   Lambda   Code MORE --> Patt# 1
! 0.00396 21.00 0.00000 0.00 0.00000 0.00 0.000000 0.00 0
! -----
! Data for PHASE number: 1 ==> Current R_Bragg for Pattern# 1: 0.00
! -----
Csh2Po4
! Nat Dis Ang Pr1 Pr2 Pr3 Jbt Irf Isy Str Furth ATZ Nvk Npr More
! 0 0 0 0.0 0.0 1.0 2 0 0 0 0 0.000 0 12 0
!
! P m 3 m <--Space group symbol
! -----> Profile Parameters for Pattern # 1
! Scale Shape1 Bov Str1 Str2 Str3 Strain-Model
! 0.10000E-03 0.00000 0.00000 0.00000 0.00000 0.00000 0
! 0.00000 91.000 0.000 0.000 0.000 0.000
! U V W X Y GauSiz LorsiZ Size-Model
! -0.242817 0.074506 0.040402 0.000000 0.000000 0.000000 0.000000 0
! 31.000 41.000 51.000 111.000 101.000 0.000 0.000
! a b c alpha beta gamma #Cell Info
! 4.951674 4.951674 4.951674 90.000000 90.000000 90.000000
! 11.00000 11.00000 11.00000 0.00000 0.00000 0.00000
! Pref1 Pref2 Asy1 Asy2 Asy3 Asy4
! 1.00000 0.00000 0.00000 0.00000 0.00000 0.00000
! 0.00 0.00 0.00 0.00 0.00 0.00
! Additional asymmetry parameters (S_L, D_L)
! 0.00300 0.00 0.00300 0.00
! Shape: shp1 cshp1 & shp2 cshp2

```

Figure 4.2: Lattice parameters calculated with the Fullprof program.

Figure 4.1 shows variables such as peak profile parameters and instrument background points. Figure 4.2 shows the lattice parameters used to make the theoretical match. The variables in Figure 4.1 affect the shape of the peak. When these profile parameters are off, they program produces a bad fit even if the peak positions are correct as can be seen in Figure 4.3. The lattice parameters, on the other hand, affect the position of the Bragg peaks and can lead to a wrong structure even if the profile parameters are correct as can be seen in Figure 4.4.

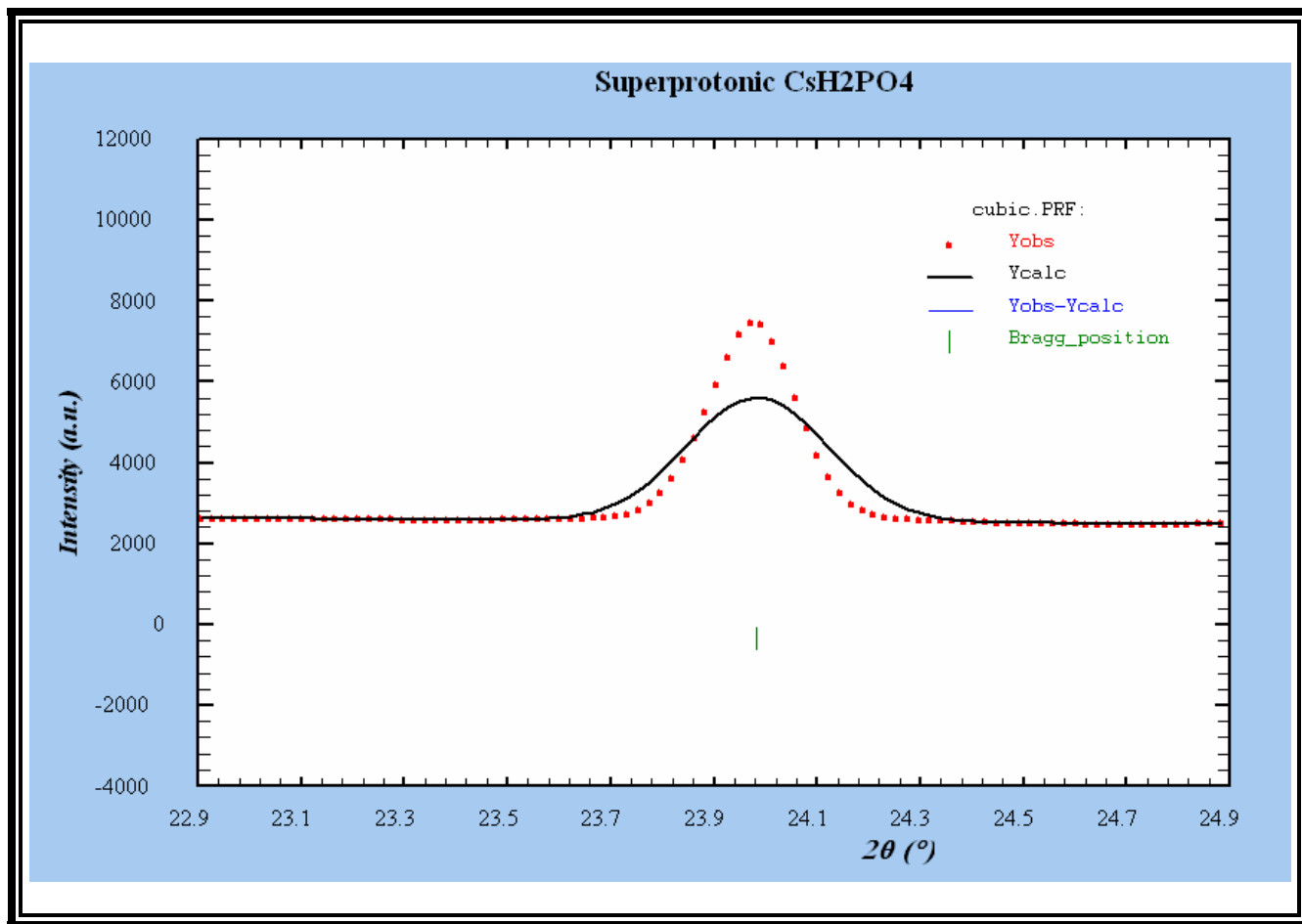


Figure 4.3: Correct peak positions with bad profile fit.

In order to produce a good match, therefore, both the peak profiles and the peak positions must be accurately matched to the observed data. χ^2 is a measure of how well the calculated and observed graphs match. In theory, a value of 1 for χ^2 is a perfect match. Figure 4.5 shows a very good fit with a χ^2 value between 1 and 2. This method was used to analyze the data obtained from the ambient pressure experiments.

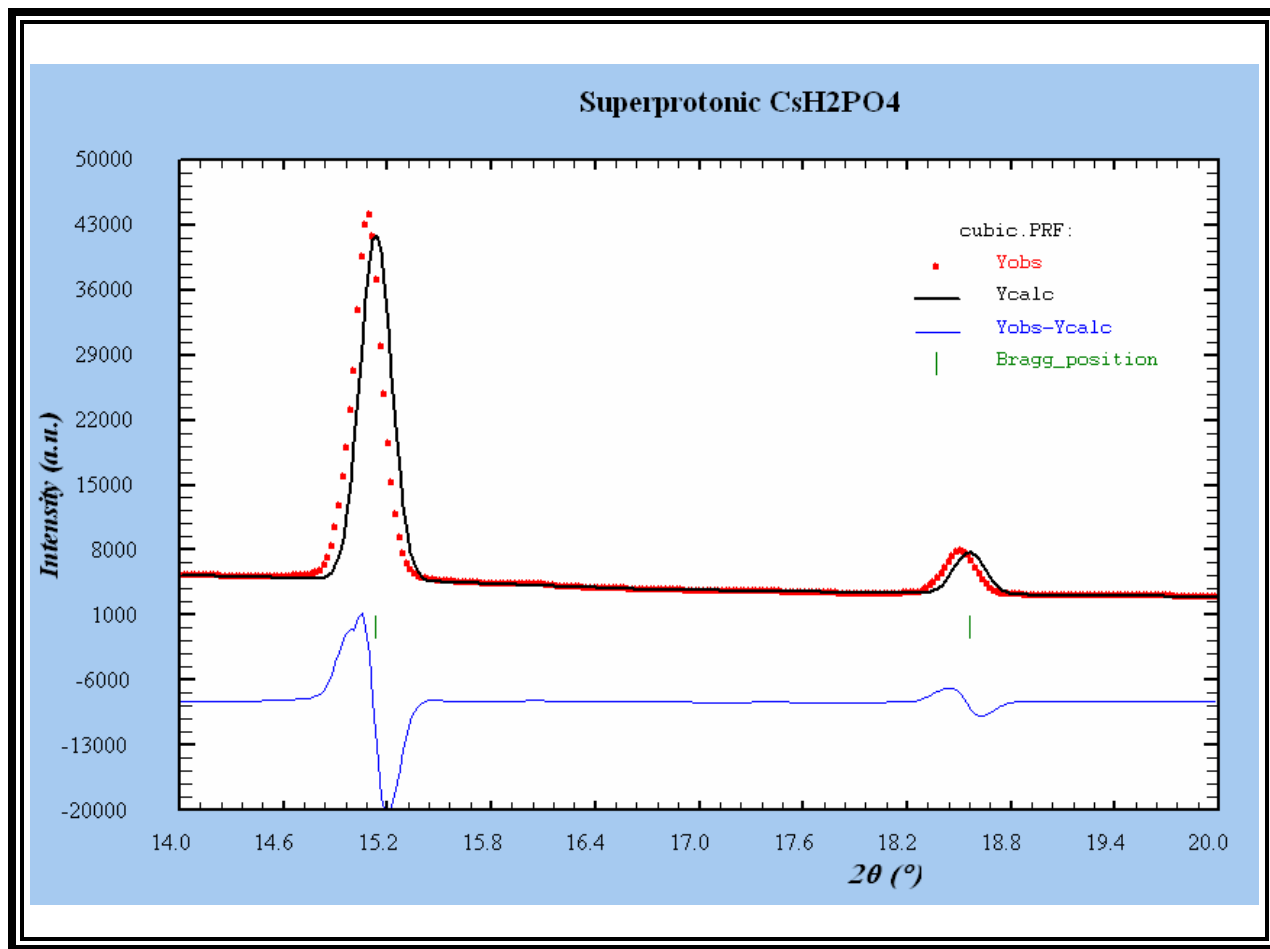


Figure 4.4: Good profile fit with incorrect peak positions.

4.3 HIGH-PRESSURE CONDITIONS

The high-pressure experiments were performed using a DIA-type, large-volume apparatus (SAM85) designed for in-situ X-ray diffraction studies at simultaneously high pressure and temperature.³¹ An energy-dispersive x-ray method was employed using white radiation from the superconducting wiggler magnet at beamline X17B2 of the NSLS. The incident x-ray beam was collimated to dimensions of $100 \times 100 \mu\text{m}$, and the diffracted x-rays were collected at a fixed angle of $2\theta = 6.485^\circ$. The cell assembly was similar to that described in Ref [31]. Briefly, a mixture of amorphous boron and epoxy resin was used as pressure-transmitting medium, and amorphous carbon was used as furnace material.

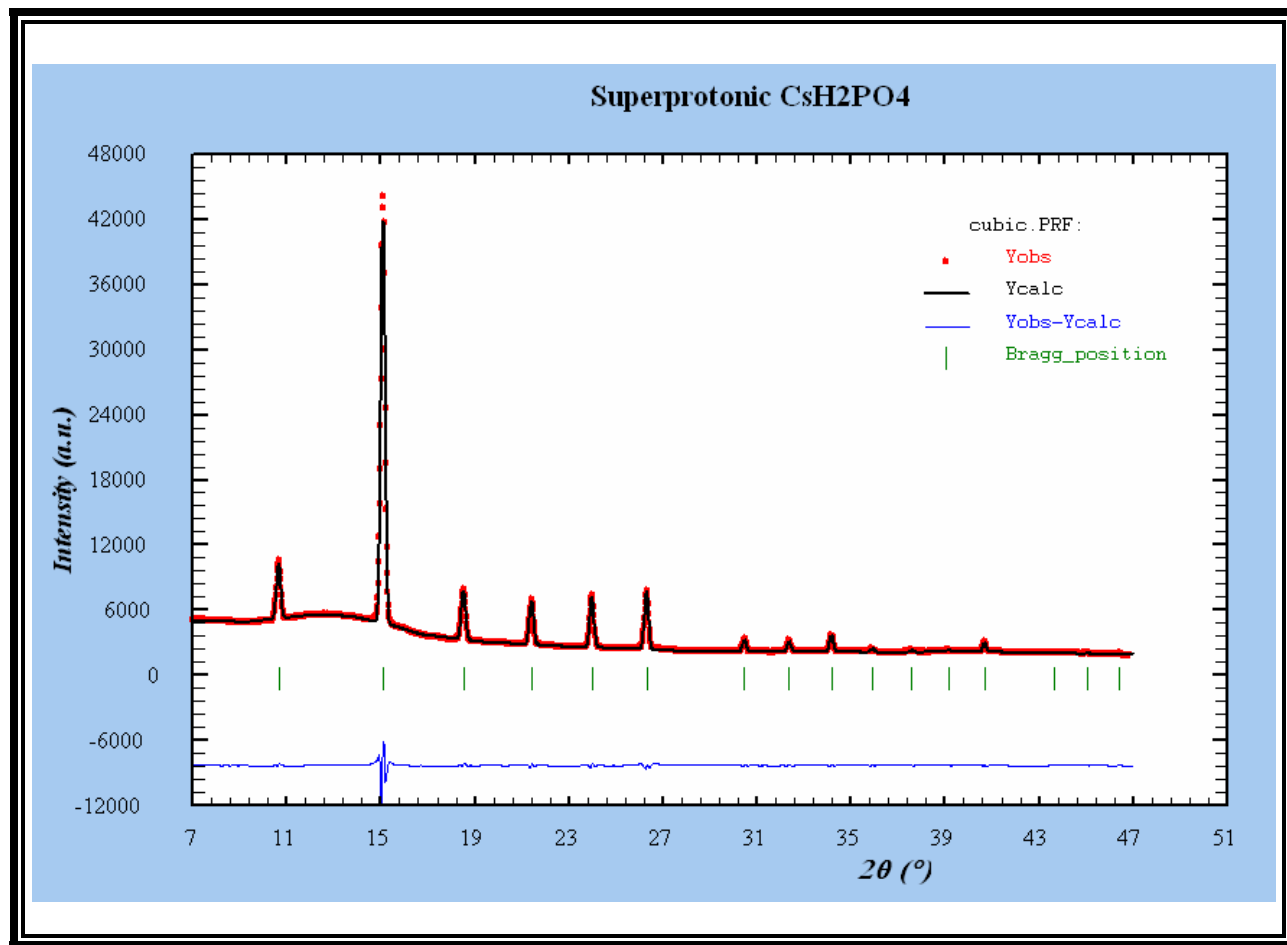


Figure 4.5: Excellent fit indicating a high temperature cubic phase.

Two layers of powder samples of MH₂PO₄ and NaCl were packed into a boron nitride container of 1 mm diameter and 2 mm length, with NaCl serving as an internal pressure standard. The counting time for the collection of each diffraction pattern was 2-3 minutes for NaCl and 5 minutes for MH₂PO₄. Pressures were calculated from Decker's equation of state for NaCl²³ using lattice parameters determined from x-ray diffraction profiles at each experimental condition. Five NaCl diffraction lines, 111, 200, 220, 222 and 420, were usually used for determination of pressure. The uncertainty in pressure measurements is mainly attributed to statistical variation in the positions of diffraction lines and is less than 0.1 GPa in the pressure range of the study.

The temperature was measured by a W/Re25%-W/Re3% thermocouple that was positioned at the center of the furnace in direct contact with the sample and the NaCl layers. For the actual experiment the samples were initially compressed at room temperature to 1.02 GPa followed by heating in steps of 20-

30°C up to 300°C. At each temperature step powder diffraction data corresponding to a 1-6Å d-spacing range were collected. Temperature variations over the entire sample length were of the order of 20°C at 1225°C and the radial temperature gradient was less than 5°C at this condition³. X-ray diffraction patterns were obtained for both samples and NaCl in close proximity to the thermocouple junction; errors in temperature measurements were estimated to be less than 10°C. No correction was applied for the effect of pressure on the thermocouple emf. The diffraction pattern images were then analyzed using the same methods as those described for the ambient-pressure experiment.

Chapter 5: Results & Discussion

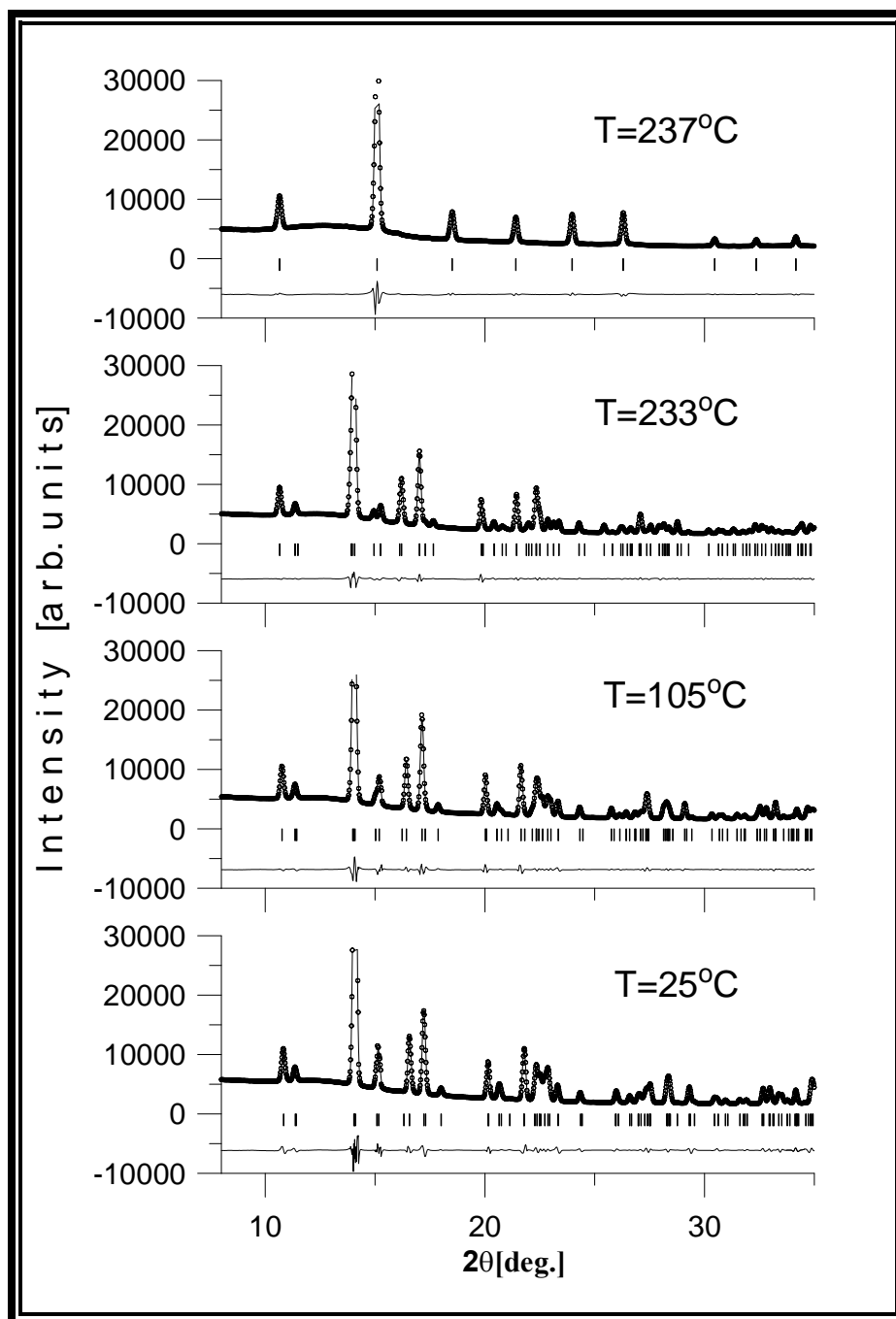


Figure 5.1: Le Bail fits to synchrotron X-ray powder diffraction patterns for CsH_2PO_4 measured at different temperatures under ambient pressure. The open symbols are the observed intensities (I_{obs}), the solid line is the best fit (I_{calc}), and the lower trace is the difference curve ($I_{\text{obs}} - I_{\text{calc}}$). The vertical bars indicate the positions of the Bragg reflections. A transition from the room-temperature monoclinic phase ($P2_1/m$; $a=7.90\text{\AA}$, $b=6.39\text{\AA}$, $c=4.87\text{\AA}$, and $\beta=107.64^\circ$) to a high-temperature cubic phase ($Pm\bar{3}m$; $a=4.96\text{\AA}$) occurs at $T=237^\circ\text{C}$

5.1 CsH₂PO₄ & RbH₂PO₄: AMBIENT PRESSURE CONDITIONS

Figure 5.1 shows the X-ray powder diffraction pattern of CsH₂PO₄ measured under ambient-pressure conditions at four different temperatures ranging from 25-237°C. The room temperature peaks were indexed using the unit cell and space group corresponding to the known crystal structure of CsH₂PO₄ (P2₁/m; a=7.90 Å, b=6.39 Å, c=4.87 Å, and β =107.64°).¹³ Our data indicates that this phase remains relatively unchanged during heating up to 232°C, with no unindexed peaks at any temperature in the 25-232°C range. (Figure 5.2 shows the smooth variation of the lattice parameters in this temperature range.) As can be seen in the uppermost graph of Figure 5.1 however, the peak pattern changes dramatically at 237°C, which suggests a structural transition to a high-symmetry phase. And as it turns out, this diffraction pattern actually corresponds to a Pm3m cubic structure (a=4.96 Å).

The existence of a cubic high-temperature phase of CsH₂PO₄ was first proposed by Baranov *et al.* in an optical microscopy study¹⁸. More recently, however laboratory X-ray diffraction studies by Preisinger *et al.* showed a monoclinic \rightarrow cubic phase transition at about 230°C for samples heated in a H₂O-saturated atmosphere³². However, the same study concluded that under ambient conditions, dehydration and decomposition of the sample occurs below the transition temperature and therefore no transition to the cubic phase is observed. Our experiment demonstrated, for the first time, that a single high-temperature cubic phase of CsH₂PO₄ can be observed even in the absence of H₂O-saturated atmospheric conditions. This phase however, turned out to be unstable in time.

Figure 5.3 shows the time-resolved X-ray powder diffraction patterns of CsH₂PO₄ measured under ambient pressure and humidity at 237°C. We found that the peak patterns of CsH₂PO₄ began to change away from the cubic phase peak positions as quickly as 15 minutes after the monoclinic \rightarrow cubic phase transition is observed. This instability is most likely due to chemical modifications and dehydration in which CsH₂PO₄ is partially decomposed into Cs₂H₂P₂O₇ through the following reaction:



The fact that the cubic phase of CsH₂PO₄ is only stable for such a short time, may explain the differences between our results and those of Preisinger *et al.* The key difference in experimental procedures was the data collection time at each temperature, ours being of the order of minutes while theirs was probably of the order of several hours³².

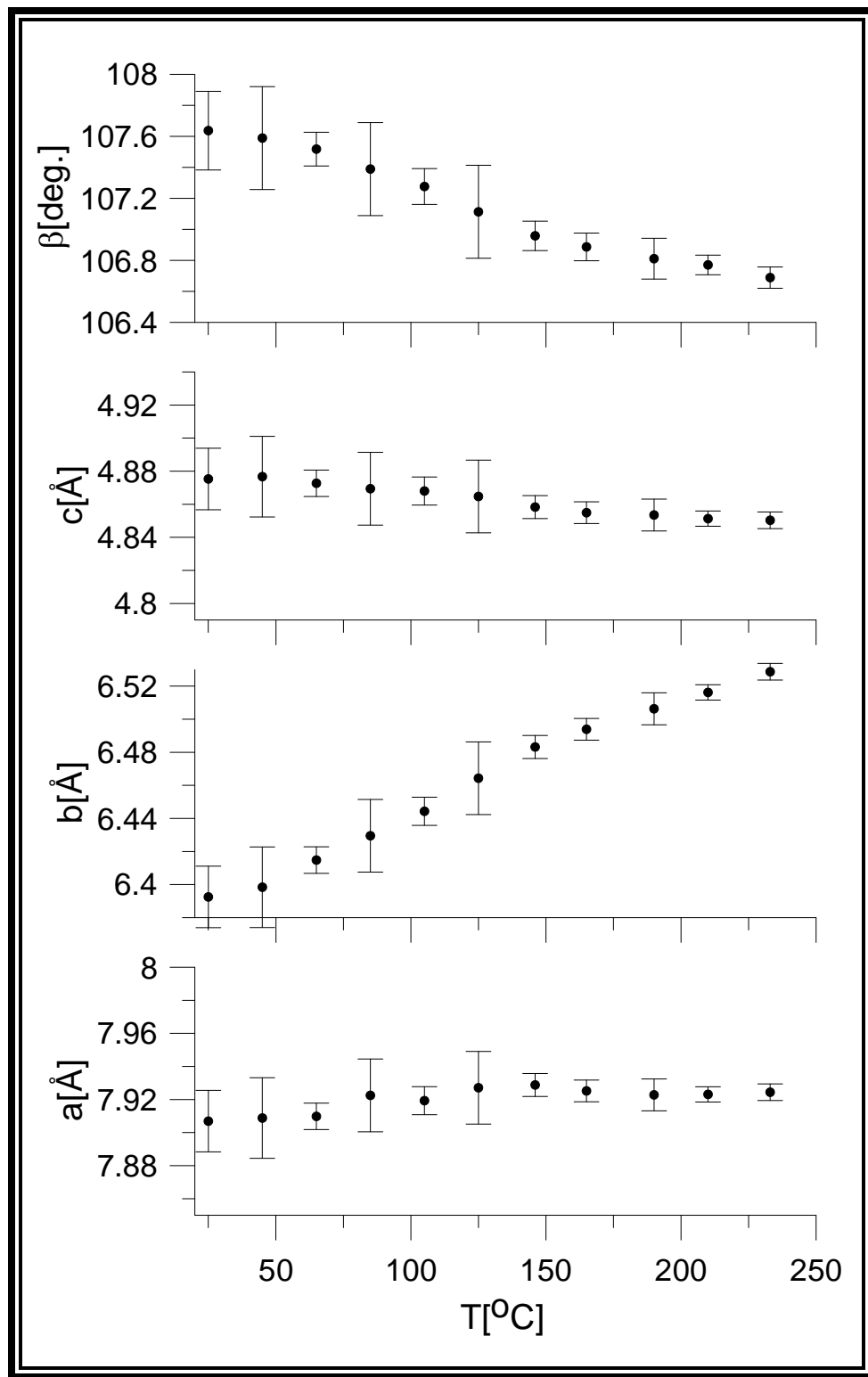


Figure 5.2: Temperature dependence of the lattice parameters of the monoclinic CsH_2PO_4 phase obtained from Le Bail fits to X-ray diffraction data. The lattice parameters vary smoothly with T, indicating that the RT monoclinic phase persists up to 233°C.

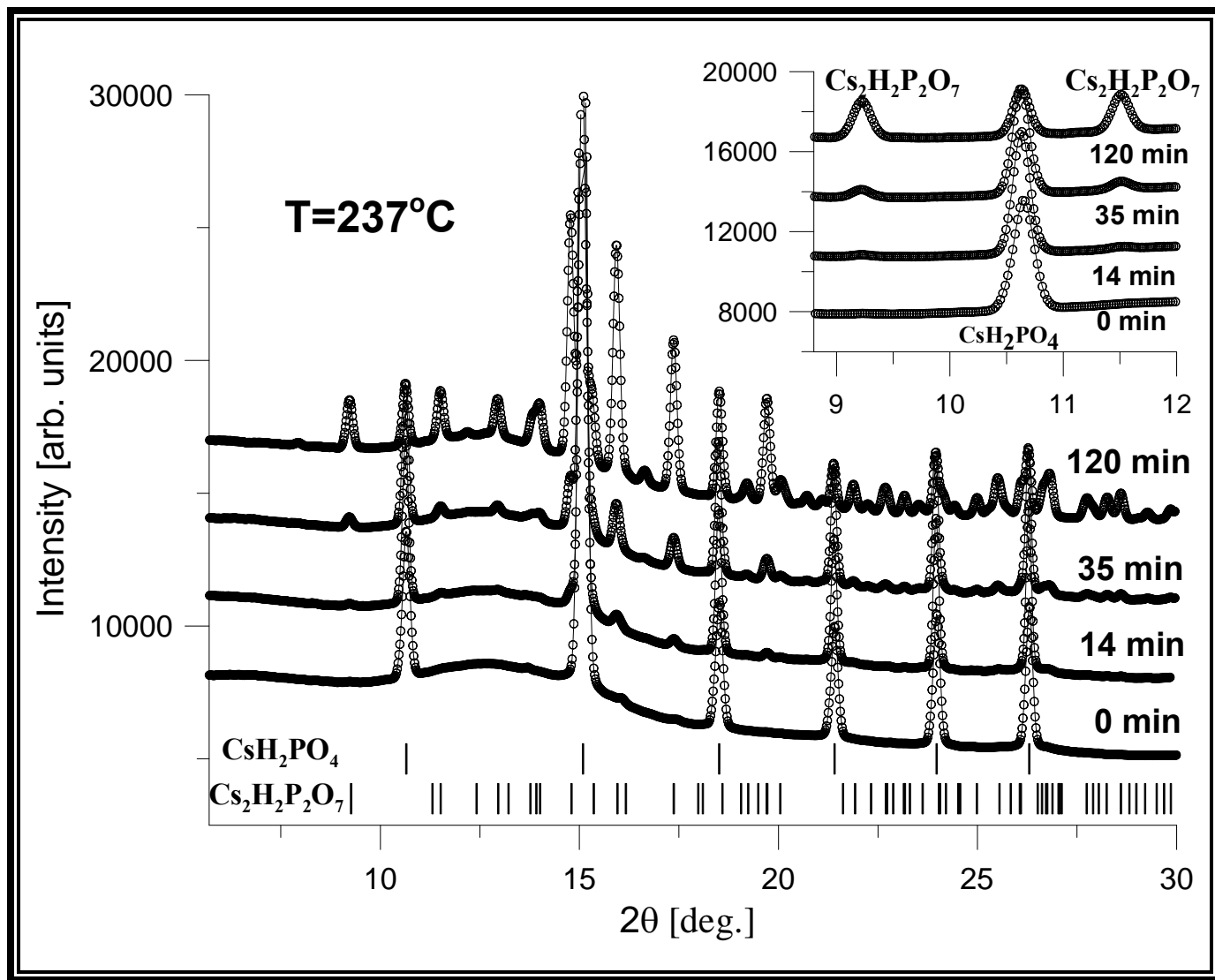


Figure 5.3: Time resolved synchrotron X-ray powder diffraction patterns of CsH_2PO_4 measured at $T=237^\circ\text{C}$ under ambient pressure. The data evidences the slow and partial decomposition of the cubic CsH_2PO_4 phase via dehydration according to the reaction $2\text{CsH}_2\text{PO}_4 \rightarrow \text{Cs}_2\text{H}_2\text{P}_2\text{O}_7 + 2\text{H}_2\text{O}$.

This may have prevented their observation of the short-lived cubic phase under ambient condition. By using a technique which allowed for rapid data collection, we were not only able to demonstrate that CsH_2PO_4 goes through a complete transition from its room-temperature monoclinic phase to a high-temperature cubic phase even in the absence of humid conditions, but also that this transition precedes the decomposition of CsH_2PO_4 through dehydration.

The room temperature crystal structure of RDP is tetragonal. CDP on the other hand, has a monoclinic ($P2_1/m$) structure at room temperature⁴¹. If the mechanism responsible for the high proton

conductivity of these materials at high temperatures is due to a transition into a high symmetry phase, one would expect their crystal structures to be more similar even at temperatures other than their transition temperature. This discrepancy was resolved by finding that RDP undergoes an intermediate phase transition between temperatures of 90-130°C. This intermediate phase had been previously thought to have been a monoclinic phase similar but not isomorphic to that of room temperature CDP^{42,43}. Using synchrotron X-ray diffraction techniques, however, it was finally shown that the intermediate temperature phase was indeed isomorphic to room temperature CDP³³.

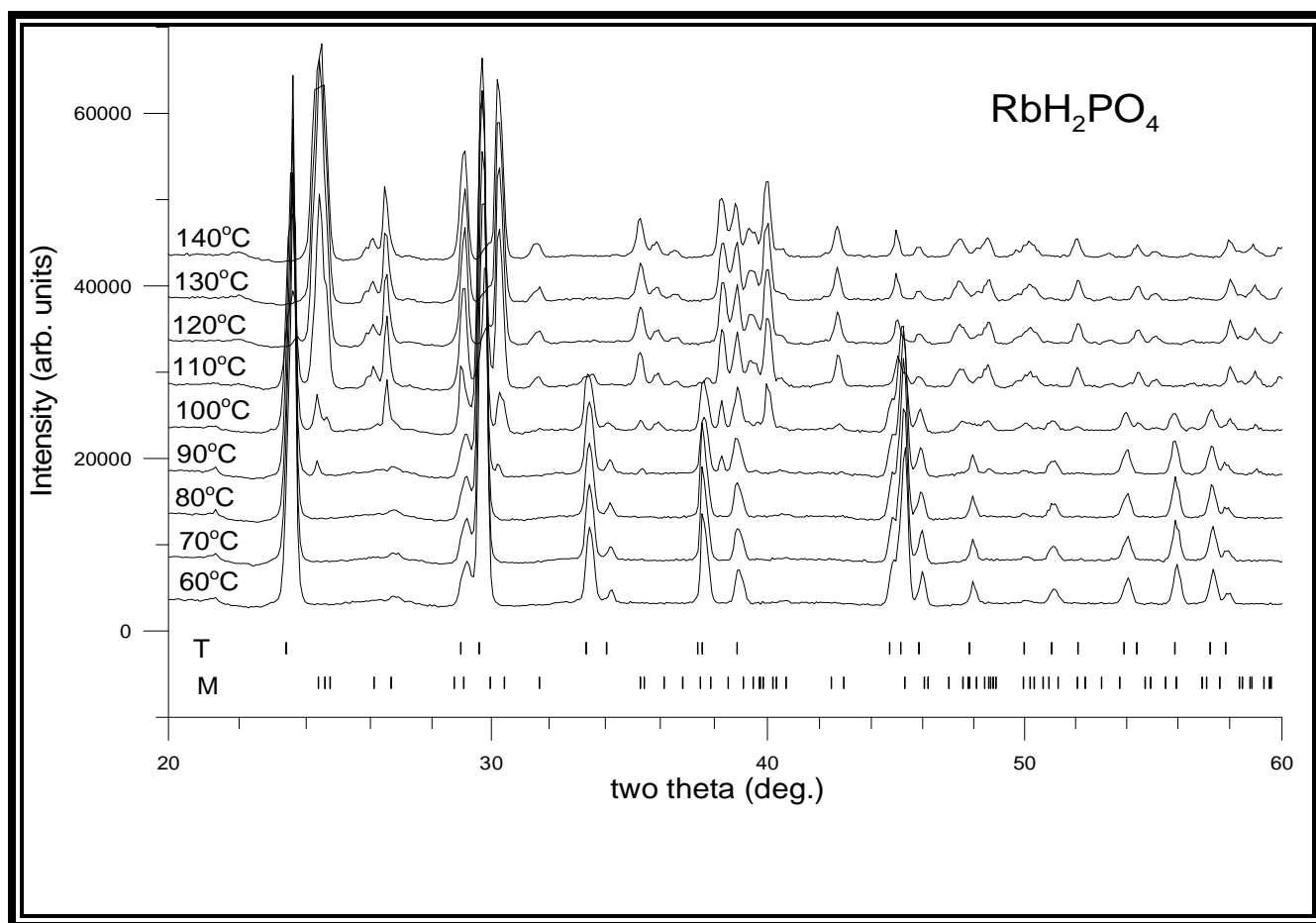


Figure 5.4: Temperature-resolved XRD data collected within the 60°C-140°C temperature interval on polycrystalline RDP.

Figure 5.4 shows temperature-resolved XRD data collected within the 60°C-140°C temperature interval on polycrystalline RDP. The nine XRD patterns, which have been vertically shifted for clarity, demonstrate that the room-temperature tetragonal (I-42d) RDP phase undergoes a transition to an

intermediate-temperature monoclinic ($P2_1/m$) modification, which, remarkably, is isomorphic to its monoclinic CDP counterpart.³³ Interestingly, another phosphate solid acid KH_2PO_4 exhibits a similar intermediate temperature behavior.³⁴ The vertical bars in Figure 5.3 are the Bragg reflection markers for the two above-mentioned RDP polymorphs.

Figure 5.5 further illustrates this transition indicating the changes in lattice parameters undergone by RDP in the 30-200°C temperature range. This also sheds light on why the true intermediate structure had been disagreed upon previously. A mixture of both the room temperature tetragonal and the intermediate monoclinic phases is present at temperatures between 90 and 130°C. The single monoclinic phase isomorphic to that of room temperature CDP is then present and stable at temperatures between 140 and 200°C (see illustrations 5.1 and 5.2)

The isomorphism between monoclinic RDP and CDP is significant because it suggests that *the same* microscopic structures and dynamics govern the high-temperature superprotonic behavior in both these materials, and, consequently, a general cation-independent conduction mechanism is likely to be at work in the high-temperature phases of phosphate based solid acids. This implies, however, that a monoclinic-cubic polymorphic structural transition, similar to the one in CDP, is responsible for triggering the proton conductivity enhancement in the Rb-based compound. RDP undergoes a proton conductivity jump, but this behavior could not be observed under ambient-pressure conditions.³³

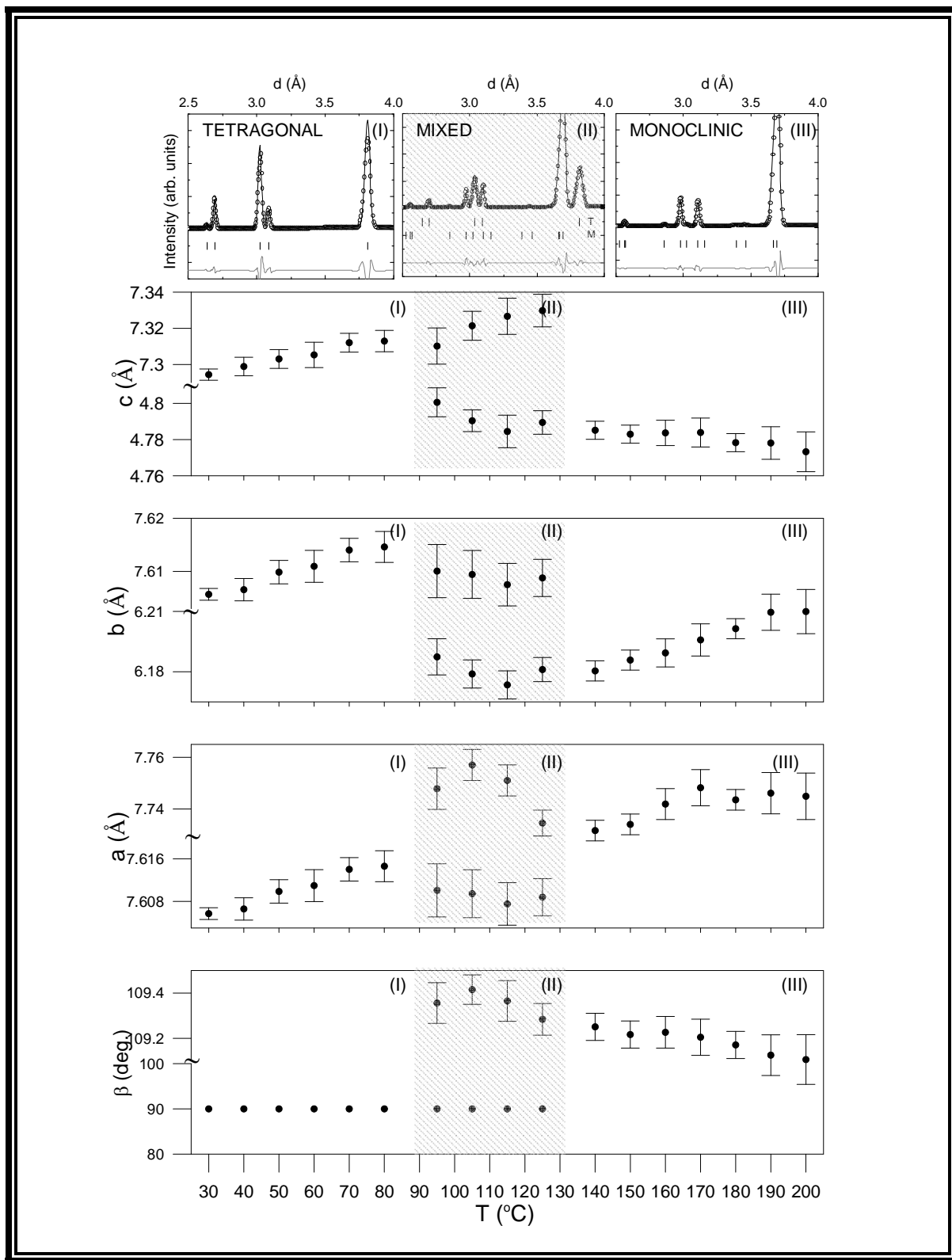


Figure 5.5: Temperature dependence of the lattice parameters of the (I) tetragonal RDP, (II) mixed (tetragonal + monoclinic), and (III) monoclinic phases. At each temperature the lattice parameters were obtained from Le Bail fits to x-ray diffraction data. The upper panels show fits to the (I) 30°C, (II) 110°C, and (III) 150°C XRD patterns.

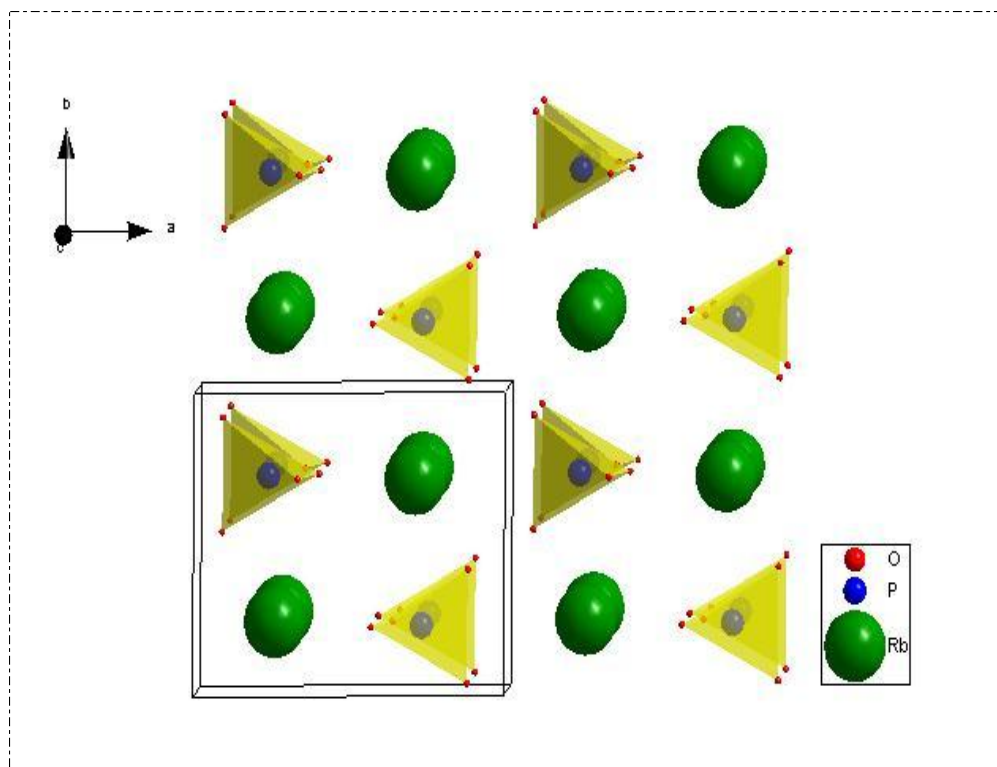


Illustration 5.1: Monoclinic RbH_2PO_4 ($T=150^\circ\text{C}$).

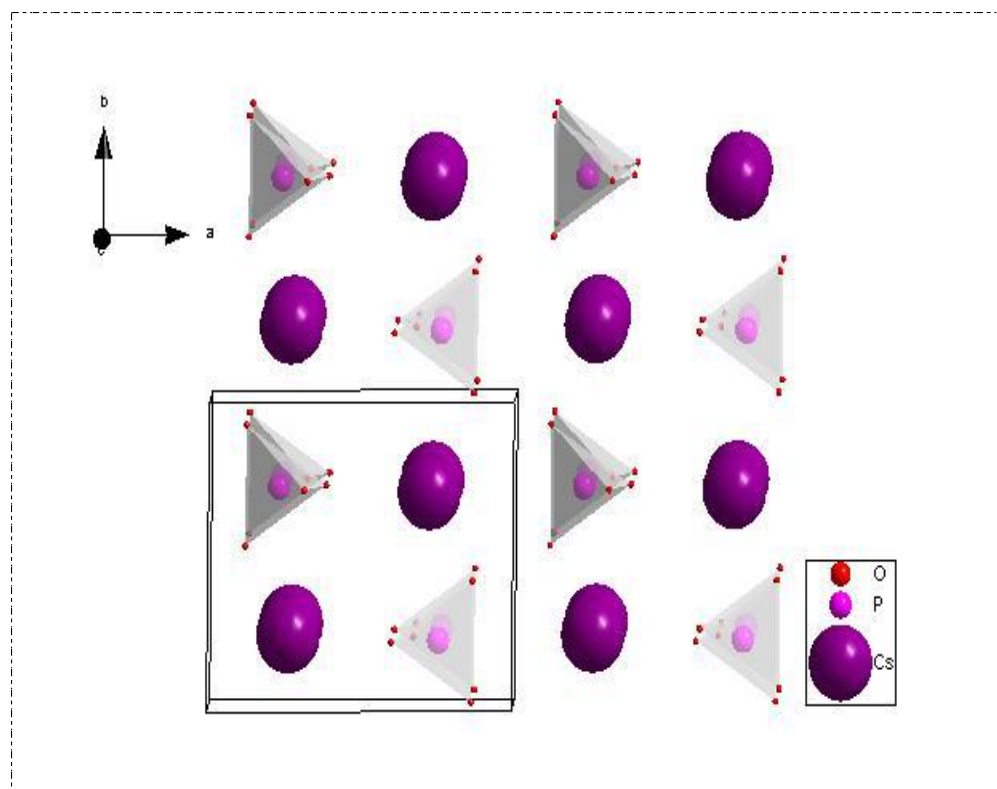


Illustration 5.2: Monoclinic CsH_2PO_4 (room temperature).

5.2 CsH_2PO_4 & RbH_2PO_4 : HIGH PRESSURE CONDITIONS

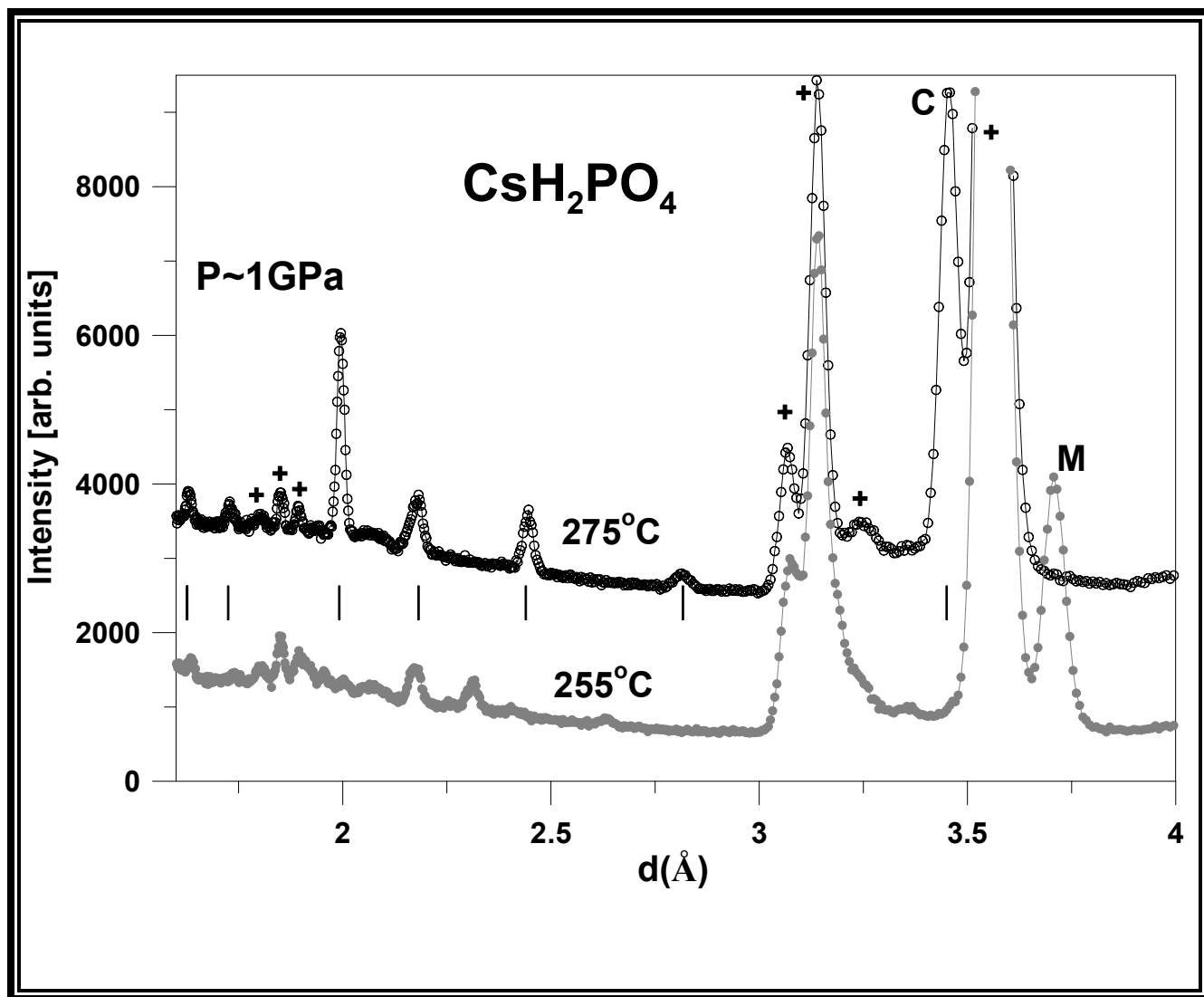


Figure 5.6: XRD patterns collected upon heating CDP from 255°C to 275°C under a pressure of 1 GPa. Datasets are shifted vertically for clarity. The data reveal a structural transition from CDP ϕ monoclinic ($P2_1/m$) phase to a high-temperature cubic ($\text{Pm}\bar{3}m$, $a=4.88 \text{ \AA}$) modification. The vertical bars indicate the d-spacing positions of the Bragg reflections from the cubic phase.

Figure 5.6 shows XRD patterns collected on polycrystalline CDP kept under a pressure of 1 GPa at two different temperatures: $T=255^\circ\text{C}$ (filled symbols) and $T=275^\circ\text{C}$ (open symbols). The 255°C data correspond to CDP ϕ monoclinic phase, which, under these high pressure conditions, persists up to higher temperatures than under ambient pressure.³² The XRD pattern recorded at 275°C , however, can

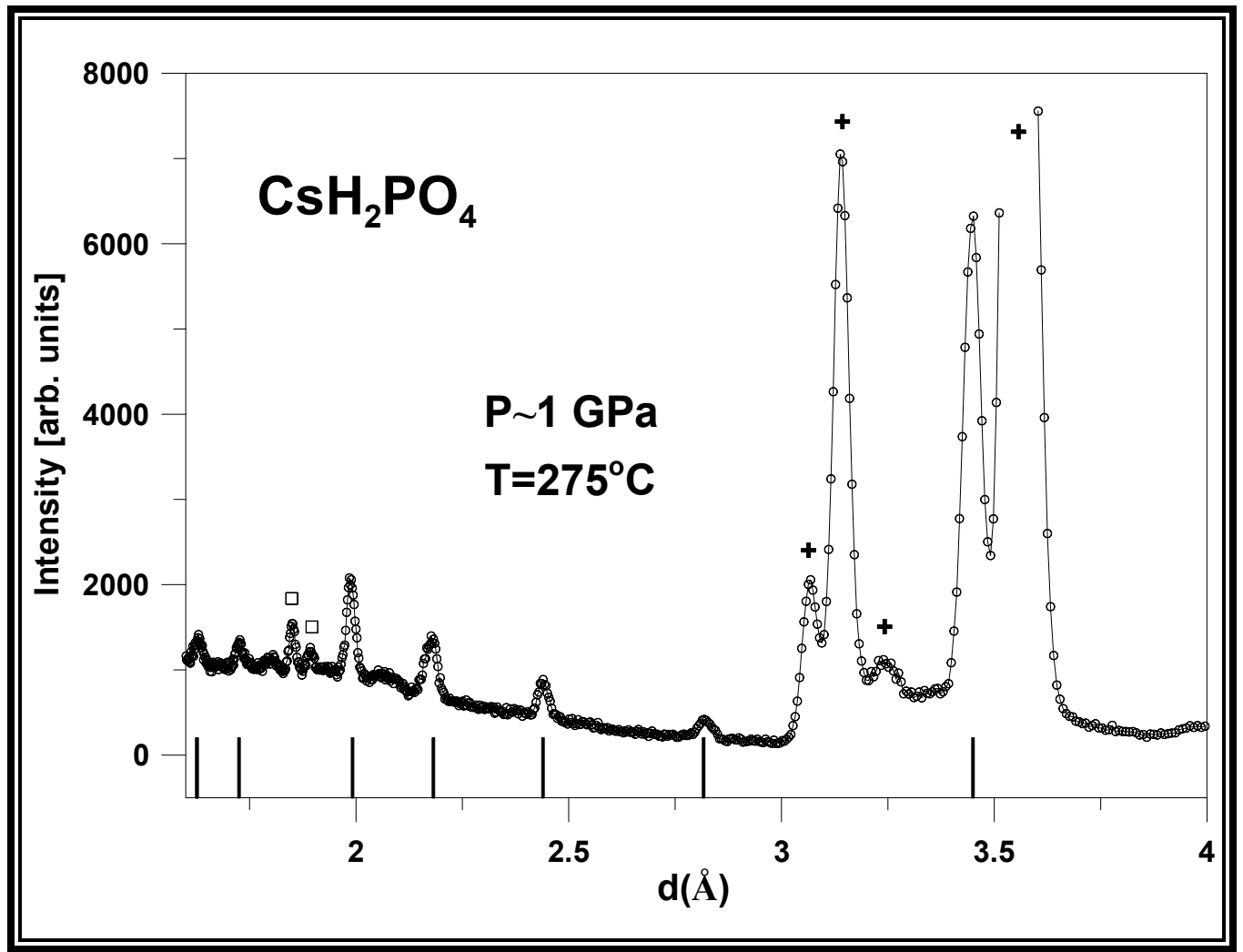


Figure 5.7: Synchrotron X-ray powder diffraction pattern from CsH_2PO_4 measured under high pressure ($\sim 1\text{ GPa}$) at $T=275^\circ\text{C}$. The vertical bars indicate the d-spacing positions of the Bragg reflections from the cubic CsH_2PO_4 phase ($Pm3m$; $a=4.96\text{Å}$). The peaks marked by crosses and squares are fluorescence lines from cesium and tungsten respectively.

be indexed to a single cubic phase with space group $Pm3m$ and lattice parameter $a=4.88\text{ Å}$ the vertical bars mark the d-spacing positions of the Bragg reflections corresponding to this indexing. The lattice parameter has a slightly reduced value from its ambient-pressure counterpart ($a=4.962\text{Å}$), which is obviously due to the application of high pressure. Figure 5.7 shows the single diffraction pattern corresponding to 275°C . The peaks marked by crosses correspond to boron nitride, and to cesium and tungsten fluorescence (we see tungsten because it is used in the slits that define the X-ray beam). These sections were therefore excluded from the diffraction pattern that was indexed (see Figure 5.8). No reflections from cesium dihydrogen pyrophosphate are observed, which demonstrates that the

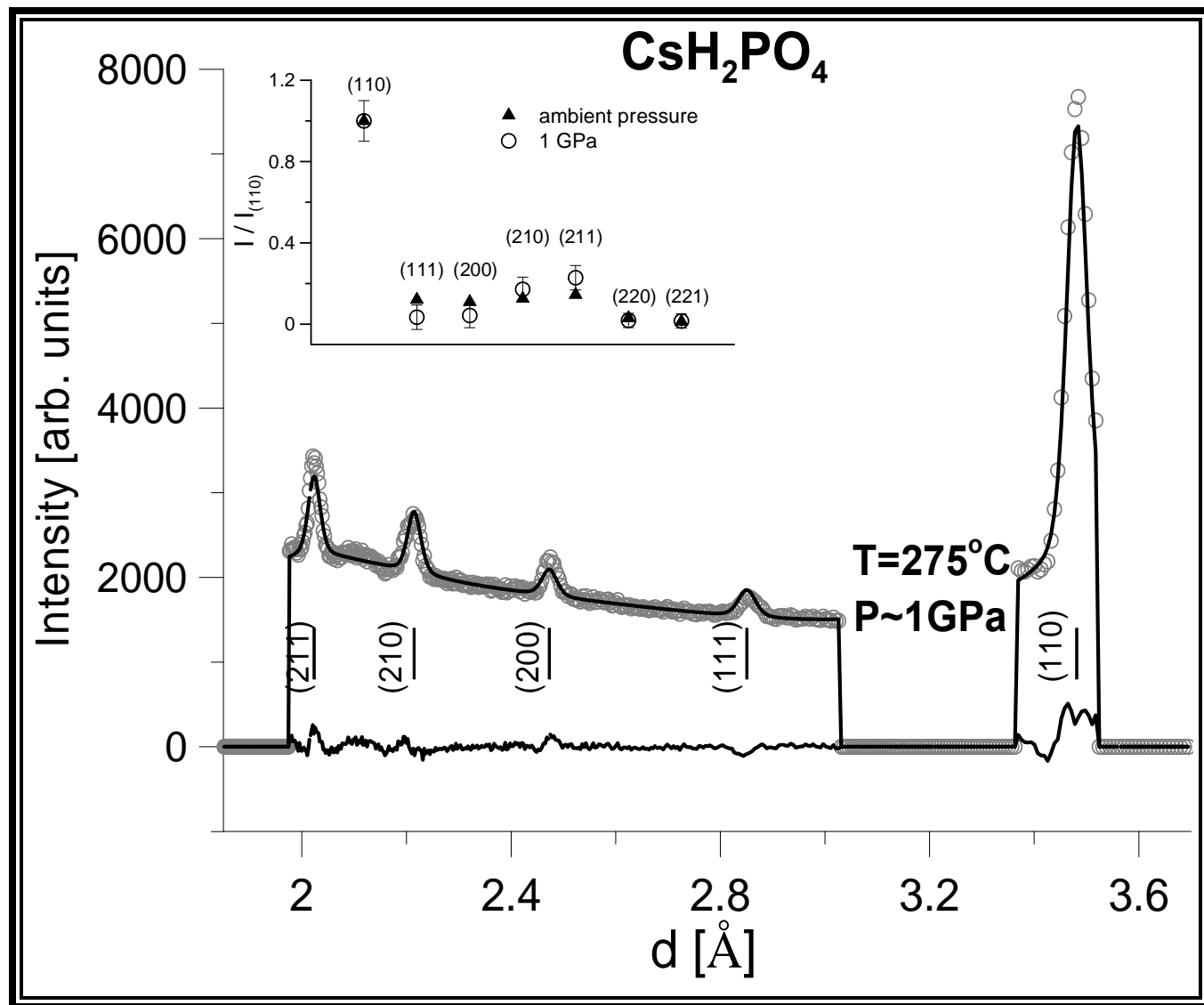


Figure 5.8: Rietveld refinement using CDP diffraction data collected at 275°C.

dehydration of CDP is completely suppressed by the application of high pressure. Thus, under 1GPa of pressure, a transition from the RT temperature CDP phase to a stable HT cubic phase occurs in the 255°C-275°C temperature interval, i.e. under the same conditions where CDP's proton conductivity jump was observed² (see Figure 5.6). In other words, the superprotonic behavior of CDP coincides with the existence of a single, stable cubic phase. This represents direct evidence that the enhancement of the proton conductivity in CDP is triggered by a temperature induced monoclinic→cubic polymorphic phase transition and is not due to chemical modifications.

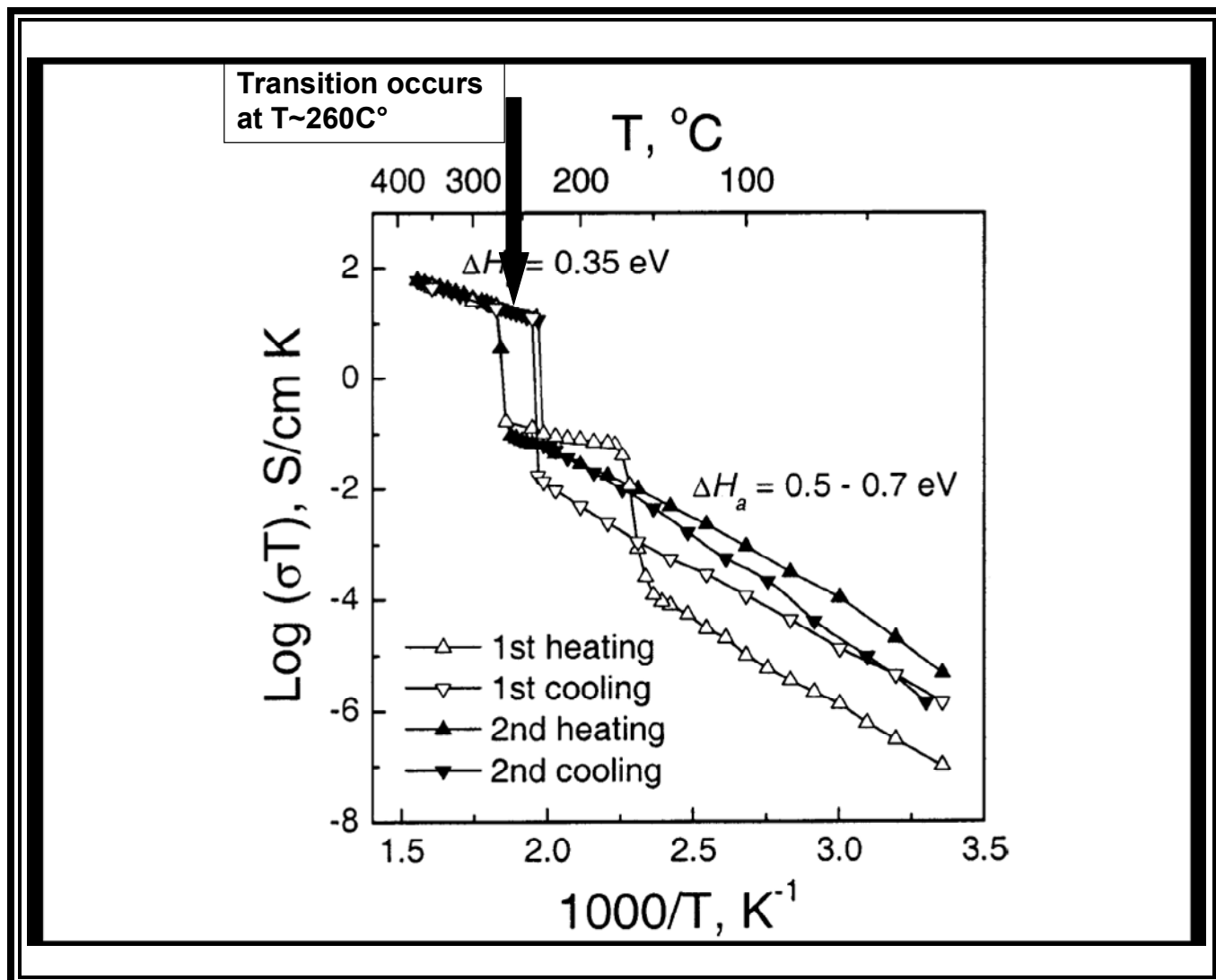


Figure 5.9: Proton conductivity vs. temperature measurements carried out under high pressure (1 ± 0.2 GPa) indicate that the onset of the superprotonic behavior occurs at about 260°C .

It is important to show that the crystal structure of the HT cubic CDP phase observed under high-pressure is basically the same as its ambient-pressure counterpart. This is demonstrated by the Rietveld refinement against high-pressure XRD data collected at 275°C shown in Figure 5.8. The solid line here is the best Rietveld fit, the empty symbols represent the scattered intensity measured as a function of d-spacing, the lower trace is the difference curve (between the observed and calculated patterns), and the vertical bars are reflection markers for the Bragg reflections. The same dynamically-disordered- PO_4 -tetrahedra model that describes the ambient-pressure cubic CDP phase was used for the initial atom positions. The inset shows a comparison between the integrated intensities of seven Bragg reflections

from the cubic CDP phase observed under high pressure (empty circles) and under ambient pressure (filled triangles). While the above Rietveld refinement might not reveal possible subtle differences between the ambient- and the high-pressure cubic CDP phases (because of extended excluded regions, overlap between fluorescence and diffraction peaks, preferred orientation effects, peak-shape issues etc.), such minute structural differences do not have a determining effect on the superprotonic behavior of CDP. This is supported by the fact that a jump in the proton conductivity of CDP has been observed upon heating under high-pressure² as well as under ambient (pressure and humidity) conditions³³. Therefore, if the two cubic CDP structures (at ambient- and high-pressure) are not identical, the slight differences between them are certainly not responsible for triggering (or inhibiting) the superprotonic behavior.

The fact that both RDP and CDP undergo a superprotonic transition is interesting since they have different crystal structures at room temperature. Finding the intermediate structure of RDP therefore gave new life to our theory that the superprotonic behavior of both compounds is due to a structural modification to a higher symmetry phase. If the crystal structure of RDP becomes monoclinic at intermediate temperatures, the next step was to see whether it also becomes cubic at temperatures near its superprotonic transition like CDP. As discussed earlier, this was achieved using synchrotron X-ray diffraction data for a temperature resolved experiment at a pressure of 1 GPa. Just like its intermediate temperature structure, its superprotonic cubic structure is isomorphic to that of cubic CDP indicating that the mechanism for high proton conductivity is the same in both compounds. It should be noted however, that unlike CDP which can be kept from dehydrating at high temperatures by placing it in a saturated water vapor atmosphere, KDP can only be stabilized by subjecting it to high pressures.

Heating while keeping the sample under 1GPa of pressure was necessary to reveal a superprotonic behavior in RDP at about 295°C.³ To uncover the structural changes that accompany this proton conductivity enhancement we recorded synchrotron XRD patterns on polycrystalline RDP subjected to high pressure (p~1GPa) at temperatures between 150°C and 300°C. These data are presented in Figure 5.10, where the XRD pattern collected at 150°C corresponds to the monoclinic $P2_1/m$ RDP polymorph. Upon further heating, the XRD pattern changes indicating that structural changes occur in the sample.

At 295°C - which is exactly the temperature where the superprotonic jump was observed in RDP under 1 GPa of pressure the diffraction pattern can be observed to change to what appears to be a higher symmetry phase than its lower temperature counterparts.

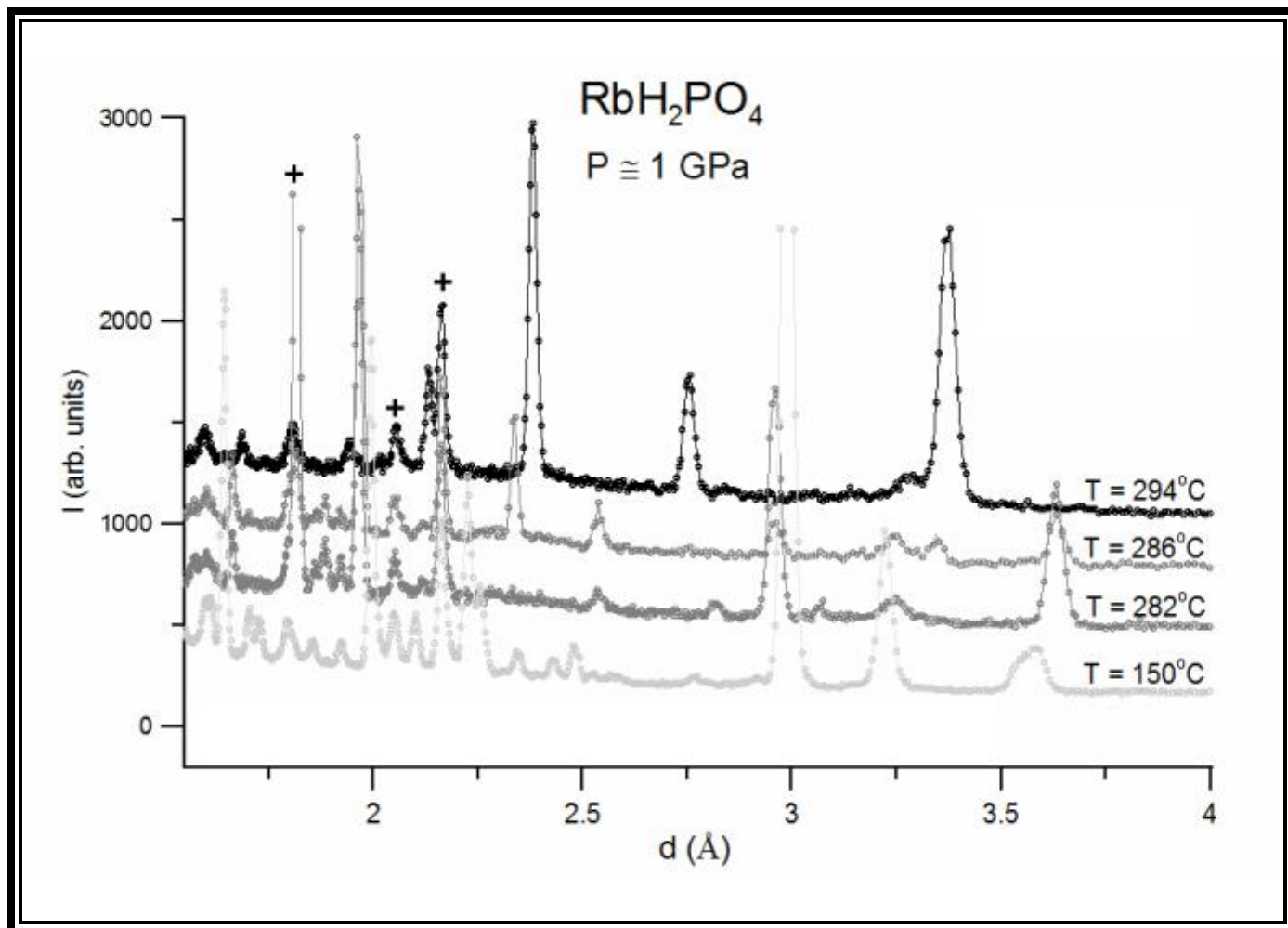


Figure 5.10: Temperature-resolved diffraction pattern for RDP under 1 GPa of pressure

5.3 KH_2PO_4

Because all the alkali metals are capable of forming phosphate based solid acids, the true goal of our research cannot be thoroughly achieved without investigating the structure and properties of all of them (excluding francium due to its radioactive nature). Although only CDP and RDP have been shown to exhibit a superprotonic transition, understanding the differences between these two compounds and those of their Group 1 counterparts should also shed some light into the mechanism ultimately

responsible for their superprotonic behavior. The following sections will therefore focus on describing the currently known structures and properties of the alkali metal phosphate based solid acids.

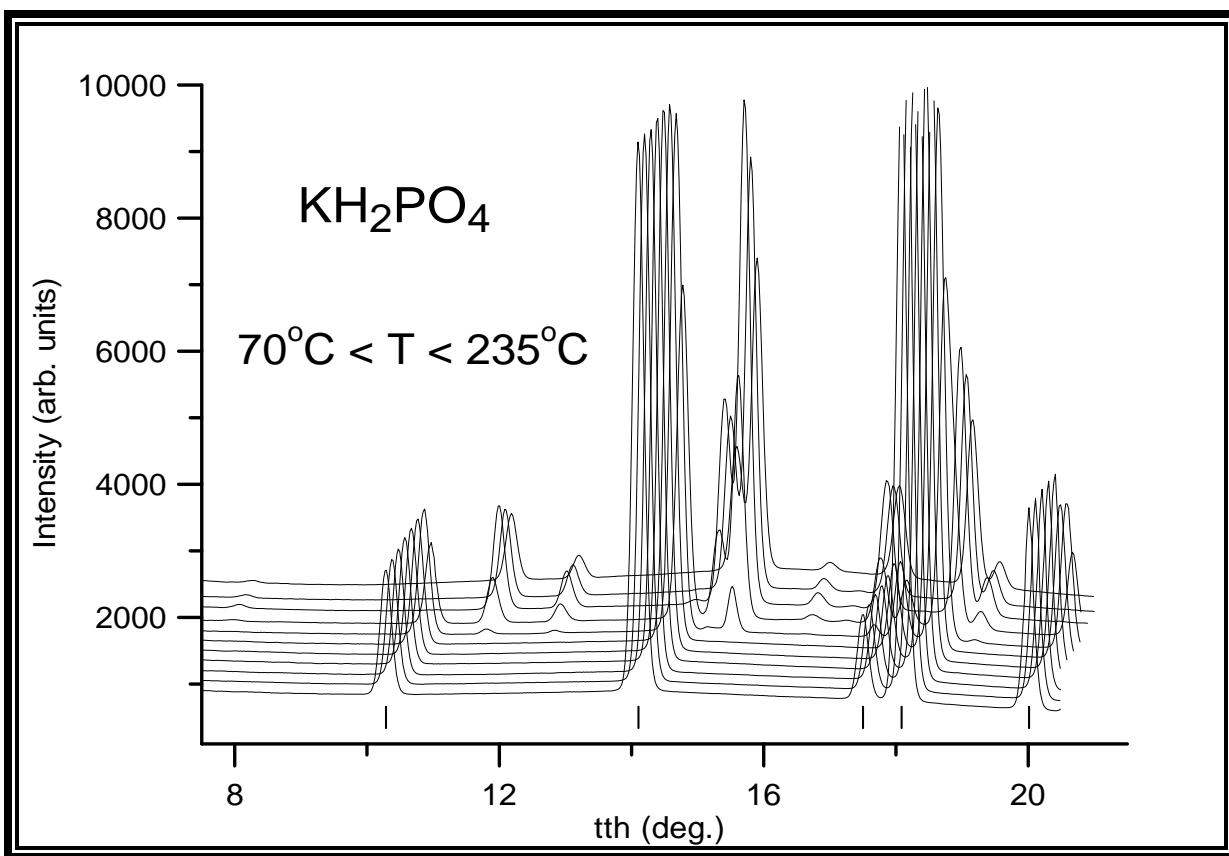


Figure 5.11: XRD patterns collected upon heating KDP from 70°C to 235°C in 15°C steps. Datasets are shifted vertically and horizontally for clarity. The vertical bars indicate the 2θ positions of the Bragg reflections from the room-temperature tetragonal (I-42d) KDP phase. The data indicate that a structural transition occurs at about 190°C ³⁴.

As was stated earlier, KDP is a very interesting case. KDP does not exhibit superprotonic behavior upon heating³. It however, does have a room temperature crystal structure isomorphic to that of RDP which does become superprotonic at high temperatures. Furthermore, KDP has also been shown to undergo a structural modification at intermediate temperatures similar to that of RDP and in fact also attains a monoclinic crystal structure isomorphic to both RDP and CDP³⁴.

Figure 5.11 illustrates the transition KDP undergoes as it is heated from 70°C to 235°C in 15°C steps. The diffraction pattern corresponding to 205°C was found to match the $\text{P2}_1/\text{m}$ space group of room temperature CDP and intermediate temperature RDP (see figure 5.12). Illustration 5.3 further

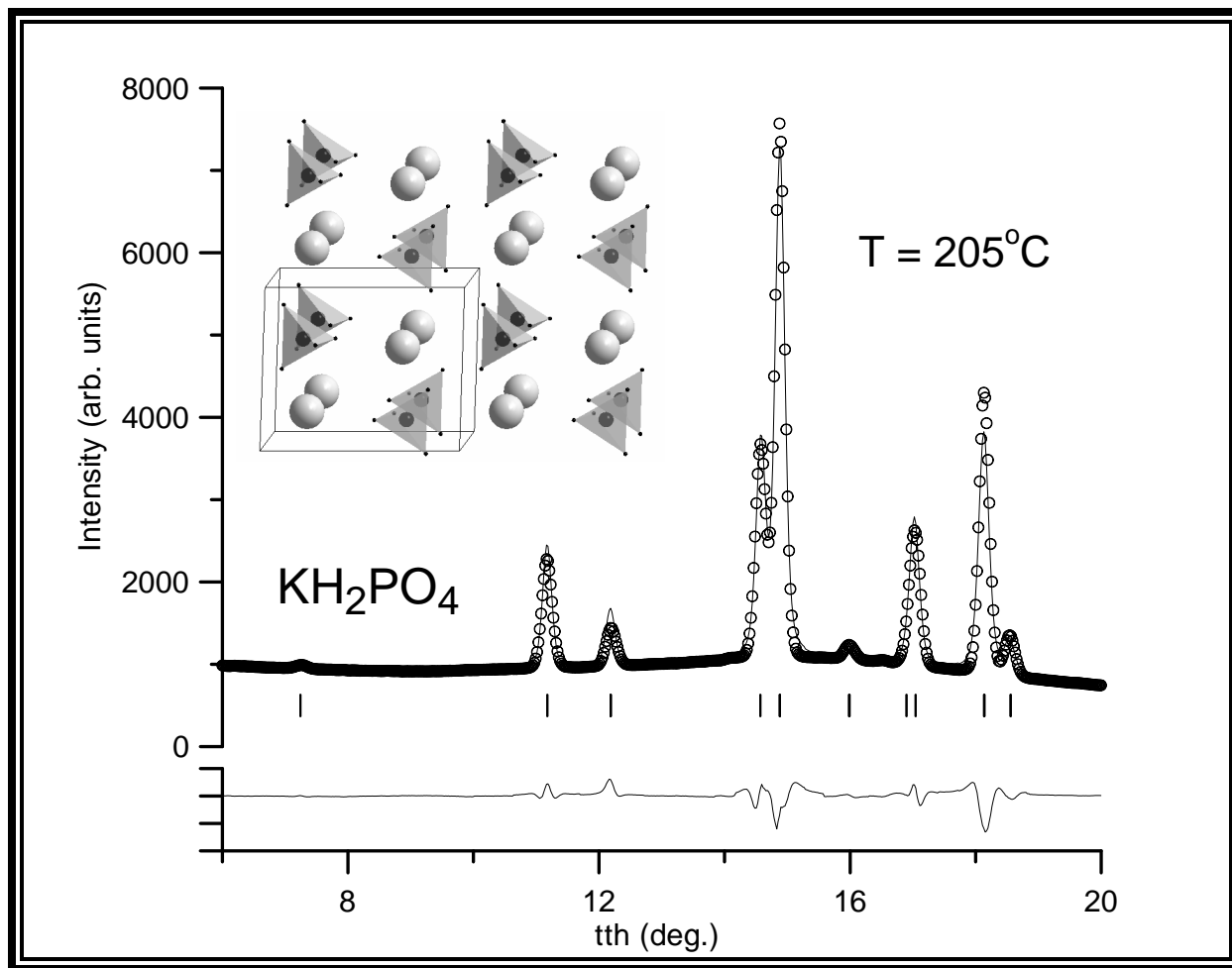


Figure 5.12: Structural refinement of the monoclinic KDP phase. The empty symbols represent the XRD data collected at 205°C, the solid line in the best Rietveld fit, and the vertical bars are the Bragg reflection markers. The lower trace represents the difference curve between the calculated and the observed XRD patterns: $I_{\text{calc}} - I_{\text{obs}}$. The inset shows the non-hydrogen atoms in the crystal structure of monoclinic KDP, including the PO_4 tetrahedra and the K ions (light spheres).

shows how the intermediate crystal structures of both KDP and RDP are identical. Although KDP does not exhibit superprotonic behavior at high temperatures, it is still unknown whether it undergoes a structural transition into a cubic phase at high temperatures. Since the cubic transition in RDP occurs at a higher temperature than that of CDP, one would assume that the one in KDP, if there is one, might occur at even higher temperatures. However, being able to observe this phase might prove to be even tougher than in RDP. Figure 5.13 depicts the lattice parameters of the monoclinic phases in these solid acids as a function of cation size.

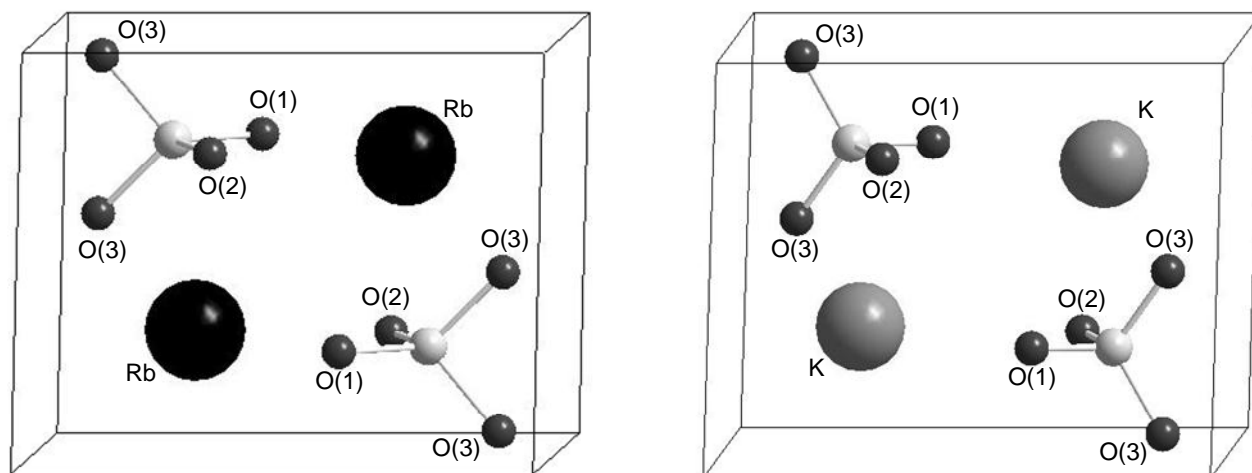


Illustration 5.3: Comparison between the atom positions in the unit cells of RDP and KDP demonstrating the isomorphism of the two crystal structures.

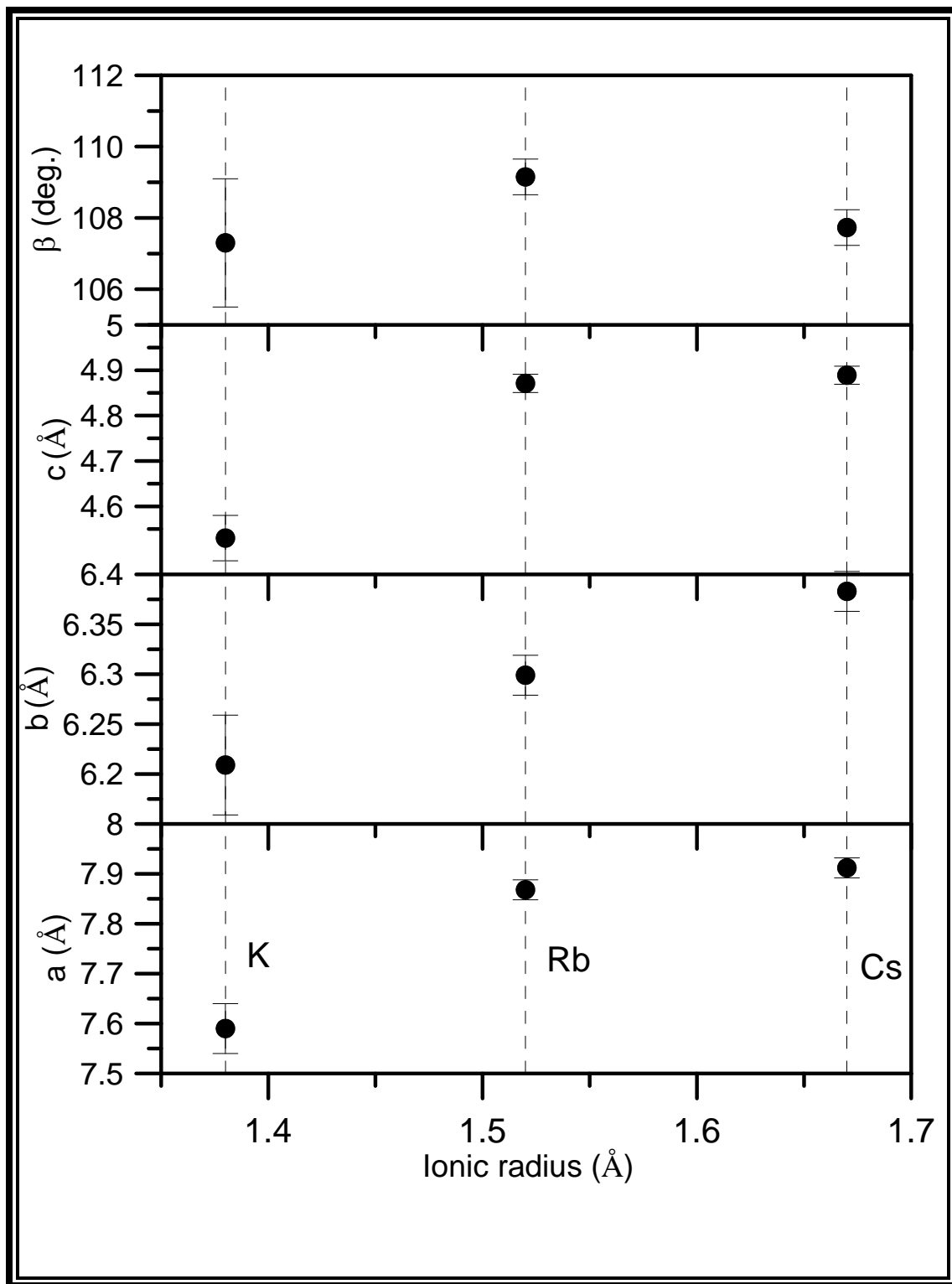


Figure 5.13: Lattice parameters of the monoclinic phases of KDP, RDP, and CDP as a function of the radius of the cation.

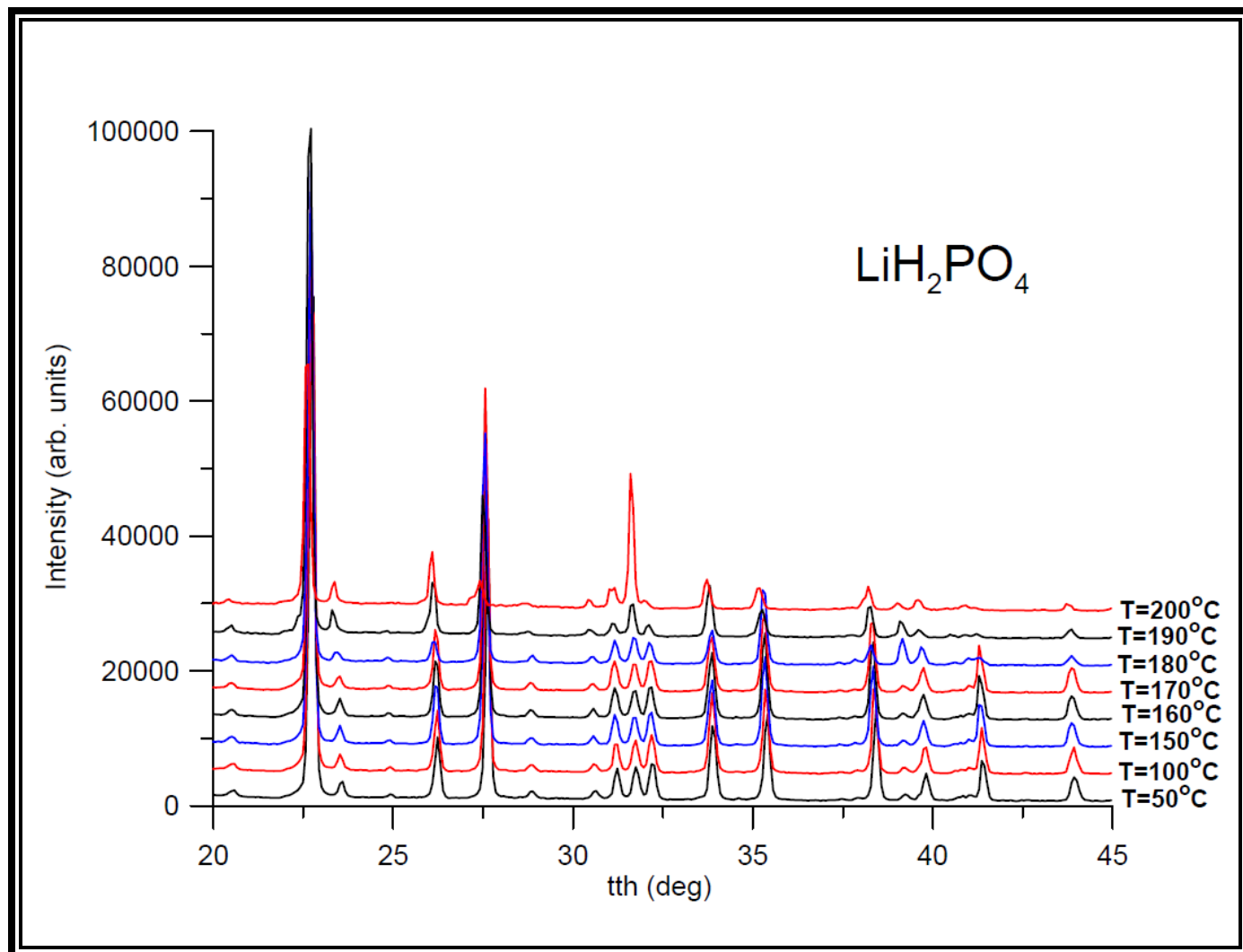


Figure 5.14: Temperature resolved x-ray diffraction pattern for LiH_2PO_4 showing almost no change in crystal structure in the 50-200°C range.

5.4 LiH_2PO_4

Figure 5.14 shows the diffraction pattern for LiH_2PO_4 at temperatures 50-200°C. As can be seen from the graph, the diffraction pattern shows almost no change in crystal structure through the entire temperature range. This agrees with the fact that LiH_2PO_4 has not been shown to exhibit a superprotonic phase. Unlike KDP, RDP, or CDP, its crystal structure is extremely stable as it is heated. It is important to note here that Li has the smallest ionic radius of all the alkali metals. The cation in LiH_2PO_4 therefore, takes up the least amount of space in the unit cell compared to that of the phosphate tetrahedra than in any of its Group 1 solid acid counterparts.

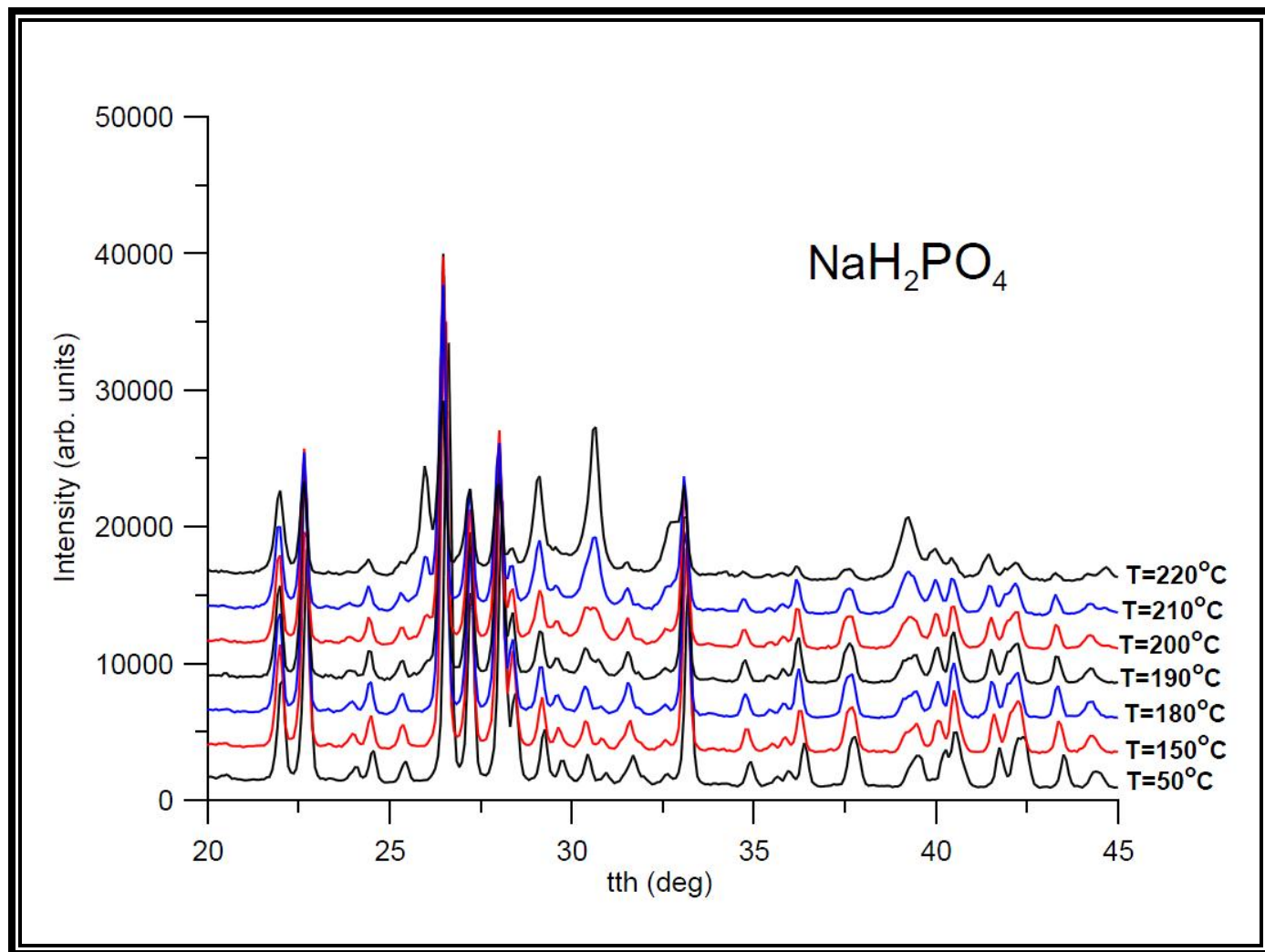


Figure 5.15: Temperature resolved x-ray diffraction pattern for NaH_2PO_4 showing very little change in crystal structure in the 50-220°C range.

5.5 NaH_2PO_4

The second smallest element in Group 1 is sodium. Sodium however has an atomic number comparable to that of potassium and oxygen and therefore is not dwarfed as much as lithium is in the unit cell. Figure 5.15 shows the diffraction pattern for NaH_2PO_4 at temperatures 50-220°C. Although the pattern shows more of a change than that of LiH_2PO_4 , the changes correspond more to a slight variation in lattice parameters and not to a structural transition with different crystal symmetry. Like LiH_2PO_4 , NaH_2PO_4 has not been observed to undergo a superprotonic transition.

5.6 MIXED CATION SOLID ACIDS: $\text{Cs}_x\text{Rb}_{1-x}\text{H}_2\text{PO}_4$

An interesting thing to note is illustrated in Figure 5.16. The diffraction patterns show what happens when a percentage of the rubidium cations are replaced by cesium. At $x=0$ and $x=0.1$, corresponding to no cesium and 10% cesium respectively, they appear to be the tetragonal structures of room temperature RDP, but when just 30% of the rubidium cations are replaced with cesium ($x=0.3$) it appears that the structure becomes isomorphic with the monoclinic room temperature CDP. These results seem to reinforce the trend that as the cation size increases in these solid acids, the temperature range at which the tetragonal, monoclinic and cubic crystal structures are stable is shifted towards lower temperatures.

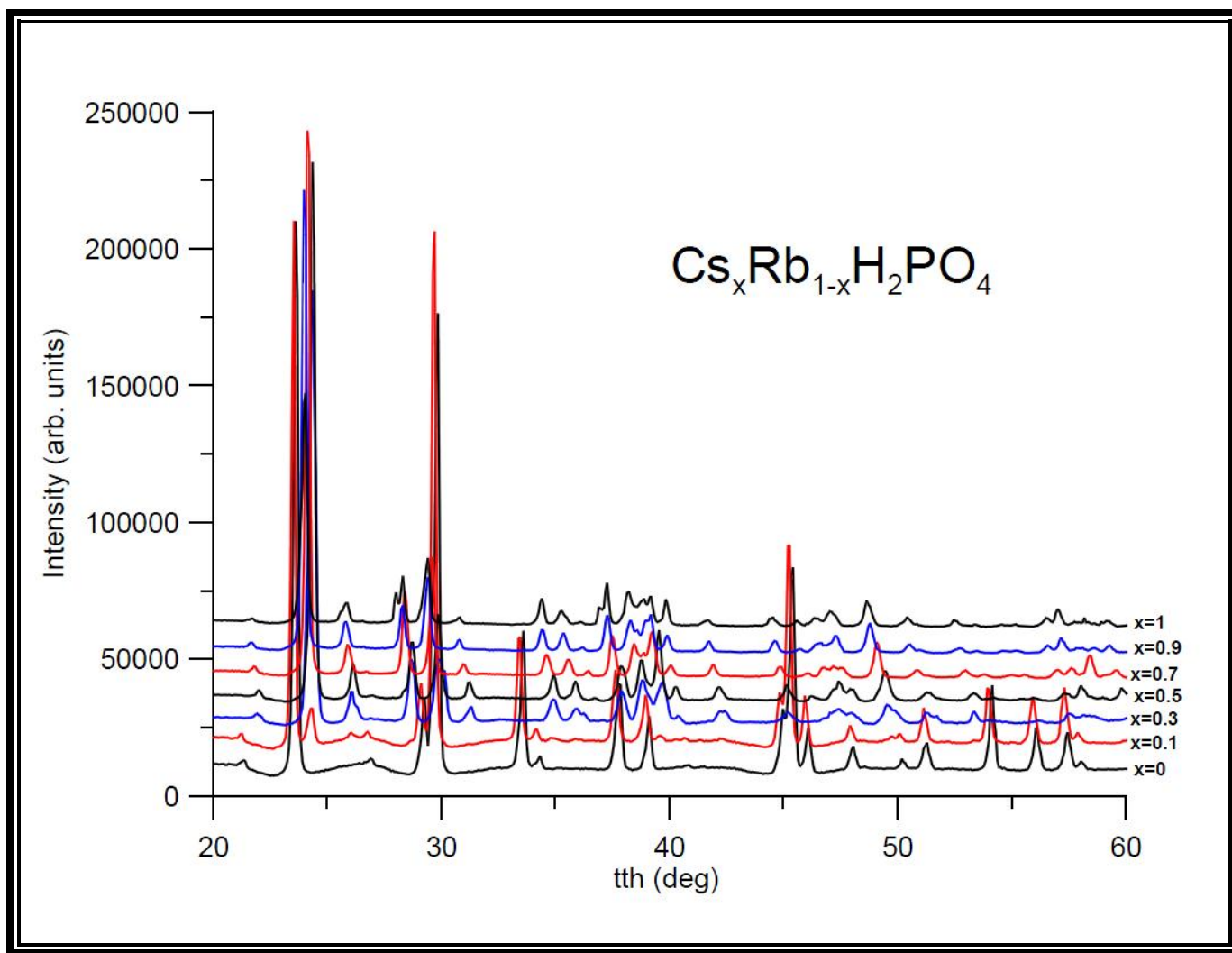


Figure 5.16: $\text{Cs}(x)\text{Rb}(1-x)\text{H}_2\text{PO}_4$: Compounds in which a fractional part of the rubidium ions are replaced with cesium.

Chapter 6: Conclusions

In summary, we have observed a high-temperature monoclinic to cubic phase transition in both the ambient and high-pressure synchrotron X-ray powder diffraction experiments of CDP. These results show that the phase transitions can be observed at the same temperature range in which the superprotonic transitions had been previously observed under both ambient and high temperature conditions. This indicates that the superprotonic behavior of CsH_2PO_4 is associated with a monoclinic to cubic polymorphic structural transition rather than chemical modifications due to loss of H_2O . This is further supported by the new results of the ambient pressure experiment.

Although the cubic phase was not stable under ambient conditions, it was nonetheless present if only for about 10-15 minutes before decomposing through dehydration. This phase transition under ambient conditions had not been observed in the past due to its brief window of existence and the nature of the previous experimental methods employed. It was the absence of this transition in ambient conditions that most skeptics used as their main argument for attributing the superprotonic behavior of CsH_2PO_4 to factors other than a monoclinic to cubic phase transition. Furthermore, the stability of the monoclinic phase of CsH_2PO_4 up to temperatures right below that at which it had previously been observed to become superprotonic (See Figure 6.1) indicates a strong correlation between the sudden phase transition and its superprotonic behavior.

The fact that RDP also exhibits superprotonic behavior at high temperature provides a perfect analog with which to test our current theories on the superprotonic behavior of CDP. At first glance, comparing the mechanism responsible for the superprotonic behavior of both acids seems far-fetched at best due to the fact that they both exhibit a different crystal structure at ambient conditions. As has been shown before, however, RDP undergoes a phase change at intermediate temperatures in which its crystal structure becomes isomorphic to that of room temperature CDP. This indicates that the proton conduction mechanism responsible will most likely be identical for both acids if RDP can be shown to undergo the same polymorphic structural transition into a cubic phase that CDP undergoes at temperatures at or near the superprotonic transition. The diffraction pattern for RDP at 294°C collected

under 1 GPa of pressure shows the presence of a high symmetry cubic phase ($Pm\bar{3}m$). This phase is isomorphic to that of CDP at its superprotonic temperature.

Finding a high temperature cubic phase for RDP indicates that the dynamics of the enhanced proton conduction in these materials is independent of the cation type. It therefore suggests that it is most likely due to the symmetry of the unit cell and the position of the phosphate groups with relation to one another. The absence of superprotonic behavior for RDP under ambient conditions may also indicate a strong correlation between the cation size and its effect on the symmetry between phosphate groups.

This work is hopefully only the beginning of a deeper understanding of the superprotonic behavior of fully hydrogenated phosphate based solid acids. A deeper understanding of the transition CDP and RDP go through as they reach the cubic phase and begin to decompose under ambient conditions, for instance, will hopefully yield knowledge on how to improve their performance as fuel cell electrolytes and how to take full advantage of their properties. Understanding and eventually controlling the microscopic mechanisms that govern the enhanced proton conductivity in these types of materials might represent a step toward the rational design of functional superprotonic conductors.

References

1. D.A. Boysen, T. Uda, C.R.I. Chisholm, and S.M. Haile, *Science*, **303**, 68(2004).
2. D.A. Boysen, S.M. Haile, H. Liu, and R.A. Secco, *Chem. Mater.* **15**, 727(2003).
3. D.A. Boysen, S.M. Haile, H. Liu, and R.A. Secco, *Chem. Mater.* **16**, 693(2004).
4. W. Bronowska, *J. Chem. Phys.* **114**, 611(2001).
5. R. Feidenhansl, *Surf. Sci. Rep.* **10**, 105(1989).
6. C. E. Botez, K. Li, E. D. Lu, W. C. Elliott, E. H. Conrad, and P. W. Stephens, *Appl. Phys. Lett.* **81**, 4718(2002).
7. J. T. E. Galindo, A. H. Adair, C. E. Botez, V. C. Flores, D. B. Baques, L. F. Cobas, and J. A. Matutes-Aquino, *Appl. Phys. A* **87**, 743(2007).
8. H. N. de Armas, O. M. Peeters, N. Blaton, G. Van der Mooter, D. J. A. De Rider, and H. Schenk, *J. Pharm. Sci.* **10**, 2123(2006).
9. C. E. Botez, P. W. Stephens, C. Nunes, R. Suryanarayanan, *Powder Diffr.* **18**, 214(2003).
10. *Structure determination from powder diffraction data*, IUCr Monographs in Crystallography, Editors: W. I. F. David, K. Shankland, L. B. McCusker, and Ch. Baerlocher, Oxford Science Publications 2002.
11. K. Itoh, T. Matubayashi, E. Nakamura, and H. Motegi, *J. Phys. Soc. Japan* **39**, 843(1975).
12. "Arrhenius, Svante." *Encyclopædia Britannica*. 2006. *Encyclopædia Britannica Online*. 15 Nov. 2006 <<http://www.britannica.com/eb/article-9009618>>.
13. H. Matsunaga, K. Itoh, and E. Nakamura. *X-Ray Structural Study of Ferroelectric Cesium Dihydrogen Phosphate at Room Temperature*. *J. Phys. Soc. (Japan)* **48**, 2011(1980).
14. E. Ortiz, R.A. Vargas, and B.E. Mellander, *J. Chem. Phys.* **110**, 4847(1999).
15. W. Bronowska, *J. Chem. Phys.* **114**, 611(2001).
16. S. M. Haile, D. A. Boysen, C. R. I. Chisholm and R. B. Merle, "Solid Acids as Fuel Cell Electrolytes," *Nature* **410**, 910-913 (2001).
17. N.M. Plakida, *Phys. Stat. Sol.*, **135**, 133(1986).
18. A. I. Baranov, V. P. Khiznichenko and L. A. Shuvalov: *Ferroelectrics* **100**, 135(1989).
19. D. A. Boysen, S. M. Haile, H. Lui and R. A. Secco "High-temperature Behavior of CsH₂PO₄ under both Ambient and High Pressure Conditions," *Chem. Mat.* **15**, 727-736 (2003).
20. D. A. Boysen, T. Uda, C. R.I. Chisholm and S. M. Haile, "High performance Solid Acid Fuel Cells through humidity stabilization," *Science Online Express*, Nov 20, 2003; *Science* **303**, 68-70 (2004).
21. J.H. Park, *Phys. Rev. B* **69**, 054104(2004).
22. EG&G Services, Parsons, Inc. *Fuel Cell Handbook*. National Energy Technology Laboratory, Office of Fossil Energy, U.S. Department of Energy, P.O. Box 880, Morgantown, West Virginia 26507-0880, 5th edition, October 2000.

23. Fuel Cells 2000. Fuel Cell Basics ó Benefits. <http://www.fuelcells.org/basics/benefits.html>, May 2011.
24. US Department of Energy, "More Capable Warfighting Through Reduced Fuel Burden," 2001.
25. Kittel, C. Introduction to Solid State Physics, Eighth Edition. John Wiley & Sons, Inc. New York, 2005.
26. Massa, W. Crystal Structure Determination, Second Edition, Springer-Verlag. Berlin, Germany. 2004
27. Cullity, B.D. Elements of X-ray Diffraction, Second Edition. Addison-Wesley Pub. Co. Reading, Mass. 1978.
28. Lipson, H. and Steeple H. Interpretation of X-Ray Powder Diffraction Patterns. St. Martin's Press. New York, 1970.
29. L. W. Finger, D. E. Cox, A. P. Jephcoat. *A correction for powder diffraction peak asymmetry due to axial divergence*. Journal of Applied Crystallography, 1994, **27**, 892-900.
30. A.P. Hammersley, S.O. Svenson, M. Hanfland, A.N. Fitch, and D. Hauserman, High Pressure Research **14**, 235(1996).
31. D.J. Weidner, M.T. Vaughan, J. Ko, Y. Wang, X. Liu, A. Yeganeh-haeri, R. E. Pacalo, Y. Zhao. In Syono Y and Manghnani, MH (ed.) High-Pressure Research: Application to Earth and Planetary Sciences. AGU, Washington DC, Geophysics Monograph Series, Vol. **67**, pp. 13617 (1992).
32. A. Preisinger, K. Mereiter, and W. Bronowska, Mat. Sci. Forum **166-169**, 511(1994).
33. C. E. Botez, H. Martinez, R. J. Tackett, R. R. Chianelli, J. Zhang, and Y. Zhao, J. Phys: Condens. Matter **21**, 325401(2009).
34. C. E. Botez, D. Carbajal, V. A. K. Adiraju, R. J. Tackett, and R. R. Chianelli, J. Phys. Chem. Solids (2010), doi:10.1016/j.jpcs.2010.08.004.
35. Clark, Jim (2005). "Atomic and Physical Properties of the Group 1 Elements". *Chemguide*
36. Royal Society of Chemistry. "Visual Elements: Group 1 ó The Alkali Metals". Visual Elements. Royal Society of Chemistry.
37. A.M. James and M.P. Lord in *Macmillan's Chemical and Physical Data*, Macmillan, London, UK, 1992.
38. J.E. Huheey, E.A. Keiter, and R.L. Keiter in *Inorganic Chemistry : Principles of Structure and Reactivity*, 4th edition, HarperCollins, New York, USA, 1993.
39. Lide, D. R., ed. (2003). *CRC Handbook of Chemistry and Physics* (84th ed.). Boca Raton, FL: CRC Press.
40. Nic, M.; Jirat, J.; Kosata, B., eds. (2006). "Electronegativity". *IUPAC Compendium of Chemical Terminology* (Online ed.). doi:10.1351/goldbook.E01990. ISBN 0-9678550-9-8.
41. C.E. Botez, J.D. Hermosillo, J. Zhang, J. Qian, Y. Zhao, J. Majzlan, R.R. Chianelli, C. Pantea, J. Chem. Phys. **127**, 194701 (2007)
42. R. Blinc, J. R. Ferraro, and C. Postmus, J. Chem. Phys. **51**, 732(1969).
43. M. T. Averbuch-Pouchot and A. Durif, Acta Crystallogr. C **41**, 665(1985).

Vita

Juan Hermosillo was born on December 21, 1980 in East Chicago, IN. His mother, Maria Del Carmen Perez raised Juan and his two brothers by herself for the majority of their childhood. They spent short intervals in Juarez, Mexico, Albuquerque, NM and Boulder, CO but mainly lived in El Paso, TX for the majority of his childhood and adolescence. Juan went to high school at Maxine L. Silva Magnet High School for Health Care Professions to take advantage of the school's science packed curriculum. He then attended the Massachusetts Institute of Technology where he obtained his B.S. in Chemical Engineering. He started his Master's work at the University of Texas at El Paso in the fall of 2004.

During his time at UTEP, Juan has gained a great deal of teaching experience. He was a teaching assistant for the Fields and Waves laboratory during his first two years at UTEP. He also worked for the Canutillo Independent School District as an academic tutor where he helped high school juniors and seniors pass the exit level TAKS test. From 2006-2008, Juan received a NSF GK-12 fellowship in which he acts as a science mentor for sixth grade students in collaboration with a science teacher at Ross and Bassett Middle Schools. This NSF grant was given to the college of science to create a partnership between UTEP and the El Paso Independent School District to explore the environment of the U.S./Mexico border. The project aims to significantly improve science learning among middle school science students by teaming teachers with science and engineering graduate fellows.

Currently, Juan is a pre-calculus/calculus teacher at Andress High School where he applies all his previous teaching experience to help his students succeed in their math and science classes.

Permanent address: 1531 George Dieter Dr. APT 1201
El Paso, TX 79936

This dissertation was typed by Juan Hermosillo.